Laboratoire d'Hydrodynamique, École Polytechnique
Unité de Mécanique, ENSTA-ParisTech

Thèse présentée pour obtenir le grade de

Docteur de l'Ecole Polytechnique

Specialité : MÉCANIQUE

par

Yifan XIA

Energy harvesting by piezoelectric flags*

Soutenue le 6 novembre 2015 devant le jury composé de :

Rapporteurs :	Benjamin THIRIA	-	Université Paris Diderot
	Olivier THOMAS	-	ENSAM Lille
Directeurs :	Sébastien MICHELIN	-	Ecole Polytechnique
	Olivier DOARÉ	-	ENSTA ParisTech
Examinateurs :	Nigel PEAKE	-	University of Cambridge
	Aurélien BABARIT	-	Ecole Centrale de Nantes

*Récupération d'énergie par drapeaux piézoélectriques

Remerciements

Mes premiers remerciements s'adressent à ma femme, Xiao, que j'aime et qui a toujours su me soutenir pendant les périodes de difficultés et de détresses.

Je remercie mes deux directeurs de thèse, Sébastien Michelin et Olivier Doaré, pour leur encadrement et surtout pour leur patience. Merci de m'avoir guider avec leur grandes disponibilités tout au long de ma thèse. Sans leur enthousiasme et rigueur, cette thèse ne verrait jamais le jour.

Mes remerciements s'adressent également aux membres de jury qui m'ont fait honneur d'être présentés à ma soutenance. Merci à Olivier Thomas et Benjamin Thiria pour leurs rapports et remarques pertinentes sur mon travail. Merci aussi à Nigel Peake et Aurélien Babarit de leur participation à mon jury et de leur questions intéressantes.

Je n'oublierai pas les gens des deux laboratoires où j'ai passé ma thèse. Merci à Jean-Marc Chomaz, et puis à Christophe Clanet pour m'avoir accueilli au LadHyX. Merci à Antoine Chaigne, et puis à Habibou Maitournam pour avoir facilité mon accès à l'UME. Un grand merci à Thérèse, Sandrine, Delphine, et Caroline (que j'ai pu revoir à l'UME après son départ du LadHyX) pour leur gestion impeccable de l'aspect administratif de la vie des doctorants. Je remercie aussi Antoine, Dani, Caroline et Toai pour avoir géré d'une manière efficace le système informatique du LadHyX. Côté l'UME, je remercie Thierry et Nico pour leur disponibilité et patience à m'aider à résoudre de nombreux problèmes que j'ai rencontrés pendant mes expériences.

Merci à Eunok, Chakri, Xavier, Mathieu, Manu, Onofrio, Julien, Tristan, Océane, et tout autres membres du LadHyX d'avoir construit un laboratoire qui possède à la fois une excellence dans la recherche, et une très bonne ambiance que tous ceux qui y ont vécu n'oublieront pas. Merci à Yuan, Julie, Arnaud, Joosung, Corinne, Jean, Romain et Benjamin qui, pendant mes très ponctuels passages Ãă l'UME, m'ont accueilli et m'ont accompagné à l'approche de ma soutenance pour améliorer la qualité de ma présentation. Un merci particulier à Emmanuel et Miguel, avec qui j'ai pu avoir beaucoup d'échanges intéressants, qui d'ailleurs ne sont pas restraints dans le plan de nos recherches.

Enfin, je remercie ma famille, mes parents, qui sont loins mais qui me soutiennent sans faille, et mes amis, sans qui ma vie en France ne serait pas aussi agréable.

Contents

Chapter 1

Introduction

1.1 Overview of flow energy harvesting

The development of techniques that extract energy from flowing air and water dates back to the first century A.D., and lasts to our days [Shepherd 1990]. One of the most ancient and well-developed methods of harvesting energy from wind is the windmills that were widely used during the 17th and 18th centuries in Western Europe (Fig. 1.1*a*). Due to the increasing awareness of the scarcity and non-renewable nature of fossil fuels, windmills attract a renewed attention, and modern wind turbines (Fig. 1.1*b*), based on a similar mechanism of ancient windmills, are being rapidly developed in many countries. Wind turbines generates energy through their rotary propeller, and the driving force of the latter's rotation is not limited to air flow. Novel concepts such as tidal turbines are recently receiving an increasing attention (Fig. 1.1*c*). Tidal turbines work under the same mechanism as wind turbines, with a major difference being that the rotation of their propeller is driven by tidal waves.

The underlying mechanism of harvesting flow energy using both wind and tidal turbines is the solid bodies' motion induced by surrounding fluid flows. The interest of using flow-induced motions of solid bodies as means of energy harvesting also gives rise to a renewed interest in a larger thematics of mechanics, i.e. the fluid-solid interactions, as potential energy-harvesting mechanisms. Many recent works focused on canonical flow-induced vibrations, such as the coupled mode flutter of an airfoil [Peng 2009, Zhu 2012, Boragno 2012], or vortex-induced vibrations of a rigid cylinder or a flexible cable [WEB1 , Bernitsas 2008, Grouthier 2014].

Another canonical and widely studied example of fluid-structure interactions is the flutter instability of flexible plates, or flags. The present work will focus on this phenomenon and explore its potential for energy harvesting.

1.2 Flutter instability

A flexible plate, or a flag, placed in a flow would stay at rest (left, Fig. 1.3) or flap (right, Fig. 1.3) as a result of a competition between its rigidity, which tends to restore the plate to its position of static equilibrium, and the pressure applied by the surrounding flowing fluid, which pushes the plate away from this equilibrium. Another decisive factor for the flutter motion to occur is the flag's inertia: a flag would not flap if it has no inertia.

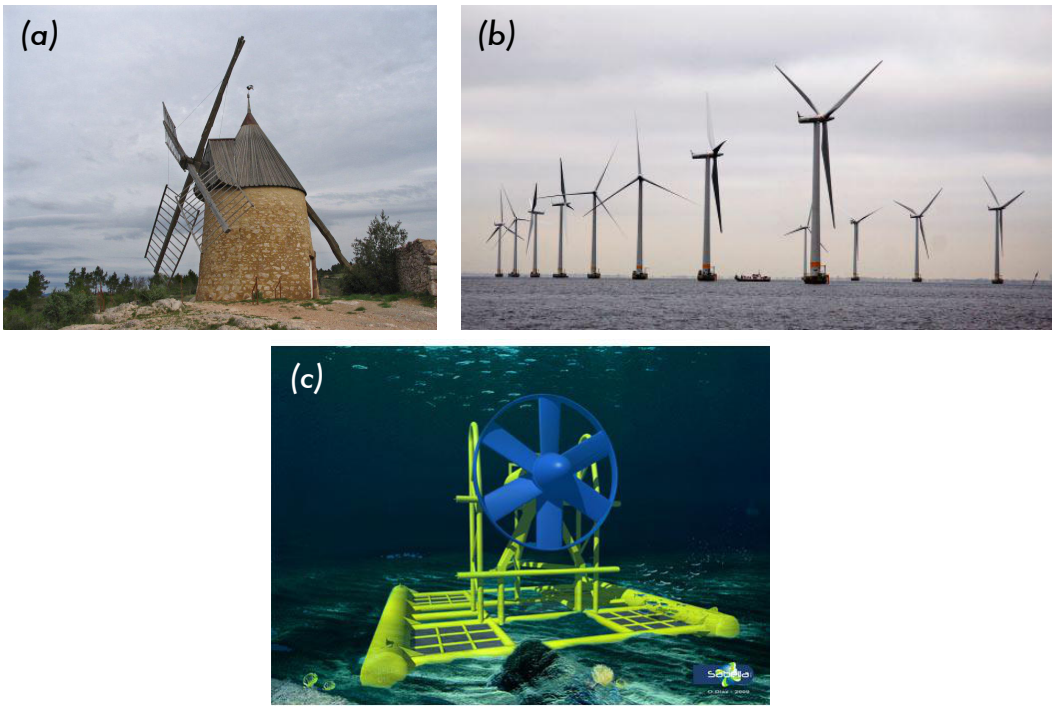

Figure 1.1: (a) A medieval wind mill in Saint-Chinian, France, (b) offshore wind turbines of Vattenfall company and (c) artistic view of a tidal turbine by SABELLA (Source: WEB).

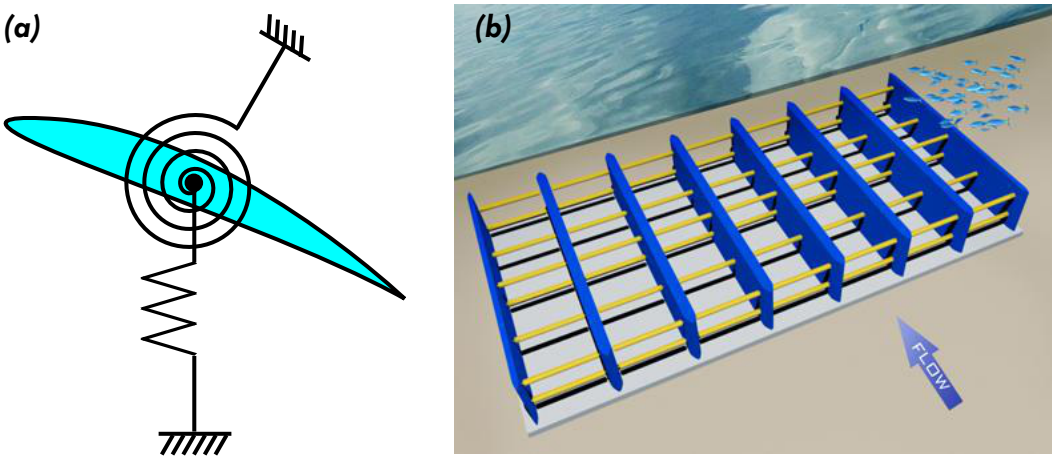

Figure 1.2: (a) Schematic representation of an airfoil and (b) VIVACE, an energy-harvesting device based on vortex-induced vibration [WEB1].

Figure 1.3: National flags at rest (left, photo taken during COP10 in Nagoya, Japan, 18–29, Oct. 2010, courtesy to Malaka Rodrigo) and flapping (right, Source: web)

Compared with previously mentioned flow-induced motions, such as the airfoil flutter or the vortex-induced vibration (VIV) of rigid cylinders, which are motions of rigid bodies involving only a limited number (usually 1 or 2) of degrees of freedom, the flexibility of the flag induces large deformations of the structure itself, thus a large number of degrees of freedom. The dynamics of a flag flapping in a flow is influenced not only by the velocity and direction of the incoming flow, but also by the physical properties of the flag, including its dimension and material characteristics. In terms of modelling, due to the large number of degrees of freedom, this problem involves a strong coupling of governing equations of both fluid dynamics and elasticity, hence the difficulty of solving this problem.

The earliest works on this problem are mainly experimental studies [Taneda 1968] with theoretical analysis using the potential flow theory [Wu 1961, Kornecki 1976]. Recently, with the advent of powerful scientific computing tools and sophisticated experimental techniques, the flutter instability of a flag receives an unprecedented popularity among researchers in the field of both fluid and solid mechanics. One may divide existing works into two main categories: studies of the stability and dynamics of a single flexible plate, and those of several flexible plates in a uniform flow.

1.2.1 Stability and dynamics of a single flag placed in a uniform flow

A great number of researchers have reported studies on stability and dynamics of a single flag placed in a uniform flow [Huang 1995, Eloy 2007, Shelley 2011]. In their experimental studies, Zhang *et al.* [Zhang 2000] observed the motion of a filament in a 2D flow generated by a soap-film. They observed that depending on the length of the filament, it has two fundamental states: (i) the stretched-straight state when the length is small, and (ii) the flapping state when the length is large. They also observed the evolution of the flapping amplitude and frequency with the filament's length, and identified a hysteresis phenomenon by increasing and reducing the filament's length. Watanabe *et al.* investigated experimentally the paper flutter

using different materials [Watanabe 2002b], and also developed theoretical models to account for various observations in the experiments [Watanabe 2002a]. In both studies, relations between the flutter speed and the mass ratio, i.e. the ratio between the inertia of the fluid and solid, are identified. Other experimental and theoretical works also investigated the stability [Lemaitre 2005] and post-critical dynamics [Eloy 2012, Virot 2013, Gibbs 2014] of a flag placed in a wind tunnel and offered a vast catalogue of flutter properties of flags made of different materials, such as paper, plastic, fabrics, and metals.

Recently, with the increasing capacity of scientific computing, a large amount of numerical work has been conducted to study the flapping of a flag. The experiments of Zhang et al. were reproduced by direct numerical simulation using immersed boundary method (IBM) [Zhu 2002] and arbitrary Lagrangian Eulerian (ALE) [Sawada 2006]. Both numerical methods gave results that are in a good qualitative agreement with the experimental results: (i) stretched-straight state is observed with short flags, (ii) bistability–switching between the stretched-straight state and flapping state–is observed for longer flags.

Despite the benefit that the direct numerical simulation provides a detailed description of the dynamics of both the flow and the structure, it is time-consuming and prohibitive for high Reynolds numbers. As a result, many simplified models are developed to carry out faster simulations. A very popular model for describing the dynamics of a flag is the inextensible Euler-Bernoulli beam model, while a variety of models for the fluid flow, based on the inviscid flow assumption and incompressibility, are used by different researchers. Alben *et al.* used a flexible body vortex sheet model to compute the fluid forcing and the flow field around a flapping 2D flag [Alben 2008a]. They reported that in addition to the two previously mentioned states: i.e. the stretched-straight and periodic flapping states, a chaotic state, characterised by undefined amplitude and frequency, may appear when the incoming flow velocity is much larger than the critical velocity. Using a unsteady point vortex model, Michelin *et al.* also identified the existence of this chaotic state [Michelin 2008].

The experimental and numerical techniques for studying a 2D flag in a uniform 2D incoming flow are well developed and have been providing interesting insights of flag's flapping dynamics. However, the major drawback of these techniques is that they consider flags of an infinite span, which is unrealistic. Many studies therefore also focus on 3D effects on the flapping flag. In their work, Eloy *et al.* highlighted that the flag's span has a significant influence on the flag's stability [Eloy 2007]: with a fixed flag's length, the onset of flapping takes place at a lower velocity for a flag with larger span. This conclusion is supported by the study of Gibbs *et al.* [Gibbs 2012], in which experiments are performed and a stability analysis is carried out using the Euler-Bernoulli beam model to describe the flag, and a vortex lattice model [Tang 2007] to account for fluid loading. Another model for the fluid forcing, called *Large-Amplitude Elongated-Body Theory* (LAEBT), initially developed as to describe fish locomotion [Lighthill 1971, Candelier 2011], is recently adapted to the case of 3D flapping flags [Singh 2012b, Eloy 2012, Michelin 2013]

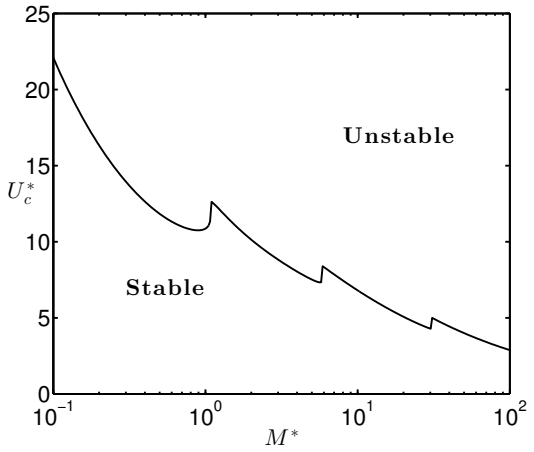

Figure 1.4: Evolution of the critical velocity U_c^* as a function of M^*. A flag with a given M^* becomes unstable if the flow velocity exceeds U_c^* (Figure obtained using the method presented in Chapter 3).

by adding drag terms corresponding to the dissipation induced by the lateral flow separation due to the finite flag span. Meanwhile, DNS techniques are also developed for 3D simulations using both IBM [Tian 2012] and ALE [Bourlet 2015].

In many recent studies, a uniform, inviscid, incompressible flow and the Euler-Bernoulli beam model are used to investigate the flag's flapping in a flow. Using these models, the system is controlled by three dimensionless parameters: the mass ratio M^*, the reduced velocity U^*, and the aspect ratio H^*. These parameters are defined as:

$$M^* = \frac{\rho_f^s L}{\mu}, \quad U^* = U_\infty L \sqrt{\frac{\mu}{B}}, \quad H^* = \frac{H}{L}, \tag{1.1}$$

where ρ_f^s and μ are respectively the fluid's mass per unit surface and the flag's mass per unit length, L is the length of the flag, U_∞ is the incoming flow velocity, B is the flag's bending rigidity, and H is the flag's span. Note that in the 3D case, $\rho_f^s = \rho_f H$, with ρ_f representing the fluid's density. Regardless of the various models used in different works, a widely approved conclusion is that for a flag with a given aspect ratio H^* ($H^* = \infty$ in 2D cases), larger mass ratio M^* leads to lower critical velocity in terms of U^*, as shown in Fig. 1.4.

When $U^* < U_c^*$, the flag is stable and stays in the stretched-straight state. Once $U^* > U_c^*$, the flag becomes unstable and reaches either a periodic flapping state (Fig. 1.5*a*, *b*), or a chaotic flapping state depending on the flow velocity (Fig. 1.5*c*, *d*).

Another aspect involved in the studies of a single flag in a uniform flow is the effect of walls. Mainly three configurations are under active investigation: (i) the close presence of one single rigid wall parallel to the flag's plane [Nuhait 2010, Dessi 2015], (ii) the close presence of two rigid walls parallel to the flag's plane, thus forming a transverse confinement [Belanger 1995, Guo 2000, Alben 2015], and (iii) the close presence of two rigid walls orthogonal to the flag's plane, therefore forming a span-

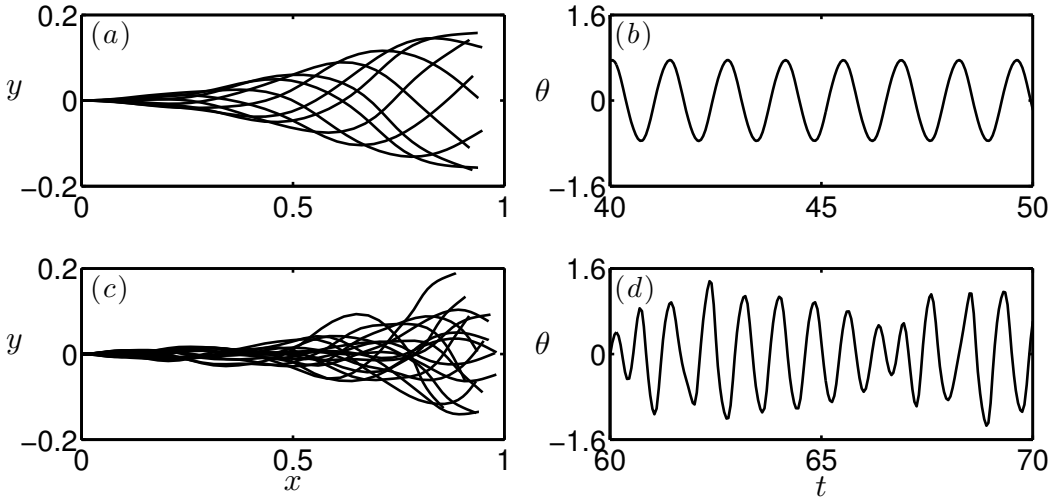

Figure 1.5: (a, c)Flapping motions and (b, d) of the flag's trailing edge orientation θ at (a, b) periodic flapping state with $M^* = 10$, $U^* = 9$ and (c, d) chaotic flapping state with $M^* = 10$, $U^* = 18$.

wise confinement [Doaré 2011b, Doaré 2011c]. These studies showed that the presence of one or two walls in the vicinity of the flag has a destabilising effect, i.e. the confinement reduces the critical velocity. Some studies also reported that the confinement leads to an increase of the flag's added mass [Belanger 1995, Guo 2000]. Post-critical behaviour of a flag in a transverse confinement is also studied numerically by Alben [Alben 2015], who found that while decreasing the channel wall distance from infinity, the flapping amplitude starts by increasing, then decreases because it is limited by the wall. Note that in a wind tunnel test with a flag, both transverse and spanwise confinements may exist depending on the size of the wind tunnel's test section.

1.2.2 Stability and dynamics of several flags placed in uniform flow

Studying the coupled motion of several flexible bodies placed in a flow is motivated by natural phenomena, particularly the fish schooling [Cushing 1968]. Weihs [Weihs 1973] pointed out that in a 2D plane, the optimal positioning of each fish in a school should have a diamond pattern (Fig. 1.6) so that the fish that follow others would profit from the thrust induced by the oscillatory motion of their predecessors.

The constantly improving techniques for studying a single flag's flapping are providing new methods to fulfil researchers' motivation in studying the flapping of multiple flags. Zhang *et al.* conducted experiments using two filaments placed side by side in a 2D flow based on a soap film [Zhang 2000]. Their results show that under the same incoming flow, two filaments flap in an in-phase pattern (two flags

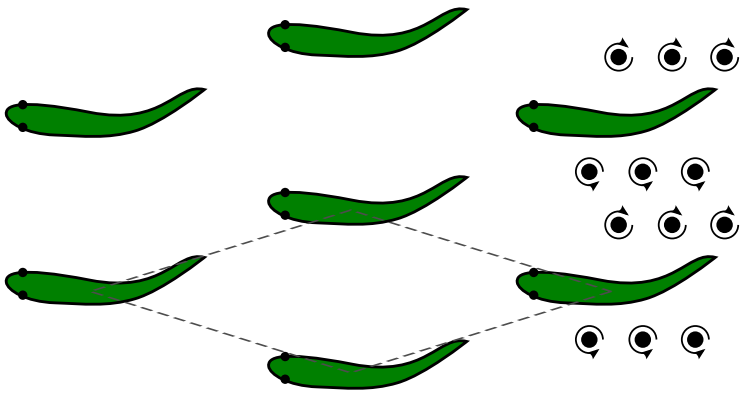

Figure 1.6: Horizontal layer of fish in a school, from above. The diamond pattern is shown with the dashed line (Adapted from [Weihs 1973])

.

have the same vertical displacement) when the distance separating them is small. The flapping becomes out of phase (two flags have the opposite vertical displacement) when the two filaments are moved away from each other. The observation of the two flapping patterns, i.e. the out-of-phase one and the in-phase one, is also reproduced by numerical simulations of parallel 2D flags [Zhu 2003, Farnell 2004]. Using the vortex sheet model and the Euler-Bernoulli beam, Alben [Alben 2009b] reported that the phase difference between two side-by-side 2D flags evolves almost monotonically with the distance separating them.

Jia *et al.* [Jia 2007] performed more thorough experimental investigations of two identical side-by-side filaments placed in a flowing soap film, and studied theoretically their linear stability. They suggest that the coupled dynamics of two filaments is subject to three dimensionless parameters: the mass ratio M^*, the reduced velocity U^*, and the dimensionless form of the separation distance d, defined by:

$$d = \frac{D}{L}, \tag{1.2}$$

where D is the dimensional form of the separation distance. According to the variation of these parameters, four flapping modes may be identified: (i) the stretched-straight mode, (ii) in-phase mode, (iii) out-of-phase mode, and (iv) an indefinite mode, i.e. a phase difference switching between 0 and π. Using a double-wake model, Michelin & Llewellyn Smith [Michelin 2009] studied the linear stability of two side-by-side flags and observed that a decreasing d induces to a destabilising effect, thereby lowering the critical velocity U_c^*. Wang *et al.* [Wang 2010] performed wind tunnel tests with two identical flags placed side by side and confirmed this destabilisation. In addition, they found that when d is too small ($d < 0.2$), U_c^* actually becomes much higher than the critical velocity of one single flag. They argue that the very small d actually makes the two flags to behave as one single flag of a larger thickness, thus a higher flow velocity is required to destabilise the system.

Another basic configuration involving two flags placed in tandem is also studied.

Still using filaments in soap-film flow, Jia & Yin [Jia 2008] performed experiments with two filaments placed in tandem, i.e. one filament is placed directly downstream to the other. They investigated flapping patterns and the energy distribution of two filaments by varying the separation distance. Their results show that the downstream filament experiences a drafting induced by the wake of the upstream filament. As a result of the drafting, the drag force on the downstream filament is reduced. Ristroph & Zhang [Ristroph 2008] also conducted experimental work using a soap film and two filaments placed in tandem but found a result opposite to Jia & Yin: the upstream filament actually experiences an inverted drafting. The drag applied on the upstream flag is lower than the drag on the downstream flag. The reason that they found opposite results lies probably in the different leading edge conditions used in these two studies: in [Jia 2008], the upstream filament is fixed at its leading edge, while the leading edge of the downstream filament is tethered by a silk fibre fixed at the other end; in [Ristroph 2008], both flags have a fixed leading edge. The inverted drafting is confirmed by Alben [Alben 2009b] using a vortex sheet model, while Kim *et al.* [Kim 2010], using an improved version of IBM, reported that both drafting and inverted drafting can be observed depending on the phase difference of both flags' vortex shedding.

During the last decade, an increasing number of researchers are interested in the coupled dynamics of three or more flexible bodies in uniform flow. Schouveiler *et al.* [Schouveiler 2009] performed wind tunnel tests with three and four side-by-side flags. Their work reported three possible flapping modes of three flags: (i) in-phase mode, i.e. all three flags have the same vertical motion, (ii) out-of-phase mode, i.e. two consecutive flags have opposite vertical motions, and (iii) symmetrical mode, i.e. the flag in the middle is stretched-straight, while the other two have opposite vertical motions. Michelin & Llewellyn Smith [Michelin 2009] extended the double-wake method to three and more side-by-side flags and investigated their linear stability: for the case of three flags, they also found the three modes reported in [Schouveiler 2009], and for the case of an infinite number of flags, the out-of-phase mode is found to be the dominant one for small M^* and large d, while for other parameters, the authors reported the existence of modes with the phase difference of any value between 0 and π.

1.2.3 Concluding remarks: why we choose piezoelectric flags

The choice of the flag's flutter instability as an energy-harvesting mechanism is motivated by its periodic, large-amplitude post-critical motion, which is the main feature of the the flag's flapping dynamics. Such motion involves a permanent energy exchange between the flags and the surrounding fluid. Many researchers are getting interested in this energy exchange and are seeking ways to harvest energy from it. In general, energy harvesting based on flapping flags may follow two routes: producing energy either from the displacement [Tang 2008, Virot 2015] or from the deformation of the flag [Allen 2001, Singh 2012a]. The latter route has recently been the focus of several studies based on active materials [Doaré 2011a, Dunnmon 2011,

Giacomello 2011, Akcabay 2012, Michelin 2013]. In our work, we will be interested in piezoelectric materials. The piezoelectric material is chosen in this work for its property of converting a part of mechanical energy generated from mechanical deformation to the electrical energy. In the next section, a brief introduction to piezoelectricity will be presented.

1.3 A brief introduction to piezoelectricity

Piezoelectric materials, as the name indicates, give an "electric" response under "pressure". More precisely, such materials produce electric charge displacement when they are deformed. The discovery of piezoelectricity is attributed to Jacques & Pierre Curie [Curie 1880a, Curie 1880b]. However, their work in 1880 only revealed one piezoelectric effect, the effect that generates electric charge from the material's deformation, since called **direct piezoelectric effect**. The other effect, called **inverse piezoelectric effect** remained in shadow at that time until one year later another French physicist, Gabriel Lippmann, who announced that according to the principle of electric charge conservation, a piezoelectric crystal should experience a slight deformation under the influence of an external electric field [Lippmann 1881], a conclusion that, although based solely on mathematical arguments, was experimentally confirmed in the same year by Jacques & Pierre Curie [Curie 1881].

In 1880, the Curie brothers published their work with the following statement [Curie 1880b]:

> *Quelle que soit la cause déterminante, toutes les fois qu'un cristal hémièdre à faces inclinées, non conducteur, se contracte, il y a formation de pôles électriques dans un certain sens; toutes les fois que ce cristal se dilate, le dégagement d'électricité a lieu en sens contraire.*

In this paragraph written in French, the Curie brothers, studying only the quartz, a naturally piezoelectric crystal, reached the conclusion that the reason of electric charge generation under deformation is the formation of electric dipoles within the material itself. This conclusion applies to almost all known piezoelectric materials, though the origin of electrical dipoles varies according to the specific category where a material lies [WEB2 , Ramadan 2014].

Knowing that electrical dipoles are the origin of piezoelectricity, we are able to describe in a qualitative way how the direct and inverse piezoelectric effects are produced. On one hand, without any deformation, a piezoelectric material is electrically neutral, implying that its centres of both positive and negative charges coincide. These two centres would be separated if the material is stretched, compressed, or sheared, creating an electrical field within the material, therefore a voltage difference is generated. An electric charge displacement would occur if the material's positive side and negative side are connected with a conductive wire, hence the direct piezoelectric effect. On the other hand, an externally applied electric field would disrupt the electrical neutrality of a piezoelectric material. In order to restore the neutrality,

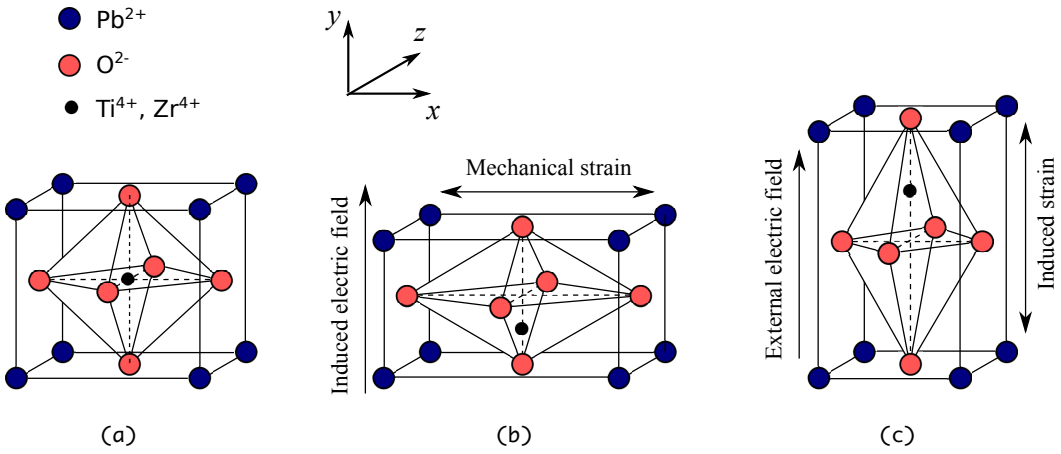

Figure 1.7: (*a*) Elementary cell structure of PZT and piezoelectric effects: (*b*) direct piezoelectric effect and (*c*) inverse piezoelectric effect (adapted from [WEB2 , Thomas 2011]).

the initially coinciding positive and negative centres would repulse each other as to create an electric field that compensates the external one. As a result, a mechanical deformation occurs, and an additional stress is induced due to the material's elasticity, hence the inverse piezoelectric effect.

Take the elementary crystal structure of PZT (Lead zirconate titanate) for example. Figure 1.7*a* shows that when the structure is neutral, its centres of positive and negative charges are at the same point. When a mechanical strain on the x direction is applied on the structure (Fig. 1.7*b*), these two centres are moved away from each other, in the y direction, thus creating an electric field directing from the positive centre to the negative centre. If an external electric field following the increasing y direction is applied on the structure, in order to restore the electric neutrality within the structure, the centres of positive and negative charges will move towards opposite directions, inducing consequently a deformation of structure.

Existing piezoelectric materials can fall into four categories: quartz, ceramics, polymers, and composites [Vijaya 2012].

Quartz

Quartz is the crystalline form of silicon dioxide, and it is a naturally occurring piezoelectric material. Besides a strong piezoelectricity, the quartz also possesses other interesting characteristics such as high stiffness, long life, and low sensitivity to temperature and other environmental changes, which makes it an ideal choice for devices requiring a precise frequency control, such as electronic watches, clock signal generators for computers and microprocessor-based instruments. However, its high stiffness and fragility also make it unsuitable for applications involving large deformation. Also, its unique crystalline structure makes it difficult to be shaped

into desired forms.

Ceramics

Piezoelectric ceramics, such as PZT and Barium Titanate, are ferroelectric materials that hold excellent piezoelectric properties. Although quartz has relatively stronger piezoelectricity than ceramics, an advantage of ceramics over quartz is that ceramics are prepared in the form of powder and can therefore be easily shaped into any required geometries, such as discs, cylinders, plates, or thin films, which makes them more widely used for actuator and transducer applications. However, their applications are also limited by their high stiffness and brittleness.

Polymers

The most commonly known and widely used piezoelectric polymer is the Polyvinylidene Fluoride (PVDF). Polymers offer rather weak piezoelectricity compared with quartz and ceramics, but have a special advantage that they are flexible and mechanically more stable. They are usually obtained in the form of large-area thin films which can afterwards be cut into any required dimension. Their excellent flexibility makes them a perfect choice for applications involving large deformation and therefore will be used in the present work.

Composite piezoelectric materials

Composite piezoelectric materials are usually made of piezoelectric ceramics, offering strong piezoelectric effects, and softer materials such as polymer or resin that help to improve the material's flexibility. As a result, composite piezoelectric materials are also interesting candidates when large deformations are required. This material will also be tested in the present work.

1.4 Energy harvesting using piezoelectric materials

Due to their ability of converting the energy associated with mechanical deformation into the electrical energy, piezoelectric materials have been extensively studied in applications of vibration control or suppression [Hagood 1991, Bisegna 2006, Thomas 2009, Thomas 2011, Ducarne 2012]. In recent years, many publications on energy-harvesting techniques based on piezoelectric materials start to appear, and this section will be dedicated to a brief review of the existing work.

The concept of piezoelectric energy generator emerged around two decades ago [Williams 1996, Umeda 1996]. Its basic idea is to convert ambient vibration energy to useful electrical energy through piezoelectric materials implemented on vibration sources. Many researchers have contributed to this field in order to improve the efficiency of such energy-harvesting systems [Sodano 2004, Anton 2007, Erturk 2011, Caliò 2014]. Some studies show that simple resonant circuits, i.e.

resistive-inductive circuits combined with the piezoelectric material's intrinsic capacitance [Yang 2005], offer promising opportunities to achieve high efficiency [Shenck 2001, De Marqui 2011].

Flow energy harvesting can be achieved by exploiting the unsteady forcing of the vortex wake generated by an upstream bluff body to force the deformation of a piezoelectric membrane [Allen 2001, Taylor 2001, Pobering 2004]. Fluid-solid instabilities offer a promising alternative as they are able to generate spontaneous and self-sustained structural deformation of the piezoelectric structure, e.g. cross-flow instabilities [Kwon 2010, De Marqui 2011, Dias 2013]. In their work, De Marquis *et al.* [De Marqui 2011] used a resistive circuit and a resistive-inductive one, and found in addition to the beneficial effect of the resonance to the energy harvesting, that a resistive-inductive circuit may also affect the stability of the vibration source. However, the resonant circuit's influence on the structure's dynamics was not reported in this work.

Some researchers have already worked on piezoelectric flags [Dunnmon 2011, Doaré 2011a, Akcabay 2012, Michelin 2013]. In particular, Doaré & Michelin [Doaré 2011a, Michelin 2013] considered a piezoelectric flag coupled with a purely resistive output. They observed moderate efficiency, which is maximised when the characteristic timescale of the circuit is tuned to the frequency of the flag. A significant impact of the circuit's properties on the fluid-solid dynamics was also identified.

1.5 Introduction of numerical models used in the present work

1.5.1 Modelling of the fluid-structure system

In our study, we are interested in the configuration illustrated in Fig. 1.8 (left), where a flag of length L and height H is placed in an uniform flow of velocity U_∞.

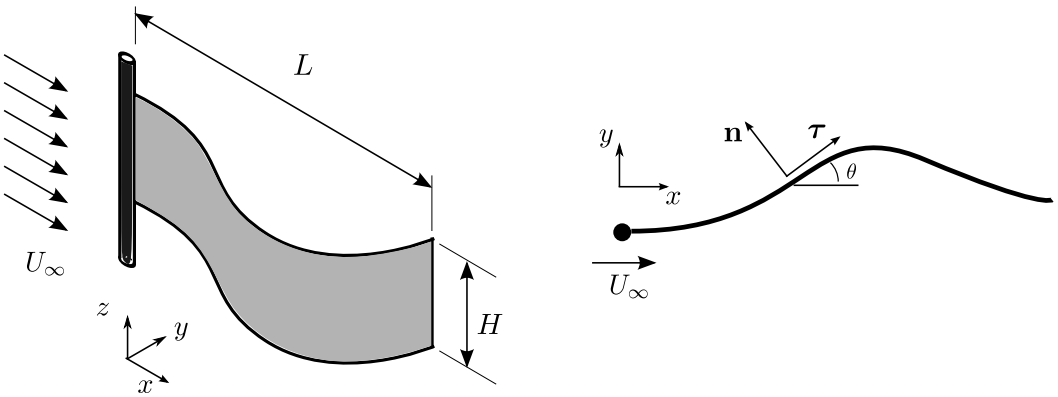

Figure 1.8: (left) A schematic representation of a flag flapping in an axial flow and (right) the view in $x-y$ plane, where the flag's motion takes place.

This representation is again simplified by posing two kinematic assumptions:

- the flag's motion is confined exclusively in the (x, y) plane (Fig. 1.8, right), i.e. all motions depending on the z direction are neglected;
- the flag is inextensible, i.e. the flag cannot be stretched or shortened.

Under these two assumptions, the flag's motion consists simply on a bending along the z direction, and consequently the Euler-Bernoulli beam model is used to describe the flag's dynamics [Antman 1995]. This model is given as follows:

$$\mu \frac{\partial^2 \mathbf{x}}{\partial t^2} = \frac{\partial}{\partial s}\left(T\boldsymbol{\tau} - \frac{\partial \mathcal{M}}{\partial s}\mathbf{n}\right) + \mathbf{F}_{\text{fluid}}, \tag{1.3}$$

$$\frac{\partial \mathbf{x}}{\partial s} = \boldsymbol{\tau}. \tag{1.4}$$

Equation (1.3) shows that the flag's displacement $\mathbf{x}$, a function of the Lagrangian coordinate s and time t, is influenced by three actions: the tension T along s, which also ensures the flag's inextensibility, the bending moment $\mathcal{M}$, which depends on the flag's bending rigidity B as well as the local curvature, and the fluid forcing $\mathbf{F}_{\text{fluid}}$. With the constitutive law of Euler-Bernoulli beam, the bending moment B is given by:

$$\mathcal{M} = B\frac{\partial \theta}{\partial s}. \tag{1.5}$$

Appropriate boundary conditions are required to complete Eq. (1.3). The boundary conditions that will be considered in the present work are the so-called *clamped-free boundary conditions*. These boundary conditions stipulate that the fixed end, or the leading edge of the flag in our work, is "clamped", meaning that neither displacement nor rotation is allowed. At the same time, the free end, or the trailing edge of the flag in our work, is not constrained by any external object apart from the flag itself. This condition entails the cancellation of three quantities at the trailing edge: the normal tension T, the bending moment $\mathcal{M}$, and its first derivative in space, representing the shear force on the flag's cross section.

$$\text{at} \quad s = 0 : \ \mathbf{x} = \theta = 0, \tag{1.6}$$

$$\text{at} \quad s = L : \ T = \mathcal{M} = \frac{\partial \mathcal{M}}{\partial s} = 0. \tag{1.7}$$

Equation (1.4) represents the inextensibility condition, which implies that the tension T is computed, using the boundary condition given by Eq. (1.7), by integrating the tangential component of Eq. (1.3) from $s = L$:

$$T(s,t) = \int_L^s \left(\mu \frac{\partial^2 \mathbf{x}}{\partial t^2} \cdot \boldsymbol{\tau} - B\frac{\partial \theta}{\partial s}\frac{\partial^2 \theta}{\partial s^2} - \mathbf{F}_{\text{fluid}} \cdot \boldsymbol{\tau}\right) \mathrm{d}s' \tag{1.8}$$

The previously mentioned LABET is chosen to model the fluid loading $\mathbf{F}_{\text{fluid}}$. In the limit of slender structures ($H \ll L$), Lighthill [Lighthill 1971] provides a leading

order expression for the "reactive force" $\mathbf{F}_{\text{react}}$ which is computed from the relative velocity of the flag to the incoming flow:

$$U_n\mathbf{n} + U_\tau\boldsymbol{\tau} = \frac{\partial \mathbf{X}}{\partial t} - U_\infty \mathbf{e}_x. \tag{1.9}$$

The reactive force can then be derived by computing the advection of the fluid added momentum by the flow, which is an inviscid effect. Here, instead of presenting the rigorous proof of the LAEBT [Lighthill 1960, Lighthill 1970, Lighthill 1971], we only show a simplified derivation of the reactive force expression in terms of momentum conservation.

Assuming that the flag's motion is confined in the $x-y$ plane, we consider two planes $\Pi(s)$ and $\Pi(s+\mathrm{d}s)$, both perpendicular to the $x-y$ plane, intersecting the flag at s and $s+\mathrm{d}s$, thus defining a segment of length $\mathrm{d}s$ on the flag along its streamwise direction. We then compute the momentum variation of the fluid flow passing across the zone confined by the planes $\Pi(s)$ and $\Pi(s+\mathrm{d}s)$ (See Fig. 1.9 for notations).

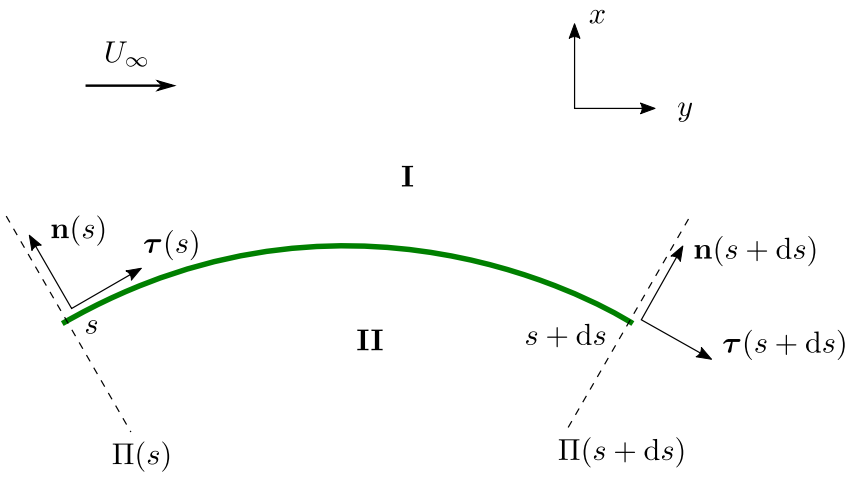

Figure 1.9: Configuration used for reactive force derivation.

Lighthill pointed out that the essential characteristic of an "elongated body" is that the fluid added mass with respect of the relative motion in the normal direction $\mathbf{n}$ is large, whereas in the tangential direction $\boldsymbol{\tau}$, the added mass is small [Lighthill 1971]. As a result, the reactive force is principally due to the variation of the normal component of the fluid's added momentum $\mathbf{p}_n$ in the volume defined by $\mathbf{I}+\mathbf{II}$. The expression of $\mathbf{p}_n$ is given by:

$$\mathbf{p}_n(s) = M_a U_n(s)\mathbf{n}(s)\mathrm{d}s, \tag{1.10}$$

where $M_a = m_a \rho_f H^2$ is the added mass of the fluid surrounding the flag, and we choose $m_a = \pi/4$, which is the added mass coefficient for a rectangular plate of

width H [Lighthill 1971]. The local conservation of $\mathbf{p}_n(s)$ in the volume $\mathbf{I}+\mathbf{II}$ is given by the following expression:

$$\frac{\partial}{\partial t}(M_a U_n \mathbf{n}) = \frac{\partial}{\partial s}(M_a U_n U_\tau \mathbf{n}) - \frac{1}{2}\frac{\partial}{\partial s}(M_a U_n^2 \boldsymbol{\tau}) - \mathbf{F}_{\text{react}}. \tag{1.11}$$

The three terms on the right-hand side of Eq. (1.11) represent three contributions to the normal momentum variation, which are:

- the advection by the flow along the tangential direction $\boldsymbol{\tau}$;
- the difference of the fluid pressure acting on $\Pi(s)$ and $\Pi(s+\mathrm{d}s)$ along the tangential direction $\boldsymbol{\tau}$, which, according to [Lighthill 1970] can be obtained using Bernoulli's theorem;
- the flag's force as a reaction to the fluid pressure, which is the opposite of the reactive force, thus noted as $-\mathbf{F}_{\text{react}}$.

Using the following relations:

$$\frac{\partial \mathbf{n}}{\partial t} = -\frac{\partial \theta}{\partial t}\boldsymbol{\tau}, \quad \frac{\partial \mathbf{n}}{\partial s} = -\frac{\partial \theta}{\partial s}\boldsymbol{\tau}, \quad \frac{\partial \boldsymbol{\tau}}{\partial s} = \frac{\partial \theta}{\partial s}\mathbf{n}, \tag{1.12}$$

we can rewrite Eq. (1.11) into the following form:

$$\mathbf{F}_{\text{react}} = -M_a\left(\frac{\partial U_n}{\partial t} - \frac{\partial}{\partial s}(U_n U_\tau) + \frac{1}{2}U_n^2\frac{\partial \theta}{\partial s}\right)\mathbf{n} + U_n\left(\frac{\partial \theta}{\partial t} - U_\tau\frac{\partial \theta}{\partial s} - \frac{\partial U_n}{\partial s}\right)\boldsymbol{\tau}. \tag{1.13}$$

By calculating the time derivative of Eq. (1.9), and using the inextensibility condition of Eq. (1.4), we may obtain the following result:

$$\frac{\partial \theta}{\partial t} - U_\tau\frac{\partial \theta}{\partial s} - \frac{\partial U_n}{\partial s} = 0, \tag{1.14}$$

thus cancelling the tangential component in Eq. (1.13). Replacing M_a by $m_a\rho_f H^2$ in Eq. 1.13, we obtain therefore the expression of the reactive force:

$$\mathbf{F}_{\text{react}} = -m_a\rho_f H^2\left[\frac{\partial U_n}{\partial t} - \frac{\partial}{\partial s}\left(U_n U_\tau\right) + \frac{1}{2}U_n^2\frac{\partial \theta}{\partial s}\right]\mathbf{n}. \tag{1.15}$$

Candelier *et al.* [Candelier 2011] recently proposed an analytic proof of this result, and successfully compared it to RANS simulations for fish locomotion problems. These authors also stated that in the case of spontaneous flapping, it is necessary to account for the effect of lateral flow separation, which is a 3D effect. Here, we choose an empirical "resistive" force model given by the following term [Taylor 1952, Eloy 2012, Singh 2012b]:

$$\mathbf{F}_{\text{resist}} = -\frac{1}{2}\rho H C_d |U_n| U_n \mathbf{n}, \tag{1.16}$$

where $C_d = 1.8$ is the drag coefficient for a rectangular plate in transverse flow [Buchak 2010]. Note that in [Taylor 1952], the resistive force had two additional

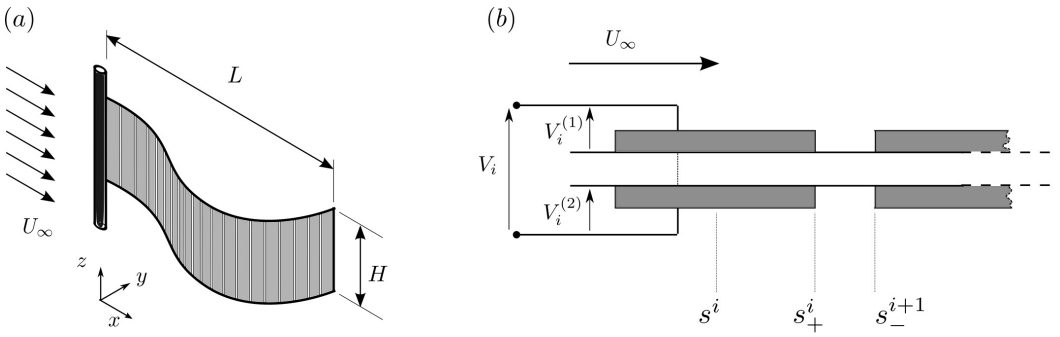

Figure 1.10: (a) Schematic representation of a flag covered by straps of piezoelectric materials and (b) schematic view of pairs of piezoelectric patches.

terms that account for the skin friction, which is irrelevant to the present work. The fluid forcing is the sum of these two terms:

$$\mathbf{F}_{\text{fluid}} = \mathbf{F}_{\text{react}} + \mathbf{F}_{\text{resist}}. \tag{1.17}$$

The applicability of this result to flapping flag was confirmed experimentally, at least up to an aspect ratio $H^* = 0.5$, the value considered in our work [Eloy 2012].

We may notice that the viscous effect is neglected in the above model. This assumption is justified by the fact that the flapping flag dynamics considered here implies a large Reynolds number. A 10 cm long/wide flag in a wind flowing at around 5 m/s, or a water current of around 0.5 m/s leads to $Re \sim 10^4$. Such order of magnitude of Re can also be obtained using configurations of existing experimental works [Eloy 2012, Virot 2013].

1.5.2 Piezoelectric effects

The surface of the flag is covered by piezoelectric patches (Fig. 1.10a). These patches are placed by pairs, i.e. every patch on one surface is paired with an identical one on the opposite surface. The left and right ends of the i^{th} pair are respectively denoted by s_i^- and s_i^+ (Fig. 1.10b). When deformed, each patch generates an electric charge displacement Q_i^k due to the direct piezoelectric effect. This quantity is given by the following equation [Ducarne 2012]:

$$Q_i^{(k)} = \chi[\theta]_{s_i^-}^{s_i^+} + \mathcal{C}^{(k)} V_i^{(k)}, \tag{1.18}$$

where χ is a mechanical/electrical conversion factor quantifying the proportion of the flag's deformation energy being converted to the electrical energy. $V_i^{(k)}$ is the voltage difference between the two electrodes of the i^{th} piezoelectric patch. And $\mathcal{C}_i^{(k)}$ is the intrinsic capacity of the i^{th} piezoelectric patch [Erturk 2009]. Equation (1.18) applies to both patches in the i^{th} piezoelectric pair. The superscript k takes values 1

or 2, indicating one surface and the other of the flag (Fig. 1.10*b*). If the two patches are connected in series in the same loop, with reversed polarity, the consequence is that since each patch experiences a deformation opposite to the other, the same quantity of electric charge passes through these two patches in the same direction, and that the same voltage is applied on each patch. If Q_i and V_i denote respectively the electric charge and the voltage of the i^{th} piezoelectric pair, we obtain following expressions:

$$Q_i = Q_i^{(1)} = Q_i^{(2)} \tag{1.19}$$

$$V_i = 2V_i^{(1)} = 2V_i^{(2)} \tag{1.20}$$

Also, since two patches are identical, they have the same intrinsic capacity. The equivalent capacity of the i^{th} pair, as a result of a connection in series, is half of the intrinsic capacity of each patch:

$$\mathcal{C}_i = \frac{\mathcal{C}_i^{(1)}}{2} = \frac{\mathcal{C}_i^{(2)}}{2} \tag{1.21}$$

The inverse piezoelectric effect, i.e. the elastic stress induced by an external voltage, is modelled as an additional torque applied on the segments of the flag that are covered by piezoelectric pairs [Thomas 2009]:

$$\mathcal{M}_{\text{piezo}} = -\sum_i \chi V_i F_i \tag{1.22}$$

where the function F is defined as:

$$F_i(s) = \begin{cases} 1 & \text{if } s_i^- < s < s_i^+ \\ 0 & \text{if elsewhere} \end{cases} \tag{1.23}$$

Piezoelectric effect therefore adds a new contribution on the bending moment applied on the flag, which is now written as:

$$\mathcal{M} = B\frac{\partial\theta}{\partial s} - \sum_i \chi V_i F_i. \tag{1.24}$$

Finally, a relation exists between the electric charge Q_i and the voltage V_i, which depends on our choice of external circuits. This relation will for now be written in its generic form as:

$$F(V_i, Q_i) = 0 \tag{1.25}$$

The complete system of equations describing a flag covered by a finite number of piezoelectric patches is therefore given by:

$$\mu\frac{\partial^2\mathbf{x}}{\partial t^2} = \frac{\partial}{\partial s}\left[T\boldsymbol{\tau} - \frac{\partial}{\partial s}\left(B\frac{\partial\theta}{\partial s} - \sum_i \chi V_i F_i\right)\mathbf{n}\right] + \mathbf{F}_{\text{fluid}}, \tag{1.26}$$

$$Q_i = \chi[\theta]_{s_i^-}^{s_i^+} + \mathcal{C}_i V_i, \tag{1.27}$$

$$F(V_i, Q_i) = 0. \tag{1.28}$$

And the clamped-free boundary conditions are given by:

$$\text{at} \quad s = 0 : \ \mathbf{x} = \theta = 0, \tag{1.29}$$

$$\text{at} \quad s = L : \ T = B\frac{\partial \theta}{\partial s} - \chi V = B\frac{\partial^2 \theta}{\partial s^2} = 0. \tag{1.30}$$

1.5.3 Dimensionless equations

We suppose first that all piezoelectric pairs are of identical length, l_p, and introduce the linear density of capacitance c, defined as:

$$c = \frac{\mathcal{C}}{l_p}. \tag{1.31}$$

Equations (1.26)–(1.30) are then written into dimensionless form using L, L/U_∞ and $\rho_f HL$ as characteristic scales of length, time and mass, respectively. We choose $U_\infty\sqrt{\mu c}$ as the characteristic scale for linear density of electric charge (Q_i/l_p), and $U_\infty\sqrt{\mu/c}$ for voltage (V). We naturally obtained three dimensionless parameters M^*, U^* and H^* defined previously. An additional dimensionless parameter, α is found to characterise the piezoelectric coupling:

$$\alpha = \frac{\chi}{\sqrt{Bc}}. \tag{1.32}$$

This parameter measures the intensity of the mutual forcing between the piezoelectric patches and the flapping flag, therefore would command a crucial impact on the energy transfer between the flag and the patches, and consequently on the energy harvesting performance. We also expect that other dimensionless parameters, characterising electrical properties of the system, will be obtained according to the nature of the circuit to be used.

The flag, the piezoelectric patches, and an electric circuit, constitute the coupled system at the core of the present work. The behaviour of this system is therefore described by the following system of dimensionless equations:

$$\frac{\partial^2 \mathbf{x}}{\partial t^2} = \frac{\partial}{\partial s}\left[\mathcal{T}\boldsymbol{\tau} - \frac{\partial}{\partial s}\left(\frac{1}{U^{*2}}\frac{\partial \theta}{\partial s} - \frac{1}{U^*}\sum_1 \alpha V_i F_i\right)\mathbf{n}\right] + M^*\mathbf{F}_{\text{fluid}}, \tag{1.33}$$

$$Q_i = \frac{\alpha}{U^*}\left[\theta\right]_{s_i^-}^{s_i^+} + V_i, \tag{1.34}$$

$$F(V_i, Q_i) = 0. \tag{1.35}$$

And the dimensionless boundary conditions are:

$$\text{at } s = 0 : \quad \mathbf{x} = \theta = 0 \tag{1.36}$$

$$\text{at } s = 1 : \quad T = \frac{1}{U^{*2}}\frac{\partial \theta}{\partial s} - \frac{\alpha}{U^*}V = \frac{1}{U^{*2}}\frac{\partial^2 \theta}{\partial s^2} = 0. \tag{1.37}$$

The above system of equations serves as the root of the following chapters of this work. In addition, two different models will be used to compute the fluid forcing:

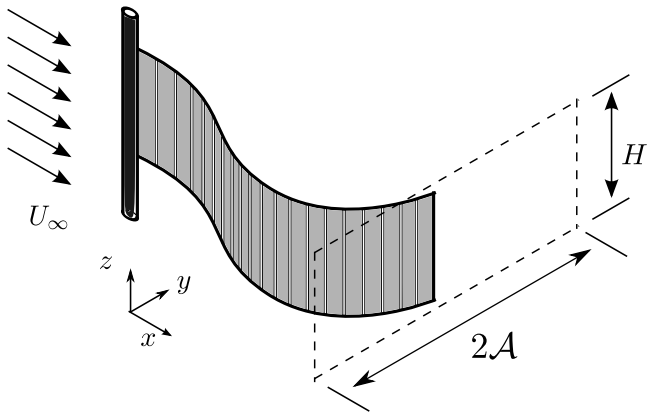

Figure 1.11: Rectangular section defined by amplitude $\mathcal{A}$ and width H.

one model is the LAEBT presented previously of which the expression is given by Eqs. (1.15)–(1.17), and the other model is the vortex sheet model introduced in [Alben 2009a].

In Eqs. (1.33)–(1.34), same notations are used for dimensionless variables $\mathbf{x}$, s, t, V and Q. Throughout this manuscript, no distinction will be made between dimensional and dimensionless variables.

1.6 Energy harvesting

The last important part of the modelling stage is to define the harvested energy. As such definition cannot be based on a specific everyday application (*e.g* a fan, a lamp bulb, or a mobile phone charger...) at the current stage, we will simply consider the most common way of electrical energy consumption: the Joule effect. More precisely, a resistor is placed in the circuit and the dissipation in this resistor is defined as the harvested energy. Although an expression of the harvested power, noted by $\mathcal{P}$ hereinafter, depends on the configuration of a given circuit and therefore is not given at this stage, a definition of the efficiency can already be obtained by choosing a reference. As in other studies on energy harvesting involving flags, we choose the kinetic energy flux of the fluid flow passing through the rectangular section delimited by the flag's width and its peak-to-peak amplitude $2\mathcal{A}$ (Fig. 1.11).

The efficiency η is therefore given by the following expression:

$$\eta = \frac{< \mathcal{P} >}{\frac{1}{2}\rho_f H L U_\infty^3 \times 2 < \mathcal{A} >}, \tag{1.38}$$

where $\mathcal{A}$ is the amplitude of the flag and the operator $<>$ gives the time average of a quantity. By using the quantity $\rho_f L^2 H U_\infty^2$ as the characteristic scale of energy, the efficiency is given in non-dimensional form by:

$$\eta = \frac{< \mathcal{P} >}{< \mathcal{A} >}, \tag{1.39}$$

where $\mathcal{A}$ now denotes the dimensionless amplitude of the flag.

1.7 Energy harvesting using piezoelectric flag connected to resistive circuits

We choose to single out this part as we consider the studies using resistive circuits constitute an important precursor of our work. Some previous works [Dunnmon 2011, Doaré 2011a, Michelin 2013] reported results obtained using a circuit containing only a resistor. The generic relation between electric charge and voltage given by Eq. (1.25), for this particular circuit becomes:

$$V + \mathcal{R}\frac{\partial Q}{\partial t} = 0, \tag{1.40}$$

where $\mathcal{R}$ represents the resistor connected in the circuit.

In [Dunnmon 2011], the authors reported an experimental study using piezoelectric patch based on PZT. They argued that a considerable amount of energy would be harvested using piezoelectric materials if aeroelastic energy harvesters could be carefully designed as to optimise relevant operating parameters.

Such optimisation is reported in [Doaré 2011a, Michelin 2013] where the authors used theoretical and numerical tools to study both a piezoelectric flag's linear stability [Doaré 2011a] and post-critical dynamics [Michelin 2013] when it is connected to resistive circuits. They pointed out that:

- in terms of the linear stability [Doaré 2011a], the resistance stabilises the system when the mass ratio M^* is small, while a destabilising effect of resistance is observed with large M^*, consistent with previously reported results on the destabilisation by damping [Doaré 2010];

- a tuning between the circuit's characteristic time scale and the flapping period leads to a maximal efficiency. Within the range of parameters used in [Michelin 2013], a maximal efficiency of around 10% is achieved with $M^* \sim 20$. The results also suggest that higher efficiency can be expected with even larger M^*.;

- a critical impact on the coupled system's dynamics by the piezoelectric coupling is observed [Doaré 2011a, Michelin 2013]. The authors reported that when the piezoelectric coupling, characterised by α, is strong, both the flapping frequency and amplitude showed modifications, resulting from the damping induced by resistor.

The results in [Doaré 2011a, Michelin 2013] highlight for the first time the important role of piezoelectric coupling in the energy harvesting: the efficiency is found to be scaled as α^2. The authors also found that the choice of electric circuits for energy harvesting might have a critical impact on the system's dynamics and performance, even when the most elementary local resistive circuit is concerned. It

is therefore reasonable and interesting to expect that other kinds of circuits would bring about different impacts to the system, influencing consequently the energy-harvesting efficiency. Studying impacts of different circuits constitutes therefore an important part of the present work.

1.8 Outline of manuscript

The present work will be elaborated in four chapters. Chapters 2–4 will focus on impacts of output circuits on the energy harvesting as well as on the dynamics of the flags. In Chapter 2, we will study a flag totally covered by one pair of piezoelectric patches, and connected to a resistor as well as an inductor, which, combined with the piezoelectric pair's intrinsic capacity, provides an additional natural frequency to the system. We will study, principally by experimental means but also numerically, the resonant property of the system and its impacts on the energy harvesting performance. In Chapter 3, the other case of piezoelectric coverage will be investigated: we will consider that the flag is totally covered by pairs of piezoelectric patches of infinitesimal size. This type of coverage can strengthen the inverse piezoelectric effect on the flag's dynamics, as the additional torque is adapted to the local curvature of the flag. Each piezoelectric pair on the flag is connected to a resistive-inductive circuit. In this chapter, we identify a strong coupling phenomenon between the piezoelectric flag and the circuit and the energy-harvesting performance is considerably improved compared with results reported in [Michelin 2013]. In Chapter 4, instead of connecting each piezoelectric pair to separated circuits, we will use an electric network that interlinks these piezoelectric pairs. The impacts on the energy harvesting as well as the flag's dynamics of the electric network will be studied in this chapter. In Chapter 5, we will turn to the coupled flutter of two flags, and the way it impacts the energy harvesting performance.

Chapter 2

Single Piezoelectric Coverage

In this chapter, a flag covered by one single pair of piezoelectric patches will be studied. As a natural continuation of previous works on purely resistive circuits [Dunnmon 2011, Doaré 2011a, Michelin 2013], a different circuit will be used. This new circuit contains two components: a resistor, which is indispensable for modelling the energy harvesting, and an inductor, which introduces resonant properties to the circuit. We will mainly focus on experimental studies. Numerical studies will also be carried out to complement the experimental results. In addition, a simple current source model will be used to conjecture whether piezoelectric effects apply an impact on the flapping dynamics.

2.1 Experimental set-up

Our experiments are conducted using two prototypes of piezoelectric flag made of two different piezoelectric materials: Polyvinylidene Difluoride (PVDF) and Macro-Fibre Composite (MFC). To fabricate these prototypes, two piezoelectric patches, of identical size, are glued face-to-face and connected with reversed polarity, forming therefore a flag covered by one single piezoelectric pair.

Experiments with these two flags are performed in a same wind tunnel, hereinafter referred to as Tunnel A, whose test section is 10 cm's wide and 4 cm's high [Doaré 2011c] (Fig. 2.1*a*). The maximal flow velocity that Tunnel A could reach is around $U_\infty = 50$ m/s. The wind tunnel's shape therefore prescribes the limits of our prototypes' dimension, as well as the way they are placed in the wind tunnel. PVDF being a paper-like, soft and easily sizeable polymer, the flag based on this material is made to be 9.5 cm's long and 2.5 cm's wide so that it can be placed in Tunnel A in the way shown in Fig. 2.1*a*. This positioning of flag minimises the influence of the flag's weight on its flapping motion as the gravity acts in the span-wise direction, which is perpendicular to the transverse direction. MFC, however, is a prefabricated patch which cannot be reshaped. As the patch's dimension is 9.3 cm×8.9 cm, prohibiting a similar positioning as the PVDF flag, it has to be placed horizontally in Tunnel A (Fig. 2.1*b*). With this positioning, the gravity acts in the transverse direction, which is the same direction as the flag's flapping motion. It is therefore necessary to evaluate the importance of the gravity's influence on the flag's dynamics. One can compare the order of magnitude of the gravity-induced torque on the flag, with that of the elastic torque of the flag:

$$\varepsilon = \mathcal{O}\left(\frac{\text{gravity-induced torque}}{\text{elastic torque}}\right) = \mathcal{O}\left(\frac{mgL^2}{EHh^3}\right). \tag{2.1}$$

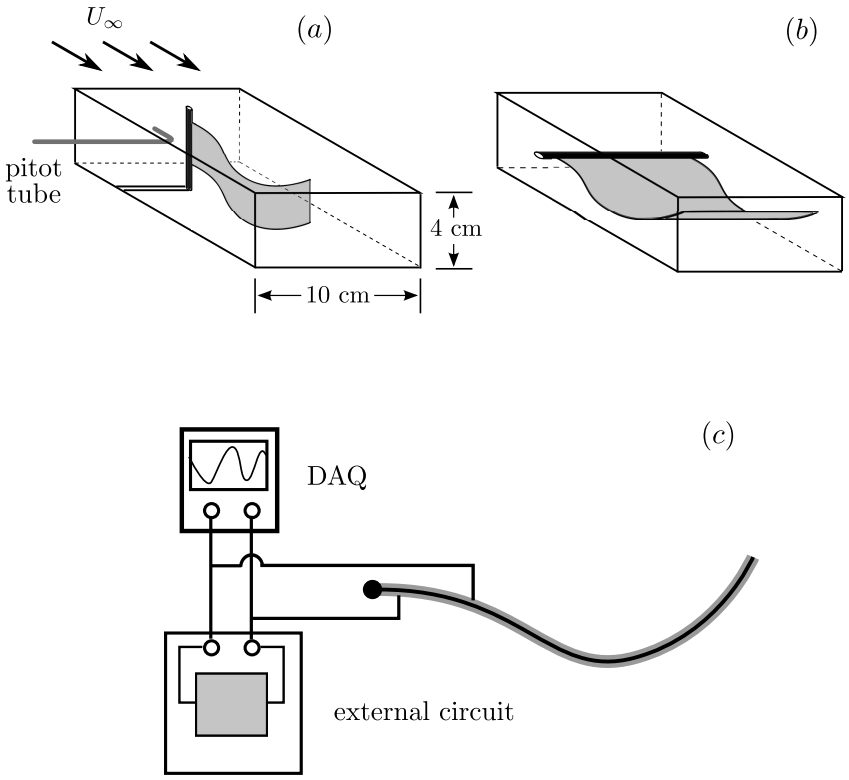

Figure 2.1: Experimental setup: (a) a PVDF piezoelectric flag and (b) a MFC piezoelectric flag in Tunnel A. Both flags are connected with an external circuit and measurement device (c).

	Length	Width	Thickness	Mass	Young's Modulus
PVDF	9.5 cm	2.5 cm	40 μm	5.5×10^{-4} kg	2 GPa
MFC	9.3 cm	8.9 cm	0.4 mm	1.3×10^{-2} kg	20 GPa

Table 2.1: Geometric and mechanical properties of piezoelectric patches.

In Eq. (2.1), m is the mass of one MFC patch, E is the MFC's Young's modulus, and L, H, h are respectively the length, the width and the thickness of the MFC patch. These quantities are shown in Table 2.1. One can obtain that for MFC, $\varepsilon \sim 10^{-2}$. This result shows that compared with the MFC flag's rigidity, the gravity's effect is relatively small and can be neglected. As a result, for any tests performed on the MFC flag positioned as in Fig. 2.1b, one can assume that the gravity is absent. Visually, it is also observed that the MFC flag remains horizontal in its streamwise direction when the flow velocity is 0, which confirms our assumption.

Evidently, for each individual test, only one flag is placed in the wind tunnel. The first series of experiments are performed with the PVDF flag which is clamped to keep a length of 8.5 cm, and the MFC flag. Their respective motion are shown in Fig. 2.2.

The circuit is constructed by connecting an inductor in parallel with a variable

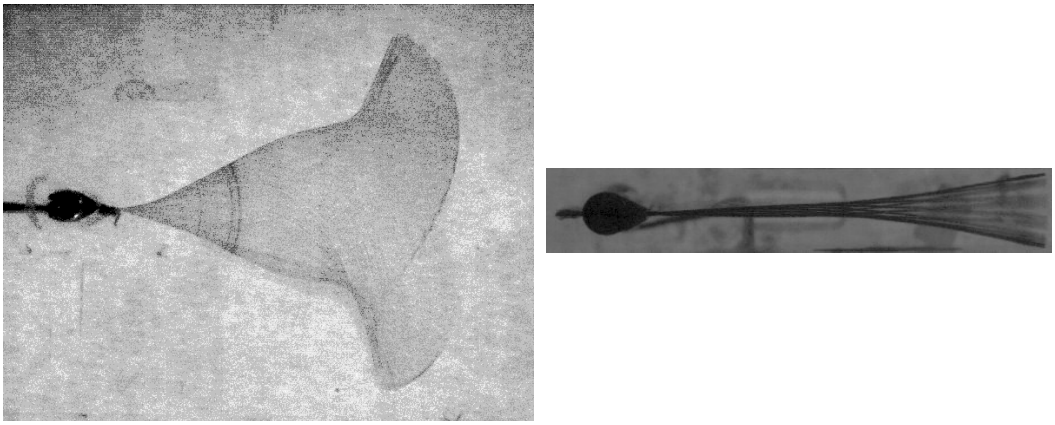

Figure 2.2: Flapping of (left) a PVDF flag and (right) an MFC flag

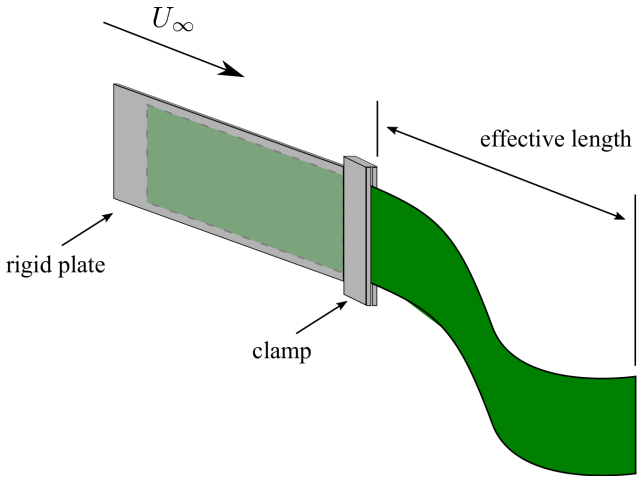

Figure 2.3: "Effective length" of the PVDF flag.

resistor ranging from 5 Ω to 10^8 Ω. This circuit is then connected to the flag, and to a data acquisition board (DAQ) (Fig. 2.1*c*), which records the output voltage V using the software LabView®. Based on V, one may compute the harvested power $\mathcal{P}$:

$$\mathcal{P} = \frac{V^2}{\mathcal{R}}. \tag{2.2}$$

2.2 Comparison between PVDF and MFC

Based on the descriptions in the previous section, one can infer that the MFC flag is more rigid then the PVDF flag, and will consequently wonder whether within the flow velocity range of the wind tunnel, both flags would become unstable and flap.

We start by examining the critical velocity for the PVDF flag of different values of L. As the total length of the PVDF flag is 9.5 cm (Table 2.1), we vary the

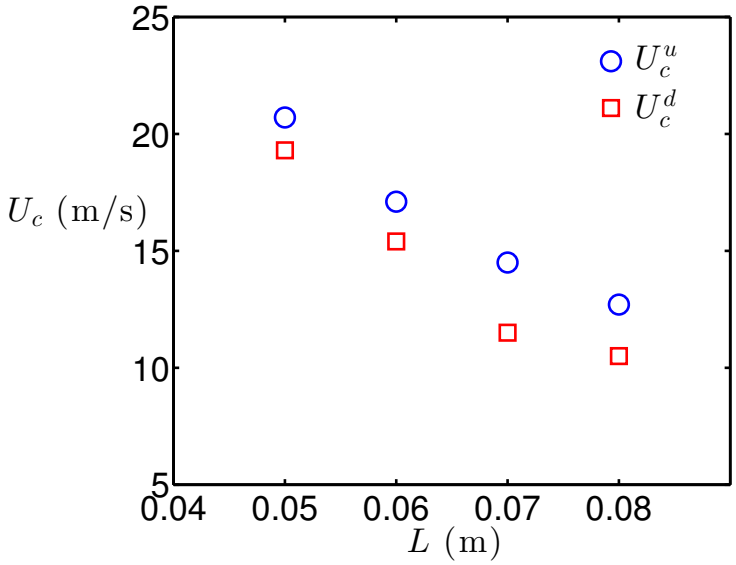

Figure 2.4: Critical instability velocity for the PVDF flag in Tunnel A.

"effective length", i.e. the length of the flag's portion exposed to the fluid flow and is susceptible to flap, by adjusting the position at which the flag is clamped. The other portion of the flag is attached to a rigid plate parallel to the flow so that its influence on the flow would be minimised (Fig. 2.3). For each L, we first increase the flow velocity U_∞ from 0 to a value U_c^u at which the flag starts to flap; then the flow velocity is decreased from U_c^d to another value U_c^u at which the flapping stops. In Fig. 2.4, the values of U_c^u and U_c^d obtained using the PVDF flag are plotted with different L.

We observe first that the critical velocity U_c shown in Fig. 2.4 is consistent with existing work on experimental study in two ways:

- Many works studying the critical velocity have reported a bistability [Alben 2008a, Michelin 2008, Eloy 2008, Eloy 2012, Virot 2013]: the coexistence of flapping and motionless states over a certain range of flow velocity. This phenomenon is also observed in the present experiment using PVDF flag. For every value of L, we observe the existence of bistability over a flow velocity range, of which the lower boundary is always U_c^d, and the higher boundary is U_c^u.

- For a given value of width H, longer flags become unstable at a lower velocity. This observation is consistent with experimental results reported in previous work [Yamaguchi 2000b, Yamaguchi 2000a, Eloy 2007, Virot 2013].

Moreover, the measurement of critical velocity of the PVDF flag shows that the flag becomes unstable at reasonable flow velocities, well below the Tunnel A's limitation. We can therefore expect to perform tests using the PVDF flag with a large range of U_∞ and L.

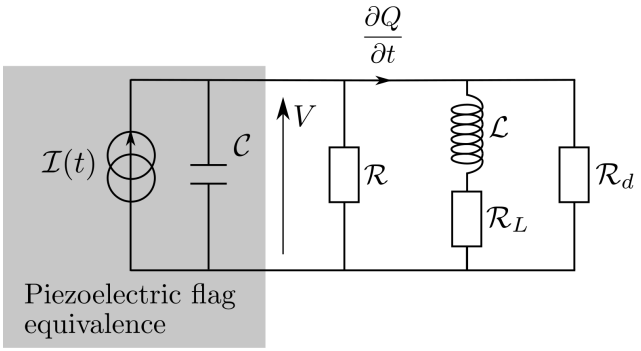

Figure 2.5: Equivalent circuit of experimental set-up.

The MFC flag is however more difficult to be set in motion. As MFC is a composite based on PZT, a piezoelectric ceramic, it inherits the rigidity of PZT. A considerably large flow velocity is mandatory to destabilise the flag. To accelerate the flow in Tunnel A beyond its limitation, the wind tunnel's cross section has to be further reduced, leaving a height of only 2.5 cm, which limits significantly the flag's flapping amplitude. Using the MFC flag of the dimension indicated in Table 2.1, The measurement gives $U_c^u = 57.6$ m/s, a value close to the maximal velocity that Tunnel A is capable of achieving even under further confinement, and $U_c^d = 49.5$ m/s, indicating the existence of the bistability. The results of critical velocity of MFC flag exclude the idea of reducing further its "effective length", which would surely lead to another critical velocity that is prohibitively large for Tunnel A.

From the above comparison, one may conclude that the PVDF flag offers a wider manoeuvrability for experimental study: within the limitation of experimental devices, we can perform tests over a larger range of U_∞ and L, while with the MFC flag, only one value of L and a very small range of U_∞ are available. For this reason, this chapter will mainly focus on studying the PVDF flag, using both experimental and numerical means. Some experimental results obtained using MFC flag will only be briefly presented at the chapter's end.

2.3 Modelling of a flag covered by one piezoelectric pair

2.3.1 Simple current source model neglecting piezoelectric feedback

The system composed of the flag, the resistive-inductive circuit, and the DAQ can be described using the equivalent circuit shown in Fig. 2.5. According to Fig. 2.5, the equivalent circuit consists of an electric current source in parallel connection with an inductor of inductance $\mathcal{L}$, a resistor of resistance $\mathcal{R}$, and a capacitor $\mathcal{C}$ which comes from the intrinsic capacitance of piezoelectric patches. For the sake of consistency in notation, in the following text, we will use $\mathcal{C} = cL$, where c is the linear density of capacitance, as introduced in Chapter 1, and L is the effective length of the flag,

as shown in Fig. 2.3. This equivalent circuit also takes into account the internal resistance of the inductor $\mathcal{R}_L$, which is connected in series with the inductance, and that of the DAQ, $\mathcal{R}_d$, which is in parallel connection with other elements.

From the voltage signal as shown in Fig. 2.6, we can assume that the current source's output takes a harmonic form:

$$\mathcal{I}(t) = \mathcal{I}_0 \mathrm{e}^{\mathrm{j}\omega t}, \tag{2.3}$$

where $\omega = 2\pi f$ with f being the flapping frequency. The amplitude $\mathcal{I}_0$ depends on the conversion factor χ and the flag's leading edge angle while flapping. Using this model, we can compute analytically the dissipation rate in $\mathcal{R}$, i.e. the harvested power $\mathcal{P}$:

$$\mathcal{P} = \mathcal{I}_R \mathcal{I}_R^* \mathcal{R}, \tag{2.4}$$

where $\mathcal{I}_R$ represents the current passing through $\mathcal{R}$, given by:

$$\mathcal{I}_R = \frac{\mathrm{j}\omega \mathcal{I}_0 \mathrm{e}^{\mathrm{j}\omega t}}{1 + \dfrac{\mathcal{R}}{\mathrm{j}\mathcal{L}\omega + \mathcal{R}_L} + \dfrac{\mathcal{R}}{\mathcal{R}_d} + \mathrm{j}\omega \mathcal{C}\mathcal{R}}, \tag{2.5}$$

and $\mathcal{I}_R^*$ is its complex conjugate.

While this model does not replace the nonlinear numerical simulation, we use it as a mean of conjecturing whether an inverse effect is applied on the flag's dynamics, as no such effect is included in this model. In the upcoming experimental study, the prediction obtained from this model, referred as **Simple Current Source Model** hereinafter, will be compared against experimental results. The conjecture is based on the fact that flag's dynamics would remain unaltered under weak inverse piezoelectric effect, therefore good agreement would be found between experimental data and Eq. (2.4), whether or not the system is at resonance. If the inverse piezoelectric effect is strong and that the dynamics of the flag is impacted, the Simple Current Source Model would no more agree with experiments. In the Simple Current Source Model, we choose a constant amplitude by supposing that a permanent flapping regime is reached, and that the coupling is weak enough so that the flag's dynamics is not influenced by the inverse piezoelectric effect. Theoretically, this amplitude depends on both the angle of the trailing edge and the mechanical/electrical conversion factor χ. In our work, $\mathcal{I}_0$ is determined using a purely resistive circuit: first, experiments are performed using a purely resistive circuit with varying $\mathcal{R}$, and then $\mathcal{I}_0$ is chosen as the value which allows the Simple Current Source Model, also using a resistive circuit, to show a good agreement with experimental data.

2.3.2 Nonlinear numerical model

As the flag is covered by one single pair of piezoelectric patches, the expressions of piezoelectric effects, derived from Eqs. (1.18) and (1.22) are written as:

$$Q = \chi\theta(s = L) + clV, \tag{2.6}$$

$$\mathcal{M}_{\text{piezo}} = -\chi V. \tag{2.7}$$

Equation (2.6) indicates that with a flag totally covered by one single piezoelectric pair, the critical variable relating to the electric charge displacement is the angle of the flag's trailing edge.

We need to find the relation between Q and V to close our modelling. For the circuit presented in Fig. 2.5, this relation is written as follows:

$$V + Z \cdot \frac{\partial Q}{\partial t} = 0, \tag{2.8}$$

where Z is the operator of impedance corresponding to the resistor, inductor and the internal resistance of the DAQ in parallel connection. This operator is given as:

$$Z = \frac{1}{\dfrac{1}{\mathcal{R}} + \dfrac{1}{\mathcal{L}\frac{\partial}{\partial t} + \mathcal{R}_L} + \dfrac{1}{\mathcal{R}_d}}. \tag{2.9}$$

In Eq. (2.8), we replace Z by Eq. (2.9), and Q by Eq. (2.6) to obtain the following relation describing the circuit's behaviour under the forcing of the piezoelectric flag:

$$\mathcal{R}_e\mathcal{L}cL\frac{\partial^2 V}{\partial t^2} + \left(\mathcal{R}_e\mathcal{R}_L cL + \mathcal{L}\right)\frac{\partial V}{\partial t} + \left(\mathcal{R}_e + \mathcal{R}_L\right)V + \chi\mathcal{R}_e\mathcal{L}\frac{\partial^2\theta}{\partial t^2} + \chi\mathcal{R}_e\mathcal{R}_L\frac{\partial\theta}{\partial t} = 0, \tag{2.10}$$

where $\mathcal{R}_e$ is the equivalent resistance of $\mathcal{R}$ and $\mathcal{R}_d$ in parallel connection:

$$\mathcal{R}_e = \frac{\mathcal{R}\mathcal{R}_d}{\mathcal{R} + \mathcal{R}_d}. \tag{2.11}$$

Using the same characteristic scales introduced in Chapter 1, the non-dimensional form of Eqs. (2.6)–(2.10) is written as follows:

$$Q = \frac{\alpha}{U^*}\theta(s=1) + v, \tag{2.12}$$

$$\mathcal{M}_{\text{piezo}} = -\frac{\alpha}{U^*}V, \tag{2.13}$$

$$\frac{\partial^2 V}{\partial t^2} + \left(\beta_L\omega_0^2 + \frac{1}{\beta_e}\right)\frac{\partial V}{\partial t} + \left(1 + \frac{\beta_{\mathcal{L}}}{\beta_e}\right)\omega_0^2 V + \frac{\alpha}{U^*}\frac{\partial^2\theta}{\partial t^2} + \frac{\alpha}{U^*}\beta_L\omega_0^2\frac{\partial\theta}{\partial t} = 0. \tag{2.14}$$

Two new dimensionless parameters, β and ω_0, appear in the above equations. Their definitions are given below:

$$\beta = c\mathcal{R}U_\infty, \quad \omega_0 = \frac{1}{U_\infty}\sqrt{\frac{L}{\mathcal{L}c}} \tag{2.15}$$

The parameter β characterises the rate of dissipation in a given resistor, therefore, while β represents the harvesting resistor, the internal resistance of inductor $\mathcal{R}_L$ and DAQ R_d are represented by β_L and β_d, respectively. β_e represents the equivalent resistance given by Eq. (2.11). The parameter ω_0 is the dimensionless natural frequency of the circuit.

Equations (2.12)–(2.14) are then incorporated into the system of equations (1.33)–(1.34) to establish the system to be solved for the numerical study.

2.4 Characterisation of the coupling coefficient α

As defined by Eq. (1.32) in Chapter 1, the coupling coefficient α is determined by three quantities: the conversion factor χ, the bending rigidity B, and the capacitance per unit length c. Among these quantities, c can be measured directly. We first measure $\mathcal{C}$ using a multimeter, which gives $\mathcal{C} = 14$ nF. This measured $\mathcal{C}$ is then divided by the effective length of the flag to obtain c. Note that since the whole PVDF flag, i.e. both the clamped part and the effective part (Fig. 2.3), is connected in the circuit, the total intrinsic capacitance $\mathcal{C}$ is the same regardless of the value of the effective length L. As a result, the linear density of capacitance c based on $c = \mathcal{C}/L$ depends on the effective length L: larger effective length L leads to lower c.

Some other measurements are required to determine B and χ. In this section, we will simply outline the methodology employed to determine each quantity. More experimental details are to be found in Appendix A.

2.4.1 Measurement of B

As the flag is considered as a three-layer sandwich plate, whose width is H, its bending rigidity B could be computed using a dedicated formula [Lee 1989]:

$$B = \frac{E_0 h_0^3 H}{12(1-\nu_0^2)} + \frac{2E_p h_p H}{1-\nu_p^2}\left(\frac{h_0^2}{4} + \frac{h_0 h_p}{2} + \frac{h_p^2}{3}\right), \tag{2.16}$$

where E are ν are respectively the Young's modulus and the Poisson's coefficient of corresponding material, h is the thickness of a layer. The subscripts 0 and p indicate the middle layer and the piezoelectric layers of the flag. However, the middle layer of the flag is a double-sided bonding tape, of which the Young's modulus E_0 and thickness h_0 are difficult to ascertain. It is therefore more practical to measure the flag's free vibration frequency f_0, which, at the first vibration mode, is given by [Timoshenko 1953]

$$f_0 = \frac{3.515}{2\pi L^2}\sqrt{\frac{B}{\mu}}, \tag{2.17}$$

where μ is the flag's mass per unit streamwise length. The bending rigidity is therefore computed from Eq. (2.17).

2.4.2 Measurement of χ

The conversion factor χ is formally given by:

$$\chi = \frac{e_{31}(h_p + h_0)H}{2}, \tag{2.18}$$

where e_{31} is a piezoelectric coefficient. Again, h_0 is difficult to measure due to the nature of the middle layer made of double-sided bounding tape. Our method consists therefore of exploiting the direct piezoelectric effect given by Eq. (2.6). We

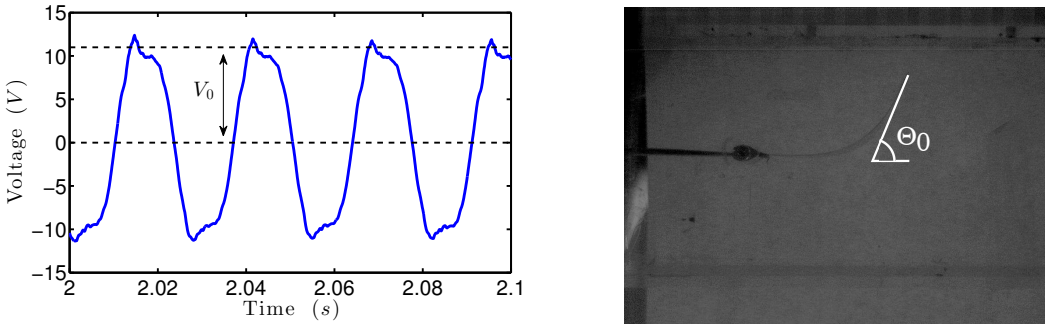

Figure 2.6: Examples of measurement of (left) voltage and (right) angle for $L = 8$ cm and $U = 11.3$ m/s.

connect the flag only to the DAQ, equivalent to a resistance of $R_\mathbf{d} = 10^6\ \Omega$. The electric charge displacement Q can be obtained from Ohm's law:

$$\frac{\partial Q}{\partial t} + \frac{V}{R_d} = 0. \tag{2.19}$$

Replacing Q in Eq. (2.6) by Eq. (2.19), we obtain:

$$\chi \frac{\partial \theta}{\partial t}\bigg|_{s=L} + \mathcal{C}\frac{\partial V}{\partial t} + \frac{V}{R_d} = 0. \tag{2.20}$$

By considering that $V = V_0 \mathrm{e}^{\mathrm{j}\omega t}$ and $\theta = \Theta_0 \mathrm{e}^{\mathrm{j}\omega t}$, the previous equation can be rewritten as:

$$\chi = \frac{V_0}{\omega \Theta_0}\sqrt{\frac{1}{R_d^2} + \omega^2 \mathcal{C}^2}, \tag{2.21}$$

with $\omega = 2\pi f$.

It is therefore necessary to measure the flapping frequency f and the amplitude of the flag's trailing edge orientation Θ_0. The flapping frequency is equal to the frequency of voltage signal, which is recorded by DAQ. Another quantity to be measured is the amplitude of trailing edge orientation Θ_0. As Tunnel A is fabricated using plexiglass, it is transparent so that we could film the motion of the flapping flag using a high-speed camera (Phantom® v9). Among all frames in the recorded film, we choose the frames where the flag exhibits a maximal trailing-edge angle, and measure this angle using ImageJ®. Examples of measurements are shown in Fig. 2.6.

In our experiment, we obtained $B = 1.178 \times 10^{-5}$ N·m^2 and $\chi = 1.45 \times 10^{-7}$ C. These measurements allow us to conclude that for the PVDF flag used in the experimental study, we have $\alpha \sim 0.085$ for $L = 6$ cm, and $\alpha \sim 0.1$ for $L = 8$ cm (see Appendix A). These values are to be kept also for the later numerical study.

2.5 Experimental and numerical results

In this section, we will first present experimental and numerical results obtained with PVDF flag. By having the flag and the circuit working at resonance, our goal is to identify the effect of such resonance on the energy harvesting. In order to achieve this objective, we need to construct a circuit, as shown in Fig. 2.5, that is able to resonate with the PVDF flag flapping at a certain frequency. Next, experimental results obtained using the MFC flag will be presented. An indication of a feedback coupling is observed using the MFC flag.

2.5.1 PVDF flag in Tunnel A

We first perform experiments in Tunnel A with the flag being connected solely to the DAQ in order to obtain the flags' flapping frequency f at a certain flow velocity. This frequency f is then chosen as the required natural frequency of the resonant circuit. With the flag's capacitance $\mathcal{C}$, we can determine, from the expression of the circuit's natural frequency, the inductance $\mathcal{L}$ necessary to obtain a resonance:

$$f = \frac{1}{2\pi\sqrt{\mathcal{L}\mathcal{C}}}. \tag{2.22}$$

For the PVDF flag, clamped at a position so that its effective length is $L = 8$ cm, we have chosen a flow velocity of $U_\infty = 12.2$ m/s, and obtained a frequency of 40.8 Hz. The value of inductance leading to resonance is then $\mathcal{L} \sim 1000$ H.

After having determined the inductance necessary for reaching a resonance, we perform tests with different circuits connecting to the PVDF flag: a purely resistive circuit, i.e. a circuit without inductor; a resonant circuit with an inductor of $L = 600$ H and $\mathcal{R}_L = 3000\Omega$, and a second resonant circuit with $L = 1000$ H, allowing the resonance, and $\mathcal{R}_L = 2000\Omega$. These choices of parameters will, on one hand, allow the comparison between the cases with and without inductance, and on the other hand, with varying inductance, highlights effects that would appear with the resonance. For all three tests, the flow velocity is kept to be $U_\infty = 12.2$ m/s. We vary the value of the harvesting resistance $\mathcal{R}$, record the voltage signal for each value of $\mathcal{R}$, and calculate the time average of harvested power $\mathcal{P}$. The average harvested power as function of $\mathcal{R}$ for all three cases is presented in Fig. 2.7. Results obtained with Simple Current Source Model are plotted in the same figure for comparison.

From Fig. 2.7, we observe that when the inductive-resistive circuit is in resonance with the flapping flag, the harvested power increases considerably compared with the purely resistive case and the non-resonant case. In addition, the predictions of Simple Current Source Model are in fairly good agreement with the experimental data, in terms of both the maximal harvested power and the optimal resistance for all three cases. These results suggest that the presence of inductance improves the energy harvesting performance by resonance, and the good agreement implies that the dynamics of the flag is marginally affected, which is also reflected by the identical flapping frequencies recorded in all three tests (Fig. 2.7*b*).

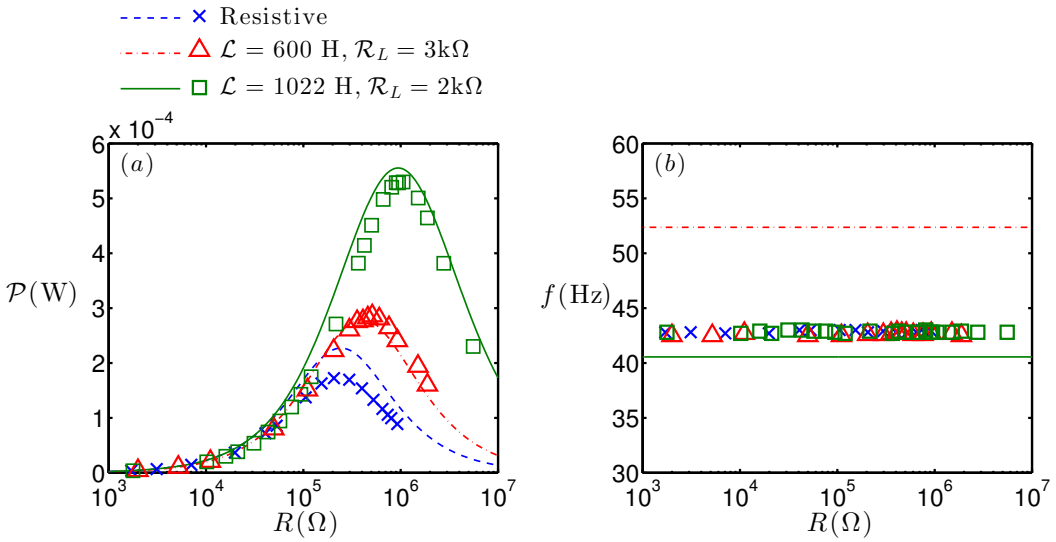

Figure 2.7: (a) Harvested power and and (b) flapping frequencies using PVDF flag of $L = 8$ cm, $H = 2.5$ cm and $U_\infty = 12.2$ m/s. In (a, b), experimental results are plotted with markers. In (a), Simple Current Source Model predictions are plotted with curves. In (b), the curves represent the natural frequency of the corresponding circuit used for Simple Current Source Model.

We attempt now to compare the experimental results with numerical ones obtained using the full nonlinear simulation. The experimental configuration, i.e. a flag of $L = 8$ cm, $H = 2.5$ cm, and a flow velocity of $U_\infty = 12.2$ m/s, corresponds to $M^* = 0.547$, $H^* = 0.3125$, and $U^* = 14.5$ for the nonlinear numerical simulation. By running the simulation using these parameters with $\alpha = 0$, we soon identified a large discrepancy: the experimental flapping frequency, $f = 41$ Hz, is $\omega = 1.9$ when converted to its dimensionless form, while numerical simulation gives $\omega = 1.014$. Another discrepancy lies in the flapping amplitude Θ_0. Experimentally, we observed $\Theta_0 = 82° = 1.43$ rad, which is significantly larger than the numerical result: $\Theta_0 = 0.43$ rad. Despite the discrepancies, we still performed the simulation with $\alpha = 0.1$ to finish the comparison. However, instead of choosing $\omega_0 = 1.9$, matching the circuit's natural frequency in the experiment, we set $\omega_0 = 1.014$ for numerical simulation as to bring forward the effects of resonance. We plot in Fig. 2.8 the harvested power, still noted as $\mathcal{P}$ but rendered dimensionless using the characteristic quantity $\rho_f LHU_\infty^3$, as a function of β, the dimensionless harvesting resistance. In Fig. 2.8, a large discrepancy is observed between two results, with the nonlinear numerical simulation significantly underestimating the harvested power, even at resonance. The key factor responsible for the discrepancies should be the confinement of Tunnel A, whose width is of the same order of magnitude of the flag's length. It has been observed that the confinement may result to an increased added mass of fluid [Belanger 1995]. The large fluid added mass strengthens the fluid forcing,

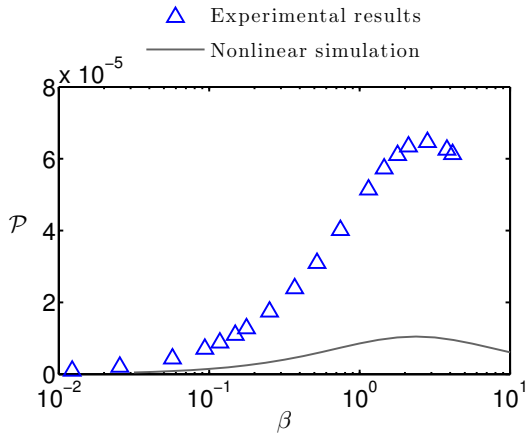

Figure 2.8: Dimensionless harvested power $\mathcal{P}$ as function of β, obtained both experimentally using Tunnel A, and numerically using nonlinear simulation. Experimental parameters are $L = 8$ cm, $U_\infty = 12.2$ m/s, and $f = 41$ Hz, numerical parameters are $M^* = 0.547$, $H^* = 0.3125$, $U^* = 14.5$, and $\omega_0 = 1.014$.

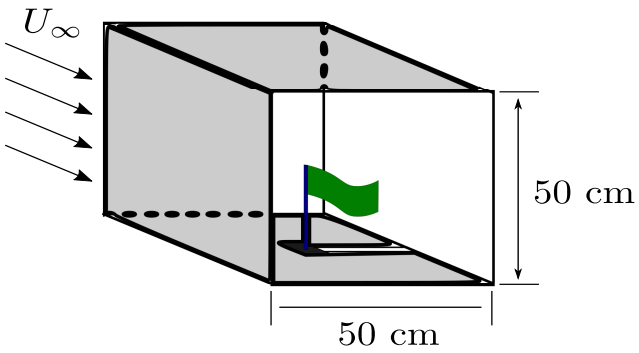

Figure 2.9: PVDF piezoelectric flag placed in the Tunnel B. The three walls in gray are opaque, and the only wall in white is transparent.

and consequently leads to a higher flapping amplitude, as well as a higher harvested energy.

2.5.2 PVDF flag in Tunnel B

The effect of confinement can be confirmed by performing experiments in a more spacious wind tunnel, referred as Tunnel B in the following (Fig. 2.9). Tunnel B has a cross section of 50 cm × 50 cm, much larger than Tunnel A, and a less significant confinement effect is expected.

In order to asses the effect of confinement, we first measure both the flapping frequency ω and amplitude Θ_0 for a flag in Tunnel B. However, the drawback of Tunnel B is the opaque walls of its test section (Fig. 2.9, gray walls) so that a direct filming in the transverse direction is impossible. Therefore, while the frequency ω can still be measured directly using the DAQ, a slightly more convoluted method

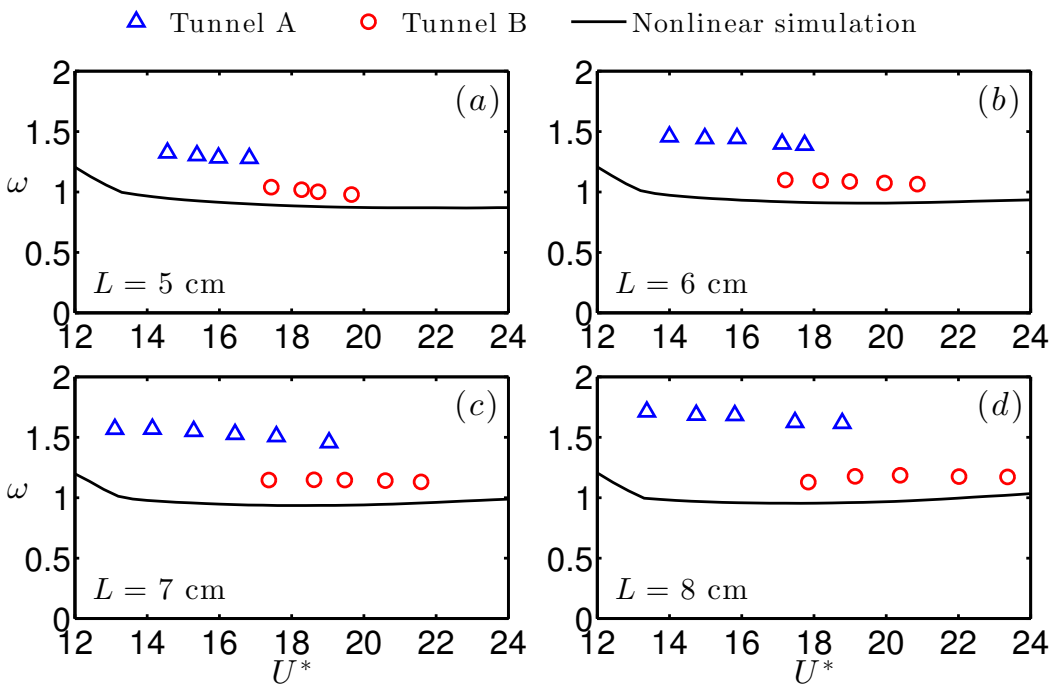

Figure 2.10: Dimensionless flapping frequency ω measured in Tunnel A and Tunnel B, compared with the frequency obtained by nonlinear numerical simulation as a function of U^*. In (a) L=5 cm ($M^* = 0.342$, $H^* = 0.5$), (b) L=6 cm ($M^* = 0.410$, $H^* = 0.417$), (c) L=7 cm ($M^* = 0.479$, $H^* = 0.357$), (d) L=8 cm ($M^* = 0.547$, $H^* = 0.313$).

based on Eq. (2.21) is used to measure the flapping amplitude Θ_0. Having determined χ for the PVDF flag, Eq. (2.21) could be rewritten into the following form and be used to compute Θ_0 from measurable quantities V_0 and ω:

$$\Theta_0 = \frac{V_0}{\omega\chi}\sqrt{\frac{1}{R_{\mathbf{d}}^2} + \omega^2\mathcal{C}^2}, \tag{2.23}$$

We first perform tests with a piezoelectric flag connected solely to DAQ. For the measurement of ω, four values of L are used: L=5 cm, L=6 cm, L=7 cm, and L=8 cm. For each L, the flag's flapping frequency with varying U_∞ in both Tunnel A and Tunnel B are measured and plotted in Fig. 2.10. The results obtained using nonlinear simulation with varying U^* are plotted in the same figure as to compare with the experimental results.

In Fig. 2.10, we can clearly identify a significant effect of confinement: in Tunnel B, for each L, we measured different ω compared with results obtained in Tunnel A. This discrepancy is increasingly visible with longer flags. Meanwhile, with the experiments performed in Tunnel B, we also obtained ω close to nonlinear simulation results.

U_∞ (m/s)	20.26	20.79	21.27	21.94	22.45
V_0 (V)	7.46	8.29	8.65	9.27	9.78
f (Hz)	53.86	56.09	57.78	59.68	60.96
ω (rad)	338.44	352.40	363.06	374.99	383.00

Table 2.2: Measurement with PVDF flag of $L = 6$ cm in Tunnel B

U_∞ (m/s)	14.98	15.75	16.61	17.58	18.52	19.48	20.75
V_0 (V)	6.85	7.72	8.59	9.43	10.10	10.59	11.12
f (Hz)	33.67	35.35	37.50	39.68	41.68	43.63	46.35
ω (rad)	211.53	222.13	235.62	249.34	261.91	274.10	291.24

Table 2.3: Measurement with PVDF flag of $L = 8$ cm in Tunnel B

Our measurement of amplitude Θ_0 is performed using L=6 cm, and L=8 cm. Experimentally, we measure V_0 and f for each L. These results are shown in Table 2.2 for $L = 6$ cm and Table 2.3 for $L = 8$ cm.

Using the results shown in these two tables, the values of Θ_0 are computed using Eq. 2.23, and are plotted in Fig. 2.11. The results on Θ_0 obtained using nonlinear simulation for both L are also presented in Fig. 2.11 for comparison. In Fig. 2.11, we observe that for both $L = 6$ cm and $L = 8$ cm, a fairly good agreement is found between experimental results and the nonlinear numerical simulation in terms of Θ_0. With the previously reported results on flapping frequency, this observation corroborates our statement that the discrepancies obtained between experimental results and the nonlinear simulation using Tunnel A are due to the tunnel's confinement effect. With Tunnel B, offering a more spacious test section thus less confinement, the nonlinear simulation and experimental results reach a satisfactory agreement in terms of ω and Θ_0. The next step is to investigate the energy harvesting using Tunnel B.

With Tunnel B, we choose two configurations where the flag and the circuit would function at resonance. The first case corresponds to $L = 6$ cm, $U_\infty = 20.9$ m/s, leading to a flapping frequency of $f = 56.8$ Hz that matches the natural frequency of a circuit with an inductor of $\mathcal{L} = 530$ H. In the second case, we have $L = 8$ cm, $U_\infty = 17.82$ m/s, yielding $f = 41$ Hz matching the natural frequency of a circuit with an inductor of $\mathcal{L} = 1000$ H. For each configuration, the same protocol as with Tunnel A is used: we vary the harvesting resistance $\mathcal{R}$ and record voltage signal V for each value of $\mathcal{R}$. The harvested power $\mathcal{P}$ is computed based on V and $\mathcal{R}$, and rendered dimensionless using $\rho_f LHU_\infty^3$. Nonlinear simulations are also carried out using parameters corresponding to each configuration: for the first one ($L = 6$ cm), we have $\alpha = 0.085$, $M^* = 0.410$, $H^* = 0.417$, $U^* = 17.91$ and $\omega_0 = 1.06$, while for the second one ($L = 8$ cm), we have $\alpha = 0.1$, $M^* = 0.547$, $H^* = 0.313$, $U^* = 21.18$, and $\omega_0 = 1.14$. The simulation is performed with varying β, in accordance with varying $\mathcal{R}$ in experiments.

In Fig. 2.12, we plot $\mathcal{P}$ as function of β, obtained both by experiments in Tunnel

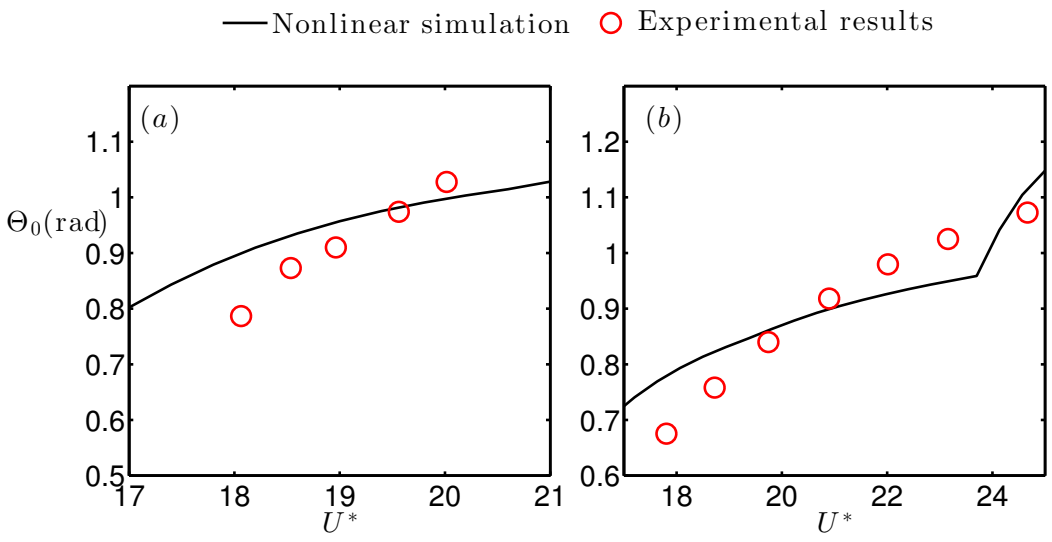

Figure 2.11: Estimation of Θ_0 in experiments and nonlinear numerical simulation results in Tunnel B, for (a) $L = 6$ ($M^* = 0.410$, $H^* = 0.417$) cm and (b) $L = 8$ cm ($M^* = 0.547$, $H^* = 0.313$).

B and by the nonlinear simulation. A fairly good agreement is found between results obtained using Tunnel B and the numerical simulation. This observation confirms that the confinement of Tunnel A indeed leads to a larger flapping amplitude Θ_0, and subsequently increases the harvested energy. This agreement also validates the numerical code for further numerical study. The slight discrepancy can be explained by the difference observed between the estimation of Θ_0 by nonlinear numerical simulations and the experimental results (Fig. 2.11).

2.5.3 MFC flag and feedback of piezoelectric effect

As mentioned earlier, we will only briefly present results obtained with MFC flag as the material's rigidity hinders experimental study with large range of parameters. Here, we will also exclude nonlinear simulations with MFC flag for the following reasons. On one hand, the results with PVDF flag in Tunnel A have already shown the strong effect of confinement which is not taken into account by the nonlinear numerical model. Knowing that the MFC flag requires additional confinement in Tunnel A in order to accelerate the flow, the experimental conditions would only become more complicated for the nonlinear model. On the other hand, the MFC flag presents an aspect ratio of $H^* \sim 1$ (c.f. Table 2.1), making it not sufficiently slender for a nonlinear simulation based on a slender body model. Despite these limitations, our persistence in studying the MFC flag is motivated by its potentially stronger piezoelectric effects.

This potential can be evinced by an estimation of α associated with the MFC

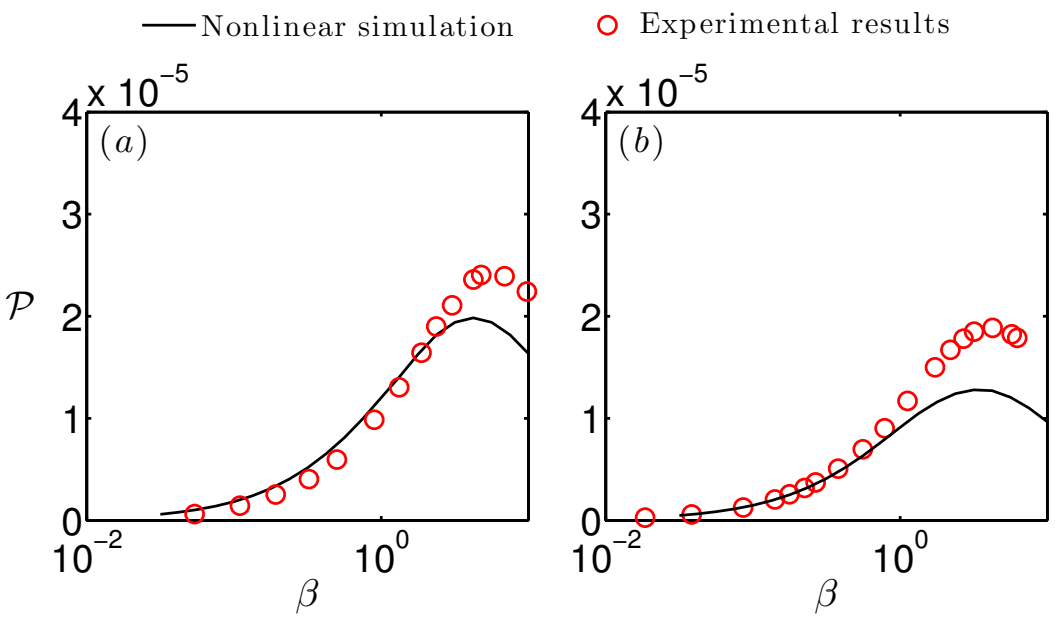

Figure 2.12: Dimensionless harvested power $\mathcal{P}$ obtained both from experiments and nonlinear numerical simulations as function of β. In (a): $\alpha = 0.085$, $L = 6$ cm, $f = 56.8$ Hz, $U_\infty = 20.9$ m/s, $\mathcal{L} = 530$ H and $\mathcal{R}_L = 1000\Omega$ and in (b): $\alpha = 0.1$, $L = 8$ cm, $f = 41.1$ Hz, $U_\infty = 17.82$ m/s, $\mathcal{L} = 1000$ H and $\mathcal{R}_L = 2000\Omega$

flag using Eq. 1.32. However, with MFC, except c, which is directly measured to be $c = 13.35$ μF/m, we can only roughly estimate B and χ for two reasons:

- The MFC being too rigid, its free vibration cannot last for even one measurable period. So measuring its free vibration frequency is impossible. As a result, B is calculated using the materials Young's modulus $E = 20$ GPa, and its geometry, given in Table 2.1, by neglecting the middle layer's thickness. The results is $B = 0.01$ N·m^2
- As the MFC flag's length is difficult to adjust, and that the operative velocity range is small, we have only used one value of U_∞ to measure Θ_0, V_0 and ω for computing χ using Eq. (2.18).

With $U_\infty = 52.04$ m/s and $L = 9$ cm. Our measurement gives: $V_0 = 8.02$ V, $\Theta_0 = 0.20$ rad, and $\omega = 569.26$. From these results, we obtain $\chi = 4.87 \times 10^{-5}$ C, leading to $\alpha = 0.15$, a value implying a stronger piezoelectric coupling than the PVDF flag.

Our next step is to perform tests with the MFC flag connected to a resonant circuit. Except being placed differently in Tunnel A, the MFC flag involves a similar experimental protocol as the PVDF flag. Using the flag connected solely to the DAQ, the flag's flapping frequency, therefore the required natural frequency of the circuit, is found to be $f = 86.51$ Hz at a flow velocity of $U = 52.04$ m/s, reaching the limitation of Tunnel A. From Eq. (2.22), we obtain that a resonance would be achieved using an inductor of $L \sim 3$ H.

We plot in Fig. 2.13*a* the harvested power $\mathcal{P}$ as function of $\mathcal{R}$ obtained both using experiments and the Simple Current Source Model. In Fig. 2.13*b*, flapping frequencies are plotted in comparison with the natural frequency for each circuit used in Simple Current Source Model. For the MFC flag, we can first identify the effects of resonance, similar to the case with the PVDF flag: at resonance, the harvested power increases considerably and a good agreement is found between the experimental data and the prediction of Simple Current Source Model (Fig. 2.7*a*). The flapping frequency, seen from Fig. 2.7*b*, is seemingly insensitive to the circuit's frequency.

We may however notice that with the MFC flag, a discrepancy exists between the prediction and experimental data for the case where $\mathcal{L} = 2.09$ H and $\mathcal{R}_L = 261$ Ω (Fig. 2.13*a*). The Simple Current Source Model predicts much lower harvested power than experimental results. The natural frequency of the corresponding circuit is distant from the resonant value $f \sim 86.51$ Hz (Fig. 2.13*b*). The difference between these two cases lies therefore primarily in the internal resistance of inductor $\mathcal{R}_L$, which dissipates electrical energy and therefore adds damping in a resonant system. With identical inductance, an inductor with lower $\mathcal{R}_L$ possesses a lower damping. A stronger effect of inductance can therefore be observed. This strong inductive effect leads to a high voltage, and consequently enhances the direct piezoelectric effect and acts in favour of the energy harvesting. Moreover, the fact that the Simple Current Source Model fails to predict the experimental results may also

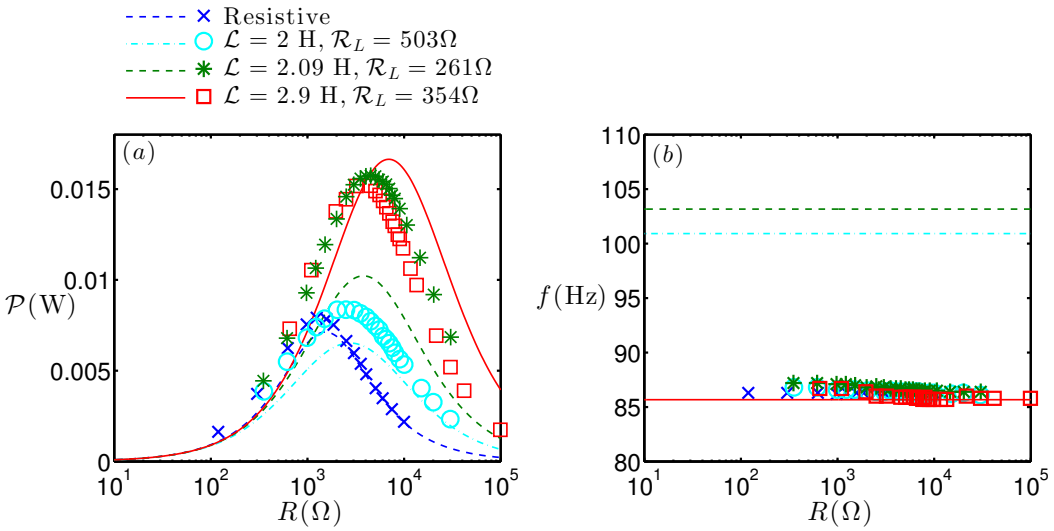

Figure 2.13: (a) Harvested power and (b) flapping frequencies using MFC flag with $U_\infty = 52.04$ m/s and $L = 9$ cm. In (a, b), experimental results are plotted using markers. In (a), Simple Current Source Model predictions are plotted with curves. In (b), the curves represent the natural frequency of the corresponding circuit used for the Simple Current Source Model.

imply the existence of a feedback due to the inverse piezoelectric effect. When the coupling is strong enough, and when the circuit's damping is sufficiently reduced, this feedback introduces variations to the dynamical properties of the piezoelectric flag and enhances the energy harvesting. These variations are not taken into account by the Simple Current Source Model used here.

In order to further asses the potential feedback, we are interested in the frequency of the voltage signal, which is identical to the flapping frequency ω, an indicator of the flag's flapping dynamics. A comparison will be made between the frequencies obtained with and without an inductor in the circuit. In order to maximise the possibility of observing a feedback, the harvesting resistor $\mathcal{R}$ is removed from the circuit so that the circuit's damping is minimised. Both the PVDF flag and the MFC flag are used for this comparison. For each flag, placed in a given flow velocity, the voltage signal is recorded with and without the inductor in the circuit. The frequencies of the voltage signal in both cases (with inductor/without inductor) are then computed and compared with each other in order to identify any possible difference, a sign of an existing feedback. For the MFC flag, the flow velocity is set as $U_\infty = 56.4$ m/s, leading to a flapping frequency of $f = 90.61$ Hz without inductor. For the PVDF flag of length $L = 6$ cm, we use $U_\infty = 21.3$ m/s and the resulting frequency is $f = 57.8$ Hz without inductor. The inductor to be used for the MFC flag is $\mathcal{L} = 2.09$ H and $\mathcal{R}_L = 261\ \Omega$, and for the PVDF flag, we have $\mathcal{L} = 530$ H and $\mathcal{R}_L = 1000\ \Omega$.

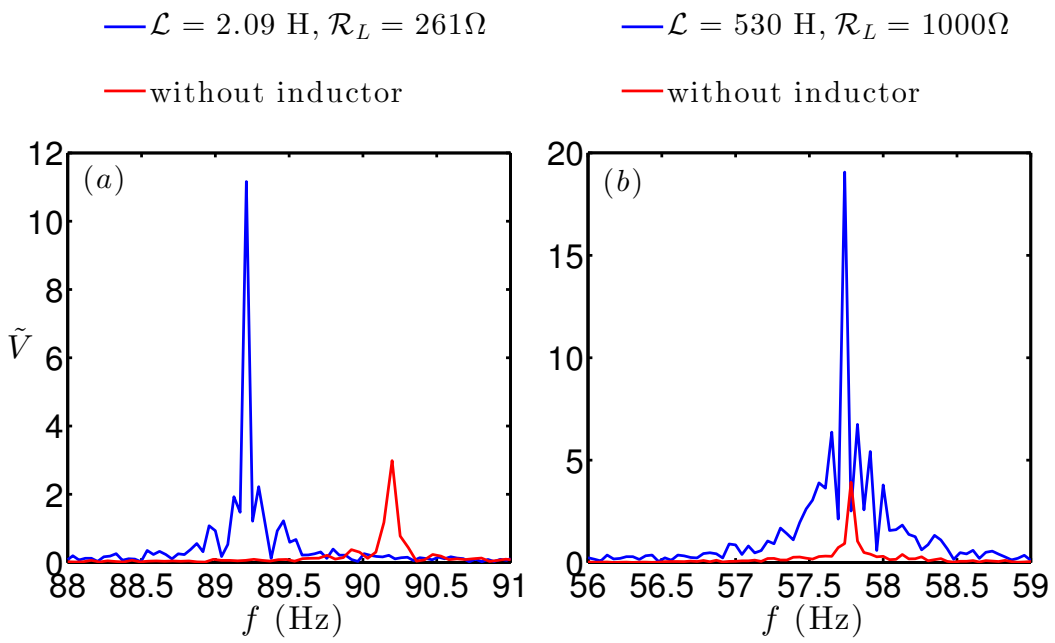

Figure 2.14: Spectra of electrical voltage $\tilde{V}$ for (a) the MFC flag at $U_\infty = 56.4$ m/s, in Tunnel A and (b) the PVDF flag of $L = 6$ cm at $U_\infty = 21.3$ m/s, in Tunnel B. For both flags, no harvesting resistor is connected in the circuit.

The spectra of the voltage signal $\tilde{V}$ are plotted in Fig. 2.14 for both flags. We can clearly observe that in the case of MFC flag, the peak of the spectrum obtained with inductor is separated from that of the spectrum obtained with open circuit (Fig. 2.14a), while with the PVDF flag, the peaks of both spectra are centred at the same frequency (Fig. 2.14b). This observation clearly shows that the feedback will certainly appear when the coupling is strong and the circuit's damping is low (small $\mathcal{R}_L$).

Due to the limitations of our experimental devices, such as the insufficient flow velocity and the small wind tunnel, our experimental investigation of the feedback effect stops here. Further experimental study with materials such as MFC requires larger scale devices, as we can see that with current experimental conditions, the MFC flag starts to flap only at a very large velocity ($U_\infty \sim 50$ m/s). With larger wind tunnels, we would be able to fabricate a prototype with MFC larger than the present one both in width and length. A flag with this larger dimension is expected to become unstable at a much lower flow velocity.

2.6 Summary and conclusion

In this chapter, we studied experimentally the energy harvesting using a piezoelectric flag connected to a resonant circuit. We indeed observed the beneficial effect

brought by the resonant circuit to the energy harvesting: an increased harvested power. The nonlinear numerical model also showed a fairly good agreement with the experimental study, highlighting in the meantime the important confinement effect. Experimental studies with a more potent piezoelectric material have shown promising signs of a potential feedback effect from the circuit to the dynamics of the flag.

Indeed, to reach the resonance, large inductance is needed for such low frequency applications. However, it is not prohibitively colossal and such inductors are still commercially available, showing optimistic perspective of the technology on the electrical aspect. The critical problem lies still in the aspects concerning the piezoelectric materials. Composite materials seem to be a good option for future development of piezoelectric flags, as they are more flexible than ceramics, and are capable of offering a stronger coupling than polymers.

The Simple Current Source Model, neglecting the feedback effect, presented in this chapter is proved to be a valid model to estimate energy-harvesting performance when the piezoelectric coupling is weak. Its validity is however challenged when the coupling becomes strong, inducing a feedback, in which case it is mandatory to incorporate the inverse piezoelectric effect into the modelling. As to study the full piezoelectric coupling, i.e. incorporating both the direct and inverse piezoelectric effects, the nonlinear model used in this chapter, considering the inverse piezoelectric effect as an added torque on the flag, is a good candidate whose validity is proved for weak piezoelectric coupling (PVDF flag, $\alpha \sim 0.1$) by the estimations of the flapping amplitude and the harvested power, which are in good agreement with experimental results. We will extend this model to stronger piezoelectric coupling, as already done in several works using purely resistive circuits [Doaré 2011a, Michelin 2013, Piñeirua 2015], in the following chapters using resonant circuits.

The experimental studies presented in this chapter clearly identify the resonance as a key mechanism that improves the performance of energy-harvesting piezoelectric flags. When the flag is at resonance with the harvesting circuit, at least twice as much as energy is harvested than using a circuit without resonant properties (e.g. purely resistive circuits). This conclusion, i.e. resonance improves energy harvesting, should also be applied to other kinds of vibration energy harvesters. One path to improve their performance is to couple the vibration source (e.g. the flag in the present work) with a resonant oscillator (e.g. the circuit in the present work). Moreover, the potential feedback from the resonant oscillator to the vibration source would also be an effect acting in favour of the energy harvesting. In the next chapter, we will focus on investigating this potential feedback effect.

Chapter 3

Fluid-solid-electric lock-in

In this chapter, a numerical study is conducted to investigate a flag covered by an infinite number of piezoelectric pairs. To each pair, a resistive-inductive circuit is connected.

This configuration enhances the piezoelectric coupling by the fact that more than one piezoelectric pairs cover the flag. As a result, the piezoelectric effects are expected to be adapted to the local curvature of the flag, thereby introducing a stronger feedback coupling. This chapter will focus on the role of this feedback coupling and the impacts thereof on the energy harvesting.

Modifications on the modelling of piezoelectric effects will be elaborated in the next section. Some results will then be presented in terms of linear stability, nonlinear dynamics, and finally the energy harvesting performance. A discussion on the importance of the coupling factor α will also be presented at the end of this chapter.

3.1 Modelling of a flag continuously covered by pairs of piezoelectric patches

The flag is covered by more than one piezoelectric pairs, as shown in Fig. 3.1*a*. To each pair, a resistive-inductive circuit is connected (Fig. 3.1*b*).

To simplify the problem, we assume that each pair has the same length and that each circuit has identical resistance and inductance. Further assumptions consist of considering the flag's surface to be fully and continuously covered by piezoelectric pairs ($s_+^i = s_-^{i+1}$), and the streamwise length of each pair l_p to be infinitesimal compared with the flag's length ($l_p \ll L$). These assumptions imply that the system's electric state can be characterised by the linear density of quantities such as Q, V, $\mathcal{G}$, $\mathcal{C}$, and $\mathcal{L}$, which are defined as: $q = Q/l_p$, $v = V$, $g = \mathcal{G}/l_p$, $c = \mathcal{C}/l_p$, $l = \mathcal{L}l_p$. Note that in this chapter, the resistors are characterised by their conductance $\mathcal{G}$, instead of their resistance $\mathcal{R}$. The quantities q and v are therefore continuous functions of the Lagrangian coordinate s. The expressions of piezoelectric effects, derived from Eqs. (1.18) and (1.22) are written as:

$$q = \chi \frac{\partial \theta}{\partial s} + cv, \tag{3.1}$$

$$\mathcal{M}_{\text{piezo}} = -\chi v. \tag{3.2}$$

It is useful to note that the derivative term in Eq. (3.1) is a result of the previously

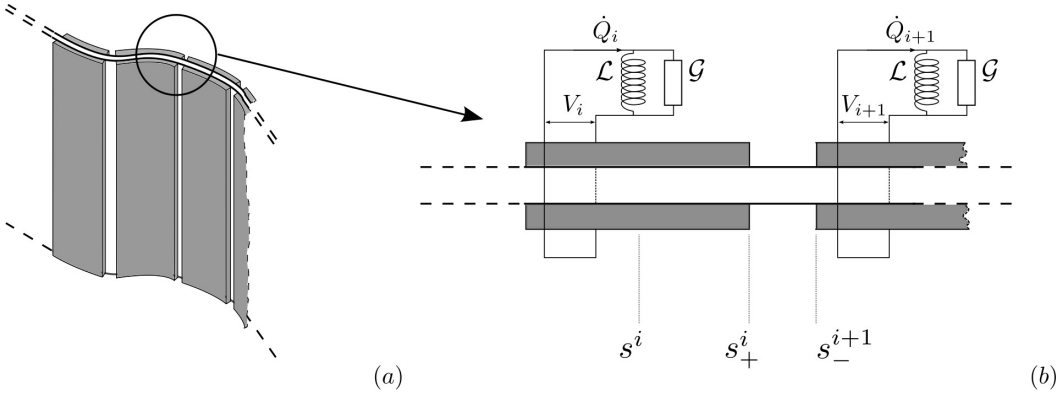

Figure 3.1: In (a): a flag covered by pairs of piezoelectric patches and in (b): piezoelectric pairs connected to resistive-inductive circuits, inductors and resistors are in parallel connection

mentioned assumptions:

$$\frac{\partial \theta}{\partial s} = \lim_{l \to 0} \frac{[\theta]_{s_i^-}^{s_i^+}}{l} \tag{3.3}$$

The fact that the voltage v is a continuous function of s brings a modification in the boundary condition at trailing edge $s = L$, representing physically the cancellation of the shear force. We recall here that this condition is written in its most generic form as:

$$\text{at} \quad s = L : \quad \frac{\partial \mathcal{M}}{\partial s} = 0, \tag{3.4}$$

where the bending moment $\mathcal{M}$, in the case of continuous coverage by small piezoelectric pairs, is given as:

$$\mathcal{M} = B\frac{\partial \theta}{\partial s} - \chi v. \tag{3.5}$$

Then the boundary condition on the shear force is written as:

$$\text{at} \quad s = L : \quad \frac{\partial \mathcal{M}}{\partial s} = B\frac{\partial^2 \theta}{\partial s^2} - \chi \frac{\partial v}{\partial s} = 0. \tag{3.6}$$

Note that with one single piezoelectric pair, the voltage induces simply a local added torque at $s = L$, which does not contribute to the shear force.

The last part of modelling is to find the equivalent circuit, which is similar to that in Chapter 2, albeit that all quantities are replaced by their linear density in this chapter (Fig. 3.2). The relation linking q and v based on this equivalent circuit is given by the following equation:

$$v + gl\frac{\partial v}{\partial t} + l\frac{\partial^2 q}{\partial t^2} = 0 \tag{3.7}$$

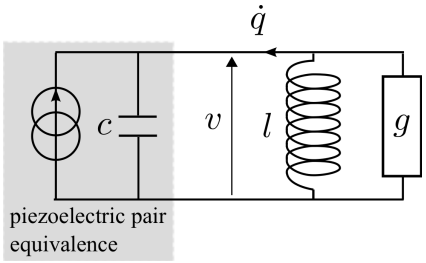

Figure 3.2: Equivalent circuit of a infinitesimally small piezoelectric pair connected to a resistive-inductive loop, in the limit of continuous distribution

The dimensionless form of Eqs. (3.1)–(3.2), using the same characteristic scales as in previous chapters, are obtained as follows:

$$q = \frac{\alpha}{U^*}\frac{\partial \theta}{\partial s} + v, \tag{3.8}$$

$$\mathcal{M}_{\text{piezo}} = -\frac{\alpha}{U^*}v, \tag{3.9}$$

and the dimensionless form of Eq. (3.7) is:

$$\beta\omega_0^2 v + \frac{\partial v}{\partial t} + \beta\frac{\partial^2 q}{\partial t^2} = 0, \tag{3.10}$$

where the two parameters β and ω_0 are defined as:

$$\beta = \frac{cU_\infty}{gL}, \quad \omega_0 = \frac{L}{U_\infty\sqrt{lc}}. \tag{3.11}$$

Note that β and ω_0 hold similar definitions as in Chapter 2, except that in Eq. (3.11) they are based on linear density of $\mathcal{G}$, $\mathcal{C}$, and $\mathcal{L}$.

The complete set of dimensionless equations to be solved for this configuration is written as follows:

$$\frac{\partial^2 \mathbf{x}}{\partial t^2} = \frac{\partial}{\partial s}\left[T\boldsymbol{\tau} - \frac{\partial}{\partial s}\left(\frac{1}{U^{*2}}\frac{\partial \theta}{\partial s} - \frac{1}{U^*}\alpha v\right)\mathbf{n}\right] + M^*\mathbf{F}_{\text{fluid}}, \tag{3.12}$$

$$\mathbf{F}_{\text{fluid}} = -m_a H^*\left[\frac{\partial U_n}{\partial t} - \frac{\partial U_n U_\tau}{\partial s} + \frac{1}{2}U_n^2\frac{\partial \theta}{\partial s}\right]\mathbf{n} - \frac{1}{2}C_d|U_n|U_n\mathbf{n}, \tag{3.13}$$

$$\beta\omega_0^2 v + \frac{\partial v}{\partial t} + \beta\frac{\partial^2 v}{\partial t^2} + \frac{\alpha\beta}{U^*}\frac{\partial^3 \theta}{\partial t^2 \partial s} = 0, \tag{3.14}$$

with the following boundary conditions:

$$\text{at } s = 0: \quad \mathbf{x} = \theta = 0 \tag{3.15}$$

$$\text{at } s = 1: \quad T = \frac{1}{U^{*2}}\frac{\partial \theta}{\partial s} - \frac{\alpha}{U^*}v = \frac{1}{U^{*2}}\frac{\partial^2 \theta}{\partial s^2} - \frac{\alpha}{U^*}\frac{\partial v}{\partial s} = 0. \tag{3.16}$$

The harvested energy in this case is defined as the sum of rate of dissipation in all resistors. The dimensionless form of this quantity is given by:

$$\mathcal{P} = \int_0^1 \frac{v^2}{\beta}\mathrm{d}s. \tag{3.17}$$

As a reminder, the efficiency is computed using the definition given by Eq. (1.39):

$$\eta = \frac{< \mathcal{P} >}{< \mathcal{A} >}, \tag{3.18}$$

where $\mathcal{A}$ is the dimensionless amplitude of the flag.

3.2 Linear stability

In this section we are interested in the effect of the inductance, measured by ω_0, on the critical velocity U_c^*. The dependence of U_c^* on the mass ratio M^* and the resistance β, in the case of purely resistive circuits, is studied in previous works [Eloy 2007, Doaré 2011a, Michelin 2013].

At the initial stage of instability, we assume small vertical displacement, i.e $y \ll 1$, allowing linearisation of Eqs. (3.12)–(3.14). The resulting linear equations are:

$$(1+M_a)\frac{\partial^2 y}{\partial t^2} + 2M_a\frac{\partial^2 y}{\partial t \partial s} + M_a\frac{\partial^2 y}{\partial s^2} + \frac{1}{U^{*2}}\frac{\partial^4 y}{\partial s^4} - \frac{\alpha}{U^*}\frac{\partial^2 v}{\partial s^2} = 0, \tag{3.19}$$

$$\beta\omega_0^2 v + \frac{\partial v}{\partial t} + \beta\frac{\partial^2 v}{\partial t^2} + \frac{\alpha\beta}{U^*}\frac{\partial^4 y}{\partial t^2 \partial s^2} = 0, \tag{3.20}$$

and the linearised boundary conditions are:

$$\text{at } s=0: \quad y = \frac{\partial y}{\partial s} = 0 \tag{3.21}$$

$$\text{at } s=1: \quad \frac{1}{U^{*2}}\frac{\partial^2 y}{\partial s^2} - \frac{\alpha}{U^*}v = \frac{1}{U^{*2}}\frac{\partial^3 y}{\partial s^3} - \frac{\alpha}{U^*}\frac{\partial v}{\partial s} = 0. \tag{3.22}$$

The coefficient M_a is defined by $M_a = m_a M^* H^*$, representing the added mass of the fluid surrounding the flag. As in the following, we will fix $M^* = 1$ and $H^* = 0.5$, in the linear regime, the fluid forcing on each cross-section of the flag depends only on two parameters: m_a and U^*.

The classical Galerkin decomposition method is used to solve Eqs. (3.19) and (3.20) by assuming that both the vertical displacement y and the streamwise voltage distribution v are linear combination of a set of orthogonal functions. For y, this function set is chosen to be $\phi_i(x)$ which are free vibration eigenmodes of a cantilevered beam without piezoelectric coupling, therefore the second derivative of $\phi_i(x)$ with respect to x, denoted by $\phi_i''(x)$, are chosen for the voltage v in order to satisfy clamped-free boundary conditions given by Eqs. (3.21)–(3.22). Consequently, y and v can be written as:

$$y = \sum_{i=1}^{N} Y_i e^{j\omega t}\phi_i(x), \quad \text{and} \quad v = \sum_{i=1}^{N} V_i e^{j\omega t}\phi_i''(x). \tag{3.23}$$

The expansion given in Eq. (3.23) takes y and v proportional to $e^{j\omega t}$. Therefore, Y_i and V_i are simply complex constant. Following Eq. (3.23). The resulting equations

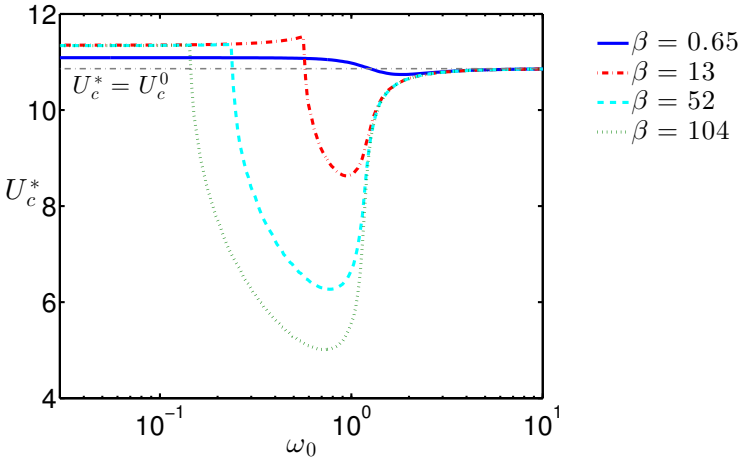

Figure 3.3: Evolution of the critical velocity with ω_0 for four different values of β and $\alpha = 0.3$.

are then projected onto $\phi_i(x)$ and $\phi_i''(x)$. Equations (3.19) and (3.20) are then recast as an eigenvalue problem and the coupled system is unstable if one of its eigenfrequencies has a positive imaginary part.

The evolution with ω_0 is shown on Fig. 3.3. For $\omega_0 \gg 1$, corresponding to the configuration where the circuit's natural frequency is much larger than the flapping frequency, the impedance resulting from the inductance is negligible compared with the resistance, therefore the inductor acts as a short-circuit, and U_c^* converges, regardless of β, to U_c^0, the critical flow velocity without coupling ($\alpha = 0$). For $\omega_0 \ll 1$, the inductance-induced impedance is so large that the electric charge displacement takes place only in the resistor. As a result, we obtain $U_c^* \geqslant U_c^0$, illustrating the stabilising effect of the resistance [Doaré 2011a]. Note that for larger values of M^*, resistance may exhibit a destabilising effect [Doaré 2011a], which is comprised in a more general case of destabilisation by damping [Doaré 2010]. For intermediate values of ω_0 ($0.1 < \omega_0 < 1$), we observe a significant destabilising effect of inductance for intermediate and large values of β. This destabilisation increases with β, as the circuit becomes dominated by inductive effects. For small β, however, no such destabilisation is observed, as the circuit transitions directly from its resistive limit (small ω_0) to its short circuit limit (large ω_0). These results highlight the positive impacts of the circuit's inductive behaviour: the instability threshold may be lowered, resulting in energy harvesting with slower flow velocity.

In order to determine the origin of this destabilisation, it is necessary to probe the evolution of eigenvalues with ω_0. For this purpose, we choose $U^* = 10$ and $\beta = 52$. This value of U^* is lower than U_c^0 but higher than the minimum critical velocity of $\beta = 52$ (see Fig. 3.3), therefore is an appropriate choice to study the origin of the destabilisation. Figure 3.4 shows the evolution of the two most unstable pairs of eigenvalues with ω_0 at $U^* = 10$ and $\beta = 52$. Starting from $\omega_0 \gg 1$ and decreasing ω_0, the electrical circuit evolves successively from short circuit, to RLC

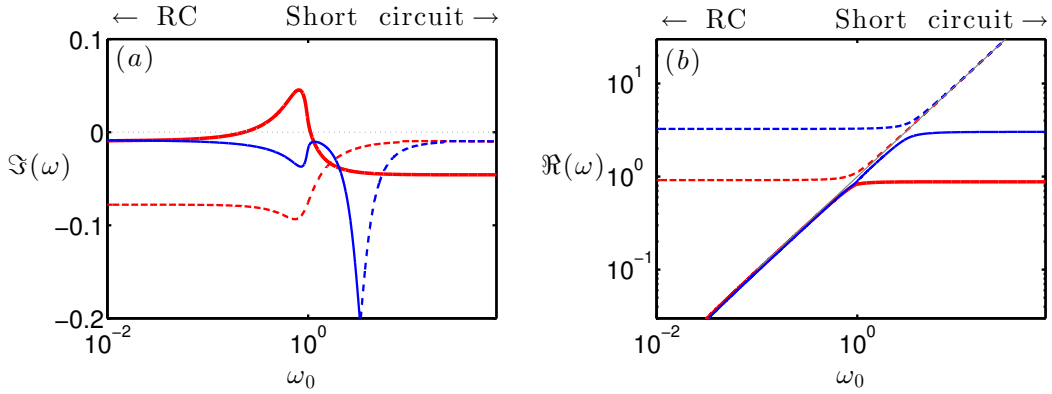

Figure 3.4: Evolution with ω_0 of (a) the imaginary part (growth rate) and (b) the real part (frequency) of the second and third pairs of eigenvalues for $\alpha = 0.3$, $U^* = 10$ and $\beta = 52$. In both (a) and (b), solid lines represent mechanical modes and dashed lines represent electrical modes. The destabilized pair is plotted in blue and the other plotted in red. In (b), $\Re\omega = \omega_0$ is plotted as a reference.

loop, and finally to a purely resistive circuit. Instability occurs when the imaginary part of any mode becomes positive.

In the absence of coupling ($\omega_0 \gg 1$), both pairs each consists of two eigenvalues: one is associated with an electrical mode, with the frequency (real part of the corresponding eigenvalue) equal to ω_0; the other is associated with a mechanical mode, with the frequency independent of ω_0. Decreasing ω_0 leads to interactions between the electrical and mechanical modes, successively within each pair. This interaction destabilises the mechanical mode, leading to the flag's instability at intermediate ω_0 (Fig. 3.4). Note that this interaction within other pairs also leads to an increase of $\Im(\omega_0)$ for the mechanical mode, but does not lead to instability (at least for $M^* = 1$).

3.3 Nonlinear dynamics and energy harvesting

Above the critical velocity, the unstable coupled system experiences an exponential growth in the flag's flapping amplitude, which eventually saturates due to nonlinear effects. A direct integration of the fluid-solid-electric system's nonlinear equations Eqs. (3.12)–(3.14) is performed using an implicit second order time-stepping scheme [Alben 2009a]. The flag is meshed using Chebyshev-Lobatto nodes, and a Chebyshev collocation method is used to compute spatial derivatives and integrals. At each time step, the resulting nonlinear system is solved using Broyden's method [Broyden 1965]. The simulation is started with a perturbation in the flag's orientation ($\theta(s, t = 0) \neq 0$), and is carried out over a sufficiently long time frame so as to reach a permanent regime.

The reduced flow velocity is chosen at $U^* = 13$, a value sufficiently higher than

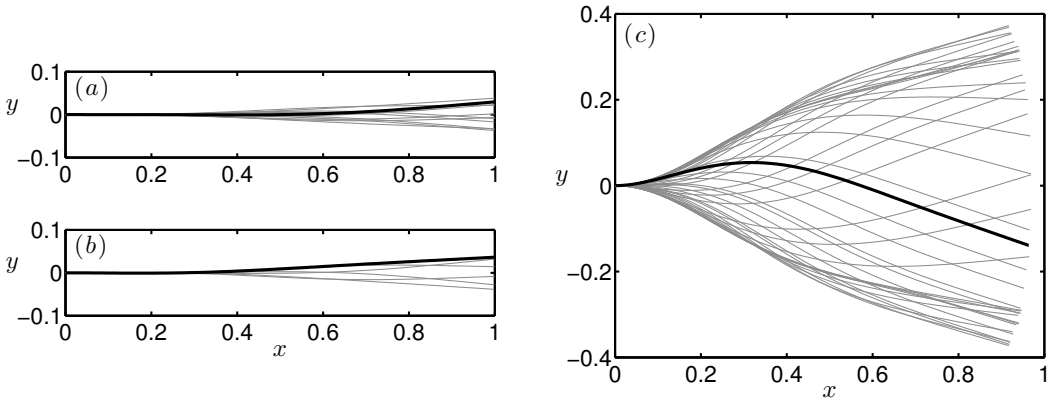

Figure 3.5: Flapping motion of flags at $\alpha = 0.3$, $\beta = 52$, $U^* = 13$ and (a) $\omega = 0.25$ (no lock-in), (b): $\omega_0 = 3.85$ (no lock-in), (c): $\omega_0 = 0.32$ (lock-in).

the critical velocity U_c^*. The flapping motion of the flag is plotted in Fig. 3.5 for three different values of ω_0, and the energy-harvesting efficiency and the flapping frequency as function of ω_0 are plotted in Fig. 3.6.

The flag's behaviour is observed to vary drastically with different ω_0 (Fig. 3.5). When ω_0 is within the range of destabilisation, the flag undergoes a remarkably larger deformation (Fig. 3.5c) than with other values of ω_0 (Fig. 3.5a, b).

Figure 3.6a shows the evolution of the efficiency with ω_0, and demonstrates that this increased flapping amplitude indeed leads to a significant efficiency improvement: a maximum efficiency of 6% is obtained here, significantly higher than the optimised efficiency obtained at $M^* = 1$ and $U^* = 13$ without inductance ($\sim 0.1\%$) [Michelin 2013].

Within the high efficiency range, the flapping frequency is deviated and locks onto the natural frequency of the circuit, ω_0 (Fig. 3.6b). A frequency lock-in is therefore observed here, similar to the classical lock-in observed in Vortex-Induced Vibrations (VIV) [Williamson 2004, Grouthier 2013]: the frequency of an active oscillator (the flag) is dictated by the natural frequency of a coupled passive oscillator (the circuit). The lock-in range is extended by a reduction of the circuit's damping ($1/\beta$), consistently with what is observed in VIV for varying structural damping [King 1973]. The lock-in range leading to high efficiency coincides with the range of ω_0 associated with the destabilisation by inductance (Fig. 3.3). This suggests that a coupled piezoelectric flag, once destabilised by inductive effects, may flap at a frequency close to the natural frequency of the circuit. As a result, a permanent resonance takes place between the flag and the circuit, leading to increased flapping amplitude and harvesting efficiency.

By varying ω_0 within the lock-in range, Fig. 3.6 shows that when the frequency of the output circuit matches the short-circuit natural frequency of the flapping flag ($\omega \sim 1.35$), the maximal efficiency is obtained for every value of β. This observation highlights again the interest of forcing piezoelectric structures at their natural

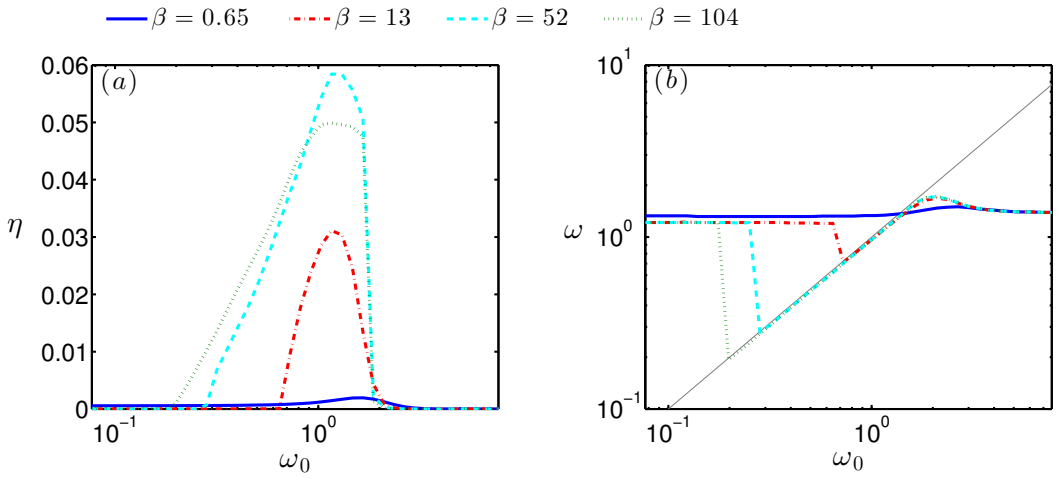

Figure 3.6: (a) Harvesting efficiency η and (b) flapping frequency ω as a function of ω_0 for four different values of β and $\alpha = 0.3$, $U^* = 13$.

frequencies for energy harvesting, as suggested by previous studies, where maximal efficiency is observed when the external forcing resonates with the piezoelectric system [Allen 2001, Roundy 2005, Ng 2005]. The existence of a lock-in extends this effect to a larger range of parameters, by maintaining the circuit working at resonance, hence guaranteeing efficient energy transfers from the flag to the circuit.

In order to illustrate the circuit's resonance, we are interested in the energy transfer within the coupled system in this regime. The mechanical energy balance is straightforward to obtain. By multiplying Eq. (3.12) with the derivative in time of $\mathbf{x}$, we have:

$$\frac{\partial \mathbf{x}}{\partial t} \cdot \frac{\partial^2 \mathbf{x}}{\partial t^2} = \frac{\partial \mathbf{x}}{\partial t} \cdot \frac{\partial}{\partial s} \left[T\boldsymbol{\tau} - \frac{\partial}{\partial s} \left(\frac{1}{U^{*2}} \frac{\partial \theta}{\partial s} - \frac{1}{U^*} \alpha v \right) \mathbf{n} \right] + M^* \frac{\partial \mathbf{x}}{\partial t} \cdot \mathbf{F}_{\text{fluid}}. \tag{3.24}$$

Using the inextensibility condition given by Eq. (1.4), we can arrange Eq. (3.24) into the following form:

$$\frac{1}{2} \frac{\partial}{\partial t} \left[\left(\frac{\partial \mathbf{x}}{\partial t} \right)^2 \right] = -\frac{1}{U^{*2}} \frac{\partial}{\partial t} \left[\left(\frac{\partial \theta}{\partial s} \right)^2 \right] + \frac{\alpha}{U^*} v \frac{\partial^2 \theta}{\partial s \partial t} + M^* \frac{\partial \mathbf{x}}{\partial t} \cdot \mathbf{F}_{\text{fluid}} + \frac{\partial F_{\text{mech}}}{\partial s}. \tag{3.25}$$

The above equation gives the local balance of mechanical energy, where F_{mech} is the mechanical energy flux, given by:

$$F_{\text{mech}} = T\boldsymbol{\tau} \cdot \frac{\partial \mathbf{x}}{\partial t} + \frac{\partial \theta}{\partial t} \left(\frac{1}{U^{*2}} \frac{\partial \theta}{\partial s} - \frac{\alpha}{U^*} v \right) - \frac{\partial \mathbf{x}}{\partial t} \cdot \frac{\partial}{\partial s} \left(\frac{1}{U^{*2}} \frac{\partial \theta}{\partial s} - \frac{\alpha}{U^*} v \right) \mathbf{n}. \tag{3.26}$$

We are now interested in the global form of mechanical energy balance, which is given simply by integrating Eq. (3.25) from 0 to 1. Using the boundary conditions, it is straightforward that:

$$\int_0^1 \frac{\partial F_{\text{mech}}}{\partial s} \mathrm{d}s = 0. \tag{3.27}$$

Therefore, integrating Eq. (3.25) yields:

$$\frac{\partial \mathcal{E}_p}{\partial t} + \frac{\partial \mathcal{E}_k}{\partial t} = \mathcal{W}_f - \mathcal{T}, \tag{3.28}$$

where $\mathcal{E}_p$ and $\mathcal{E}_k$ are respectively the flag's potential and kinetic energy, given in their dimensionless form by:

$$\mathcal{E}_p = \frac{1}{2}\int_0^1 \frac{1}{U^{*2}}\left(\frac{\partial \theta}{\partial s}\right)^2 \mathrm{d}s, \quad \mathcal{E}_k = \frac{1}{2}\int_0^1 \left(\frac{\partial \mathbf{x}}{\partial t}\right)^2 \mathrm{d}s. \tag{3.29}$$

The term $\mathcal{W}_f$ is the rate of work of fluid force, and $\mathcal{T}$ is the rate of energy transfer from the structure to the circuit through piezoelectricity. They are given by:

$$\mathcal{W}_f = M^* \int_0^1 \mathbf{F}_{\text{flluid}} \cdot \frac{\partial \mathbf{x}}{\partial t}\mathrm{d}s, \quad \mathcal{T} = -\frac{\alpha}{U^*}\int_0^1 v\frac{\partial^2 \theta}{\partial t \partial s}\mathrm{d}s. \tag{3.30}$$

Next, we need to find the balance of electrical energy. We first introduce the relation between the voltage applied on an inductor, and the electric charge flowing through it, noted as q_I. In its dimensionless form, this equation reads:

$$v = \frac{1}{\omega_0^2}\frac{\partial^2 q_I}{\partial t^2}. \tag{3.31}$$

In the first term of Eq. (3.14), the variable v is replaced by Eq. (3.31), yielding:

$$\frac{\partial^2 q_I}{\partial t^2} + \frac{1}{\beta}\frac{\partial v}{\partial t} + \frac{\partial^2 v}{\partial t^2} + \frac{\alpha}{U^*}\frac{\partial^3 \theta}{\partial t^2 \partial s} = 0. \tag{3.32}$$

Integrating Eq. (3.32) with respect of t, and multiplying the resulted expression by v yields:

$$\frac{\partial}{\partial t}\left[\frac{1}{2\omega_0^2}\left(\frac{\partial q_I}{\partial t}\right)^2 + \frac{1}{2}\left(\frac{\partial v}{\partial t}\right)^2\right] + \frac{v^2}{\beta} + v\frac{\alpha}{U^*}\frac{\partial^2 \theta}{\partial t \partial s} = 0. \tag{3.33}$$

Equation (3.33) gives the local balance of electrical energy. The global form of electrical energy balance is given also by integrating Eq. (3.33) from 0 to 1, which is:

$$\frac{\partial \mathcal{E}_C}{\partial t} + \frac{\partial \mathcal{E}_I}{\partial t} = -\mathcal{P} + \mathcal{T}, \tag{3.34}$$

where $\mathcal{E}_C$ and $\mathcal{E}_I$ are respectively energy stored in capacitors and inductors, given in their dimensionless form by:

$$\mathcal{E}_C = \frac{1}{2}\int_0^1 v^2 \mathrm{d}s, \quad \mathcal{E}_I = \frac{1}{2\omega_0^2}\int_0^1 \left(\frac{\partial q_I}{\partial t}\right)^2 \mathrm{d}s. \tag{3.35}$$

In the electrical energy balance, one can also find the harvested power $\mathcal{P}$ and the rate of energy transfer $\mathcal{T}$.

We are now interested in the balance of both mechanical energy and electrical energy of the system with and without lock-in. The comparison of both cases are plotted in Fig. 3.7. When the system is not at lock-in and $\omega_0 \ll 1$ (Fig. 3.7*a*),

the dominant balance of the electrical energy conservation takes place between the intrinsic capacitance and the piezoelectric patches, while the inductance and the resistance contribute a negligible part to the energy balance. The role of capacitance in this case is actually equivalent to a small added rigidity, as it stores and releases, throughout the period, electrical energy converted from mechanical energy by piezoelectric patches. When the system is not at lock-in but with $\omega_0 \gg 1$ (Fig. 3.7*c*), the dominant balance of the electrical energy conservation takes place between the inductance in the circuit and the piezoelectric patches, while the intrinsic capacitance and the resistance contribute little to the energy balance. The inductance in this case acts as an added mass and exchanges energy with the flag throughout the period. In these two cases, the piezoelectric effects marginally affect the flag's dynamics, as the mechanical energy balance of the flag is dominated by the fluid forcing (Fig. 3.7*d*, *f*).

When the flapping frequency is locked to the circuit's (Fig. 3.7*b*), the electrical energy balance is dominated by the periodic exchange between the inductance and capacitance, proving that the circuit is working at its resonance regime. A more active role of the circuit is consequently observed also on the dynamic of the flag, as the rate of work of the piezoelectric forcing becomes comparable to that of the fluid forcing (Fig. 3.7*e*). It is however worthwhile to note that the permanent regime represented by this energy balance showing the circuit working at resonance requires a long transient period to be reached. During this period, the capacitor and the inductor are charged, energy therefore accumulates in the electrical circuit, leading to the resonant behaviour consisting of strong energy exchanges between the capacitance and inductive components. This results in

- a large flapping amplitude of the flag forced by the piezoelectric patches, and
- a large amount of dissipation in the resistance .

This lock-in and the increased efficiency are not possible with purely resistive circuit [Michelin 2013], since an essential element of this mechanism is the periodic energy exchange between two forms of electrical energy. We can therefore conclude that the resonant property of a resisitive-inductive circuit may lead to a frequency lock-in phenomenon that significantly enhances the energy-harvesting performance of a piezoelectric flag.

3.4 Impact of the coupling factor

A decisive factor is the intensity of piezoelectric coupling, characterised by α in this work. In practice, the coupling coefficient α, defined in Eq. (1.32), depends primarily on the materials used for the piezoelectric flag, as well as the geometries of the flag and piezoelectric electrodes [Doaré 2011a]. The importance of the coupling factor has been reported by many studies on energy harvesting by piezoelectric systems [Anton 2007, Caliò 2014]. In [Doaré 2011a, Michelin 2013], when the coupling is weak and the amplitude does not depend on α, a dependence of the harvesting

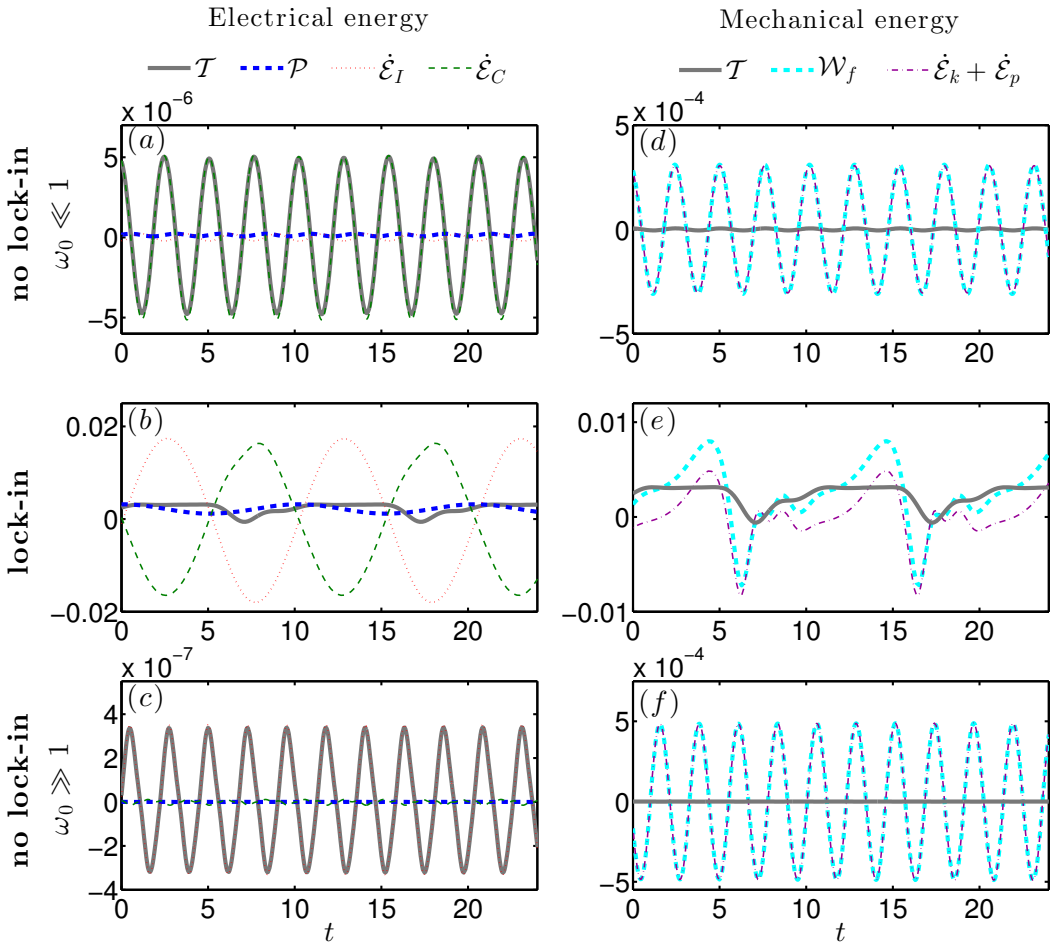

Figure 3.7: (a, b, c) Electrical and (d, e, f) mechanical energy balance for (a, d) $\omega_0 = 0.25$, (b, e) $\omega_0 = 0.32$, (c, f) $\omega_0 = 3.85$, and $\alpha = 0.3$, $U^* = 13$, $\beta = 52$. The operator $\dot{}$ denotes derivatives in time.

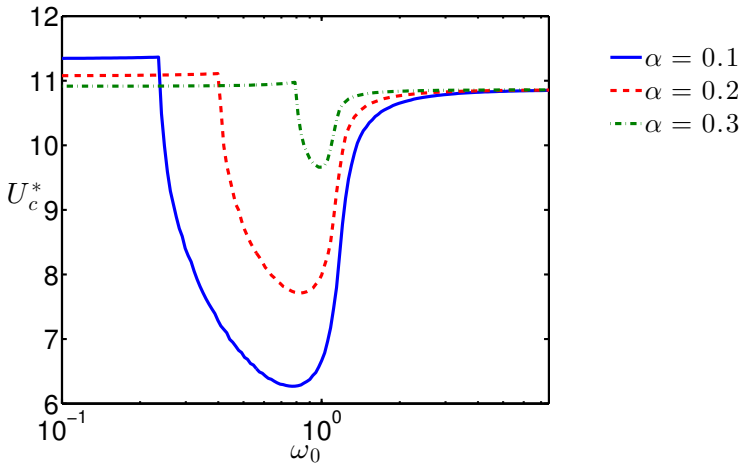

Figure 3.8: Evolution of the critical velocity with ω_0 for different values of α. Other parameters are $\beta = 52$, $M^* = 1$.

efficiency to α^2 was identified. This dependence is expected as from Eq. (3.8), one can infer that the voltage v is proportional to α. And as the harvested power $\mathcal{P}$ is proportional to v^2, it is straightforward that $\mathcal{P} \sim \alpha^2$, hence $\eta \sim \alpha^2$.

In the present work, the influence of α is observed both in terms of critical velocity (Fig. 3.8) and the lock-in range (Fig. 3.9). In Fig. 3.8, lower critical velocities and larger destabilisation range in terms of ω_0 are observed with increasing α. Fig. 3.9 shows that the range of frequency lock-in also increases with increasing α. The impact of the coupling coefficient α on the system's performance is again identified: a strong piezoelectric coupling is desired so that the beneficial effects of a resonant circuit, namely the destabilisation and the frequency lock-in, can be obtained.

It is nonetheless necessary to mention that using available materials, we only have a limited range of possible values of α. For example, the PVDF used in our experimental study presented in the previous chapter may yield $\alpha \sim 0.1$, and as mentioned in [Doaré 2011a], using material with better piezoelectric property, such as PZT, and a steel plate as the flag, one might expect $\alpha \sim 0.3$.

One might also expect improving α by considering materials of small Young's modulus E, therefore the bending rigidity B, which has an impact on α according to Eq. (2.16), would decrease. While we have a limited choice of piezoelectric materials, one might choose softer materials for the flag. However, this idea is not practical. For example, if we choose a flag based on Mylar ($E_0 = 4$ GPa) covered with PZT patches ($E_p = 60$ GPa), the three-layer flag will be extremely heterogeneous. As a result, when the flag flaps, the middle layer made of soft material is not strong enough so that two piezoelectric patches will not be able to exhibit opposite deformation, but identical deformation. As a result, their effect would cancel out each other's, thus no electricity would be generated. Meanwhile, in [Ducarne 2012], the authors included the thickness of the flag h_0 and that of the piezoelectric patches h_p in their study. They found that the optimal value for h_p decreases with decreasing E_0, leading to

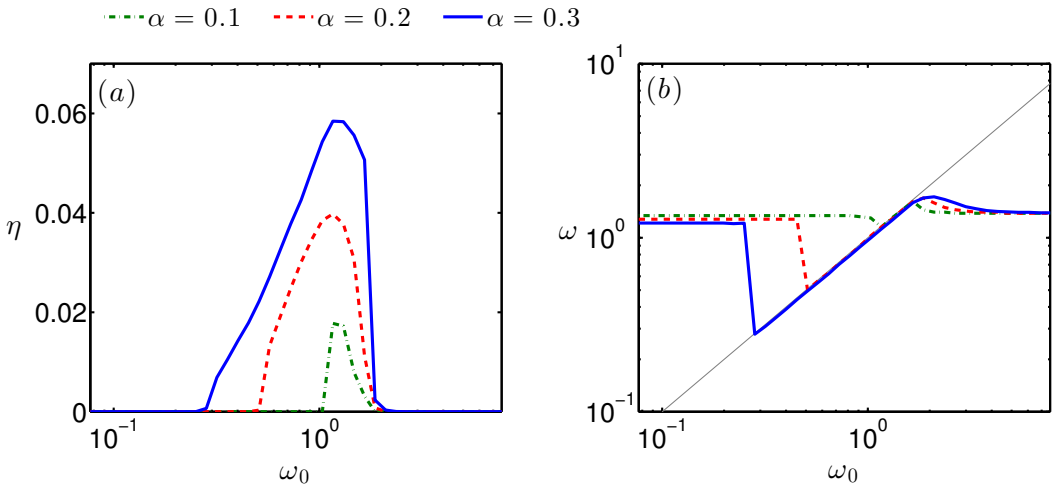

Figure 3.9: (*a*) Harvesting efficiency and (*b*) flapping frequency ω as a function of ω_0 for different values of α. Other parameters are $\beta = 52$, $M^* = 1$, $U^* = 13$, $H^* = 0.5$.

a lower conversion factor χ. As a result, using softer materials for the flag would only marginally improve the coupling.

3.5 Perspective: lock-in with one single piezoelectric pair

One might wonder whether the lock-in phenomenon, observed in this chapter using a continuous coverage of infinitesimal piezoelectric pairs, would be expected with more realistic configurations, such as a flag covered with one piezoelectric pair. In order to exploit this perspective, the configuration studied in Chapter 2 is revisited, using a much stronger piezoelectric coupling, $\alpha = 0.3$, and an ideal inductor which has zero internal resistance. Eq. 2.14 is therefore modified accordingly and is written as:

$$\frac{\partial^2 V}{\partial t^2} + \beta \frac{\partial V}{\partial t} + \omega_0^2 V + \frac{\alpha}{U^*} \frac{\partial^2 \theta}{\partial t^2} = 0. \tag{3.36}$$

Based on Eq. (3.36), together with the beam equation as well as boundary conditions, we use numerical simulations to compute the energy harvesting efficiency as well as the flag's dynamics. The efficiency and the flapping frequency are presented in Fig. 3.10. While the flapping frequency matches the circuit's natural frequency (Fig. 3.10*b*), we indeed observe a peak of η (3.10*a*), a result of resonance.

In terms of flapping motion, we observe that at resonance, the flag flaps with a much larger amplitude (Fig. 3.11*b*) than without resonance (Fig. 3.11*a*). In terms of flapping frequency (Fig. 3.10*b*), we do not observe a lock-in with an extent as large as in the cases presented in Fig. 3.6*b*. However, within a small range of ω_0, the flag's flapping frequency seems to be following the circuit's natural frequency.

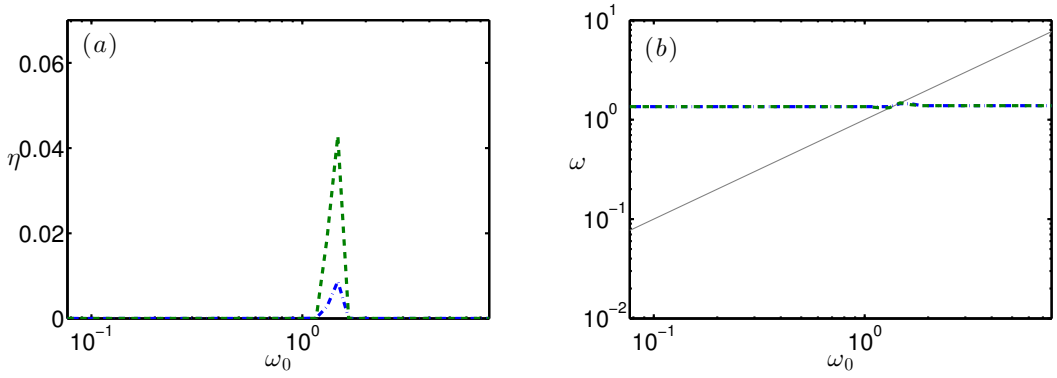

Figure 3.10: (a) Harvesting efficiency η and (b) flapping frequency ω as a function of ω_0 for $\alpha = 0.3$, and $\beta = 13$ (blue, dash-dot), $\beta = 52$ (green, dashed)

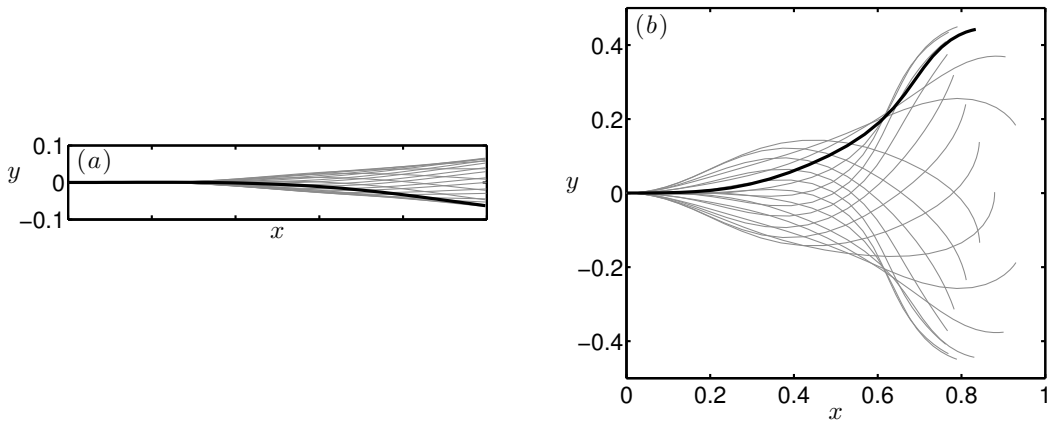

Figure 3.11: Flapping motion of flags at $\alpha = 0.3$, $\beta = 4$ and (a) $\omega_0 = 13.43$ (no lock-in), (b): $\omega_0 = 19.14$ (resonance)

Moreover, the large amplitude observed at resonance (Fig. 3.11*b*) suggests that a strong coupling exists between the flag and the circuit, even if the flag is covered only by one single piezoelectric pair.

A recent study [Piñeirua 2015], using purely resistive circuit but a flag covered by a finite number of piezoelectric pairs, reported that by optimising the positioning and the number of piezoelectric pairs on the flag, one might expect an energy-harvesting performance of the same order as the continuous coverage of infinitesimally small piezoelectric pairs. It is reasonable to expect their results to also apply with resistive-inductive circuits: with a finite number of piezoelectric pairs, not only a better efficiency would be observed, but also a frequency lock-in would be achieved.

3.6 Conclusion

The results presented here provide a new insight on the dynamics of a piezoelectric energy-harvesting flag. First and foremost, they emphasise how the fundamental dynamics of the energy harvesting system and of the output circuit may strongly impact the motion of the structure and its energy harvesting performance. Also, they identify two major performance enhancements associated with the resonant behaviour of the circuit, namely

- a destabilisation of the fluid-solid-electric system, leading to spontaneous energy harvesting at lower velocity; and
- a lock-in of the fluid-solid dynamics on the circuit's fundamental frequency, resulting in an extended resonance and a significant increase of the harvested energy.

This lock-in behaviour at the heart of both effects above is classically observed in VIV where it is also responsible for maximum energy harvesting [Grouthier 2014]; it is in fact a general consequence of the coupling of an unstable fluid-solid system to another oscillator's dynamics. We therefore expect that the conclusions presented in the present work go beyond the simple inductive-resistive circuit considered here, and should be applicable to a much larger class of resonant systems. Such systems could be other forms of electrical output circuits, or other mechanical oscillators. In his work, Emmanuel Virot [Virot 2015] studied the coupling between a flag and a mass-spring system. He identified a frequency lock-in between the flag and the spring, leading to significantly larger amplitude of the flag. This concept is intimately associated with the lock-in phenomenon reported in our work and therefore constitutes an interesting path to follow.

To a larger extent, the lock-in phenomenon could be considered as a consequence resulting from any coupling of two or more vibration systems. Such mechanism could therefore be applied to other kinds of vibration-based energy-harvesting technologies, such as electrostatic energy harvesting [Perez 2015], and energy harvesting using magnetic induction.

The critical impact of the coupling coefficient α on the system's performance is also underlined in the present work through its strong influence on the destabilisation range and the lock-in range. The choice of the piezoelectric materials is therefore essential in the practical achievement of high efficiency.

These results nonetheless illustrate the fundamental insights and technological opportunities offered by the full coupling of a passive resonant system (electric, mechanical or other) to an unstable piezoelectric structure for the purpose of energy harvesting. The lock-in phenomenon and the enhanced performance demonstrated by the coupling between the piezoelectric flag and a simple resonant circuit open the perspective of applying different kinds of resonant systems to energy-harvesting piezoelectric system. The choice of an inductive circuit is motivated by its simplicity, while in practice, other designs of resonant circuits may present important advantages over the proposed formulation in our work. Meanwhile, complex circuitry, such as electric networks [Bisegna 2006] and active circuits [Lefeuvre 2006], also represent interesting perspectives of the present work. In the next chapter, we will investigate one of the above mentioned complex circuitry, namely the non-local electric network.

Chapter 4

Non-local electric network

Flags covered by continuously distributed small piezoelectric pairs will remain the subject of interest in this chapter. However, a different kind of circuit will be used to these flags. Instead of circuits connecting only the two patches within each piezoelectric pair, which are referred as local circuits, we are interested in a non-local electric network that is deployed on the flag and connects all piezoelectric pairs to their neighbours.

In [Bisegna 2006], it has been shown that using electric networks could enhance vibration control of structures by piezoelectric patches, it is therefore reasonable to imagine that interesting effects would also be introduced to energy harvesting using electric networks. Moreover, each local circuit harvests solely the energy produced by the piezoelectric pair to which it is connected, and consequently separates the flag into a set of independent electricity sources so that the flag's dynamic as a whole is not involved. Also, it is quite unlikely that energy harvested in each local circuit would practically be "summed". The advantage of non-local networks over local circuits is that they effectively connect all piezoelectric pairs on the flag into one single circuit, thereby making the whole flag into a single electricity source. For this reason, compared with the local circuits studied in the previous chapter, non-local electric networks are more likely to be applied in a prototype of a flag covered by multiple piezoelectric patches.

4.1 Equations of non-local electric network

We are interested in the configuration given in Fig. 4.1. On each surface of the flag, an electric network interlinks piezoelectric pairs, following [Bisegna 2006]. In Fig. 4.1, the impedance embedded in the electric network is denoted by Z for the sake of generality. The equivalent circuit of Fig. 4.1 is obtained and given in Fig. 4.2.

From the equivalent circuit presented in Fig. 4.2, one may derive the governing equations of this electric network using Kirchhoff's laws. Similar to Chapter 3, governing equations of the electric network interlinking a finite number of piezoelectric pairs distributed on the flag will be derived; next, using the same assumptions in Chapter 3, the corresponding governing equations will be derived for the continuous distribution of infinitesimal piezoelectric pairs.

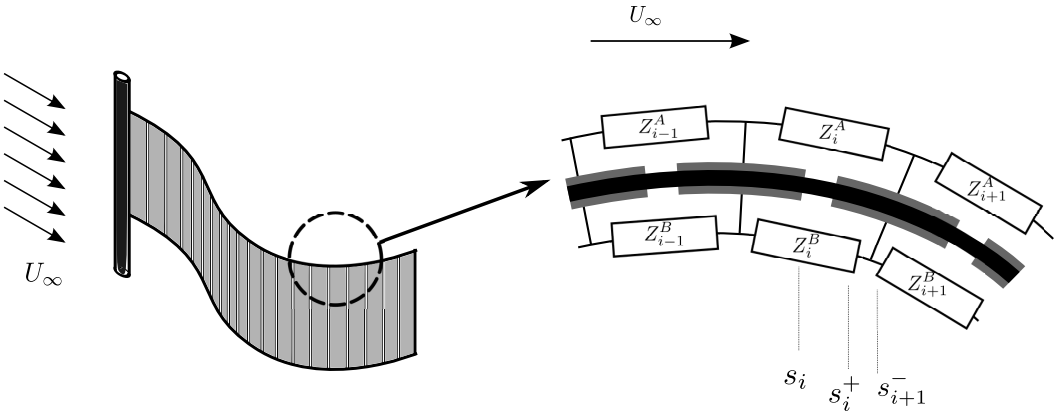

Figure 4.1: (left) 3D schematic representation of a piezoelectric flag with (right) a detailed representation of non-local electric network connected with piezoelectric pairs.

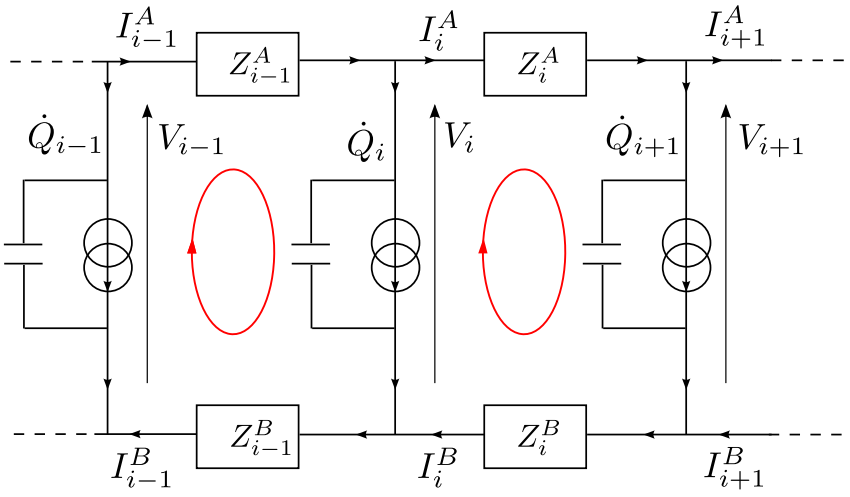

Figure 4.2: Equivalent circuit of a piezoelectric flag connected with a non-local electric network. All quantities associated to the upper surface (resp. lower surface) are denoted with the superscript A (resp. B). Red oval arrows indicate the prescribed positive direction when applying the Kirchhoff's laws.

4.1.1 Flag covered by a finite number of piezoelectric pairs

We consider first the situation where the flag is covered by a finite number of piezoelectric pairs of same length l_p. These pairs are continuously distributed on the flag so that $s_{i+1} - s_i = s_i^+ - s_i^- = l_p$. Applying Kirchhoff's current law on the nodes associated with the i^{th} piezoelectric pair, we obtain:

$$I_{i-1}^A - I_i^A - \frac{\partial q_i}{\partial t} l_p = 0, \tag{4.1}$$

$$I_{i-1}^B - I_i^B - \frac{\partial q_i}{\partial t} l_p = 0, \tag{4.2}$$

where $q = Q/l_p$ is the linear density of electric charge flowing through the piezoelectric pairs.

We apply then Kirchhoff's voltage law on the loop between the $i-1^{\text{th}}$ and i^{th} pair. It yields:

$$V_{i-1} - V_i - Z_{i-1}^A \cdot I_{i-1}^A - Z_{i-1}^B \cdot I_{i-1}^B = 0. \tag{4.3}$$

Note that the impedance Z are defined as operators. As simple examples, a such operator corresponding to a resistor $\mathcal{R}$, applied on an electric current I, is given by:

$$Z_{\mathcal{R}} \cdot I = \mathcal{R} I, \tag{4.4}$$

and for an inductor $\mathcal{L}$, we have:

$$Z_{\mathcal{L}} \cdot I = \mathcal{L} \frac{\mathrm{d}I}{\mathrm{d}t}. \tag{4.5}$$

4.1.2 Periodic networks and continuous limit

A simplification proposed in [Bisegna 2006] is to consider that the electric networks on the upper and lower surfaces of the flag are periodic, meaning that between any two consecutive piezoelectric pairs, the impedance is identical, i.e. $Z_i^A = Z^A$, and $Z_i^B = Z^B$. As a result, Eq. (4.3) becomes:

$$V_{i-1} - V_i - Z^A \cdot I_{i-1}^A - Z^B \cdot I_{i-1}^B = 0, \tag{4.6}$$

Using the notations introduced in Chapter 1, we may write:

$$I_{i-1} = I(s_i - l_p/2), \quad I_i = I(s_i + l_p/2), \tag{4.7}$$

$$Z_{i-1} = Z(s_i - l_p/2), \quad Z_i = Z(s_i + l_p/2), \tag{4.8}$$

$$V_i = V(s_i), \tag{4.9}$$

$$Q_i = Q(s_i). \tag{4.10}$$

We consider also linear density of impedance: $z_A = Z^A/l_p$ and $z_B = Z^B/l_p$, respectively on the upper and lower surfaces of the flag. As a result of introducing these lineic quantities, Eqs. (4.1)–(4.3) become:

$$I^A(s_i - l_p/2) - I^A(s_i + l_p/2) - \dot{q}(s_i) l_p = 0, \tag{4.11}$$

$$I^B(s_i - l_p/2) - I^B(s_i + l_p/2) - \dot{q}(s_i)l_p = 0. \tag{4.12}$$

$$V(s_{i-1}) - V(s_i) - z_A l_p \cdot I^A(s_i - l_p/2) - z_B l_p \cdot I^B(s_i - l_p/2) = 0. \tag{4.13}$$

The continuous limit is obtained by studying Eqs. (4.11)–(4.13) at the limit where $l_p \to 0$. Equations (4.11)–(4.12) yield:

$$\frac{\partial q}{\partial t} = -\frac{\partial I^A}{\partial t}, \tag{4.14}$$

$$\frac{\partial q}{\partial t} = -\frac{\partial I^B}{\partial s}. \tag{4.15}$$

And Eq. (4.13) yields the following continuous equation:

$$\frac{\partial v}{\partial s} + z_A \cdot I_A + z_B \cdot I^B = 0. \tag{4.16}$$

From Eqs. (4.14) and (4.15), we obtain:

$$\frac{\partial I^A}{\partial s} = \frac{\partial I^B}{\partial s}. \tag{4.17}$$

Supposing that the flag's trailing edge is not directly connected to its leading edge, implying $I^A(s = 0) = I^B(s = 0)$ and $I^A(s = L) = I^B(s = L)$, we can integrate the previous equation to obtain:

$$I^B = I^A = I. \tag{4.18}$$

We replace in Eq. (4.16) the quantity I^B by Eq. (4.18), it yields:

$$\frac{\partial v}{\partial s} + z \cdot I = 0, \tag{4.19}$$

where $z = z_A + z_B$. Equation (4.19) shows that the configuration in Fig. 4.1 is equivalent to its one-side version, i.e. it is not important on which side of the flag the impedance z is embedded. Consequently, in the remaining of this document, no distinction will be made between the surfaces A and B. As a result, Eqs. (4.14) and (4.15) become simply one equation:

$$\frac{\partial q}{\partial t} + \frac{\partial I}{\partial s} = 0. \tag{4.20}$$

4.1.3 Boundary conditions and energy balance

Besides different equations for the system's electric state, another novelty introduced by the electric network is that boundary conditions are required to close these equations. Since the flag has a finite length, so does the electric network deployed on it. Therefore at leading edge ($s = 0$) and trailing edge ($s = L$), additional relations between v and I should be prescribed.

In our study, we consider two simple configurations of boundary conditions, both consisting of attaching an external resistor, $\mathcal{R}_{\text{ext}}$, to either the leading edge (Type A) or the trailing edge (Type B), while on the other edge, the piezoelectric patches are connected by a wire. As an example, the boundary conditions of Type A is presented in Fig. 4.3.

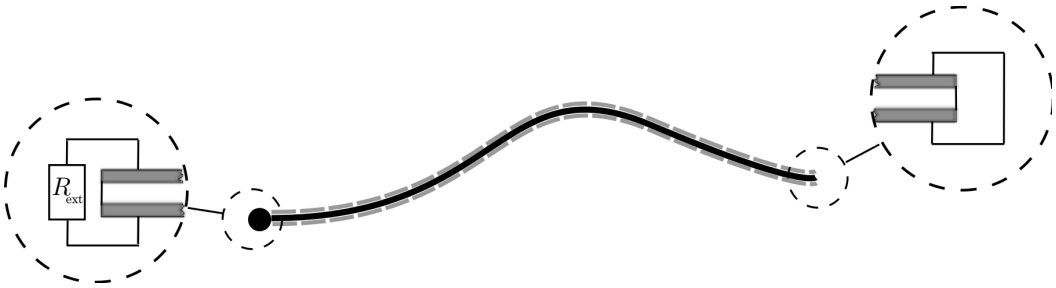

Figure 4.3: Boundary conditions (Type A): a harvesting resistor $\mathcal{R}_{\text{ext}}$ is connected at the leading edge of the flag. On the trailing edge, two patches are connected by a conducting wire.

The resistor $\mathcal{R}_{\text{ext}}$ is the useful load of the electric network, and will be referred as "harvesting resistor" in the following text.

By applying Kirchhoff's laws, these boundary conditions are given by the following equations:

$$\text{Type A:} \qquad z \cdot v(0,t) = \mathcal{R}_{\text{ext}} \frac{\partial v}{\partial s}\Big|_{s=0,t}, \qquad v(L,t) = 0, \tag{4.21}$$

$$\text{Type B:} \qquad v(0,t) = 0, \qquad z \cdot v(L,t) = -\mathcal{R}_{\text{ext}} \frac{\partial v}{\partial s}\Big|_{s=L,t}, \tag{4.22}$$

Therefore, the system of equations describing the electric network is:

$$\frac{\partial v}{\partial s} + z \cdot I = 0, \tag{4.23}$$

$$\frac{\partial q}{\partial t} + \frac{\partial I}{\partial s} = 0, \tag{4.24}$$

with the boundary conditions given by one of Eqs. (4.21) or (4.22). Note that in Eqs. (4.23) and (4.24), v is the voltage applied on the piezoelectric pairs, and q is the linear density of electric charge flowing through the piezoelectric pairs.

The harvested power $\mathcal{P}$, is consequently defined as:

$$\text{Type A:} \quad \mathcal{P} = \frac{< v^2(0,t) >}{\mathcal{R}_{\text{ext}}}, \tag{4.25}$$

$$\text{Type B:} \quad \mathcal{P} = \frac{< v^2(L,t) >}{\mathcal{R}_{\text{ext}}}. \tag{4.26}$$

4.1.4 Dimensionless Equations

Using the same characteristic scales as in previous chapters, the dimensionless form of Eqs. (4.23) to (4.24) are written as:

$$\frac{\partial v}{\partial s} + \tilde{z} \cdot I = 0, \tag{4.27}$$

$$\frac{\partial q}{\partial t} + \frac{\partial I}{\partial s} = 0. \tag{4.28}$$

Notice that $\tilde{z}$ is defined as "dimensionless impedance". For different types of components (resistor, inductor,), this quantity is expressed as:

$$\tilde{z}_R \cdot I = \beta I, \tag{4.29}$$

$$\tilde{z}_L \cdot I = \frac{1}{\omega_0^2} \frac{\partial I}{\partial t}, \tag{4.30}$$

where:

$$\beta = \frac{\mathcal{R}\mathcal{C}U_\infty}{L}, \quad \omega_0 = \frac{L}{U_\infty \sqrt{\mathcal{L}\mathcal{C}}}. \tag{4.31}$$

It is important to mention that $\mathcal{R}$ and $\mathcal{L}$ in Eq. (4.31) represent the *total* resistance or inductance in the embedded circuit, while $\mathcal{C}$ is the *total* intrinsic capacitance of all piezoelectric pairs. Although the electric state is characterised here by linear quantities, we do not choose linear densities of $\mathcal{R}$, $\mathcal{L}$ and $\mathcal{C}$ in the definitions of β and ω_0 as to keep their definition formally similar to those in previous chapters.

The boundary conditions are also written in dimensionless form as:

$$\text{Type A:} \qquad \tilde{z} \cdot v(0,t) = \beta_{\text{ext}} \frac{\partial v}{\partial s}\Big|_{s=0,t}, \qquad v(1,t) = 0, \tag{4.32}$$

$$\text{Type B:} \qquad v(0,t) = 0, \qquad \tilde{z} \cdot v(1,t) = -\beta_{\text{ext}} \frac{\partial v}{\partial s}\Big|_{s=1,t}, \tag{4.33}$$

where the parameter β_{ext}, given by:

$$\beta_{\text{ext}} = \frac{\mathcal{R}_{\text{ext}}\mathcal{C}U_\infty}{L} \tag{4.34}$$

characterises the external harvesting resistor. The dimensionless harvested power is therefore given by:

$$\text{Type A:} \quad \mathcal{P} = \frac{< v^2(0,t) >}{\beta_{\text{ext}}} \tag{4.35}$$

$$\text{Type B:} \quad \mathcal{P} = \frac{< v^2(1,t) >}{\beta_{\text{ext}}} \tag{4.36}$$

Equations (4.27)–(4.33) are combined with Eqs. (3.8), (3.9), (3.12) and (3.13), as well as the clamped-free boundary conditions given by Eqs. (3.15)–(3.16), to constitute the governing equations of the coupled system.

In the next two sections, we will investigate two fundamental circuits. In Section 4.2, the embedded impedance is only composed of resistors, and the corresponding circuits will be referred as "purely resistive circuits"; while in Section 4.3, inductors constitute the embedded impedance, and the corresponding circuits will be referred as "purely inductive circuits".

4.2 Purely resistive circuits

Purely resistive circuits imply that the impedance is given by $\tilde{z} = \beta$, therefore the equation describing the circuit is:

$$\frac{\partial v}{\partial t} - \frac{1}{\beta}\frac{\partial^2 v}{\partial s^2} + \frac{\alpha}{U^*}\frac{\partial^2 \theta}{\partial s \partial t} = 0. \tag{4.37}$$

The two types of boundary conditions are written as:

$$\text{Type A:} \qquad \beta v(0,t) = \beta_{\text{ext}} \frac{\partial v}{\partial s}\Big|_{s=0,t}, \qquad v(1,t) = 0, \tag{4.38}$$

$$\text{Type B:} \qquad v(0,t) = 0, \qquad \beta v(1,t) = -\beta_{\text{ext}} \frac{\partial v}{\partial s}\Big|_{s=1,t}. \tag{4.39}$$

We choose for now to study only boundary conditions of Type A. Using nonlinear numerical simulations, we vary β and β_{ext} to study the influence of embedded resistors and harvesting resistor on the harvesting efficiency. The efficiency η as a function of both β and β_{ext} is plotted in Fig. 4.4a, b, respectively for $M^* = 1$ and $M^* = 10$. Figures 4.4c, d show the flapping motion corresponding to these two values of M^*. Other parameters are $\alpha = 0.3$, $H^* = 0.5$, and $U^* = 15$.

For both values of M^*, the simulations show that the flapping dynamics for both M^* are barely impacted by varying β and β_{ext}: for $M^* = 1$, the flapping frequency is $\omega = 1.76$, and for $M^* = 10$, we obtained $\omega = 6.67$. In terms of energy harvesting, we observed that no energy is harvested at large values of β_{ext} and β. This result is expected: the case of large β_{ext} is equivalent to an open circuit at $s = 0$ and therefore no dissipation is possible; large values of β correspond to large embedded resistors, in which case the entire electric network is equivalent to an open circuit, and consequently no electric charge is flowing in the network. Meanwhile, we observe that there are two peaks of harvesting efficiency for both values of M^*. These two peaks are separated by a zone where efficiency is almost 0. An explanation to the observation of two peaks can be partly obtained by studying the response of Eq. (4.37) with the boundary condition given by Eq. (4.38) under a prescribed forcing.

In Eq. (4.37), we will replace the last term, corresponding to a forcing resulted from the flag's flapping, by a simpler forcing term. Equation (4.37) becomes therefore a diffusion equation with a oscillating source term. This operation will lead to a relation between β and β_{ext} that determines the location of the maximal harvested power.

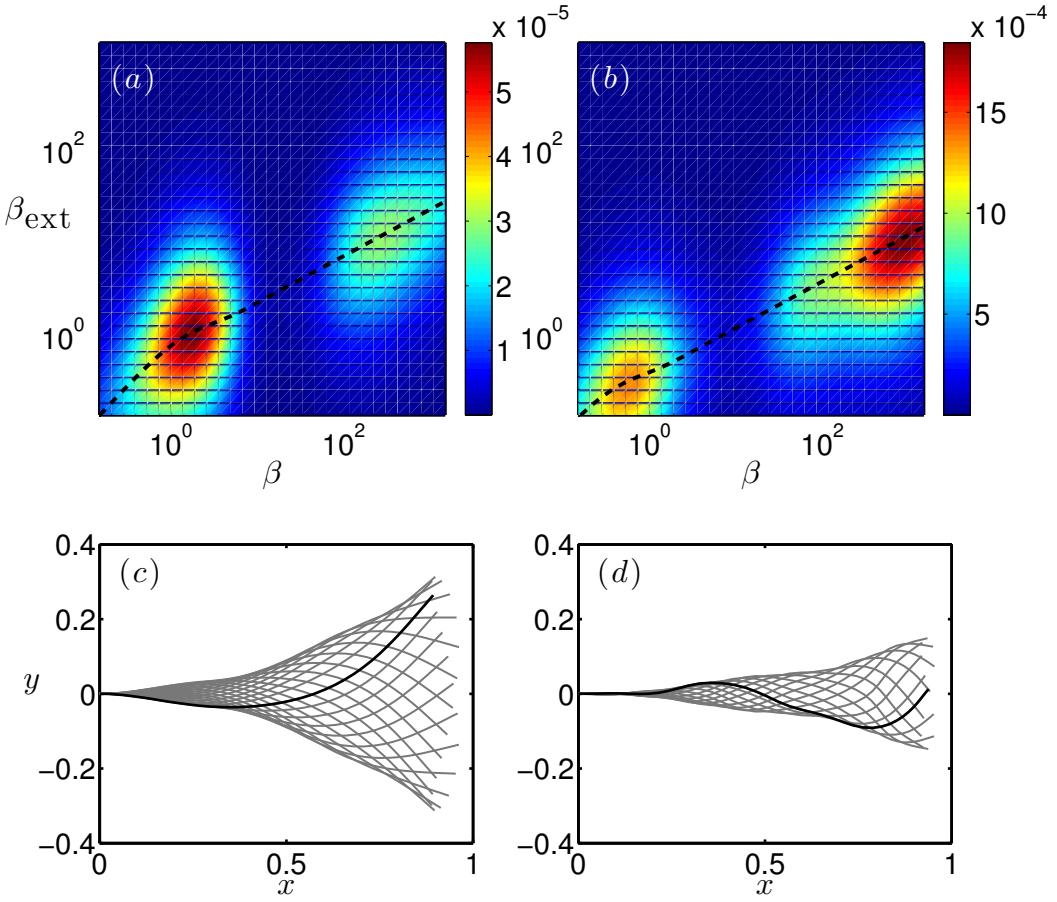

Figure 4.4: In (a, b): harvesting efficiency η as a function of β and β_{ext} for (a) $M^* = 1$ and (b) $M^* = 10$, with boundary conditions of Type A. Other parameters are $\alpha = 0.3$, $H^* = 0.5$, and $U^* = 15$. Values of β_{ext} given by Eq. (4.42) is presented by the dashed curve. In (c, d): flapping motion for (c) $M^* = 1$, $\beta = 0.13$, $\beta_{\text{ext}} = 0.07$, $\omega = 1.7$ and (b) $M^* = 10$, $\beta = 794.7$, $\beta_{\text{ext}} = 9.3$ and $\omega = 6.2$. In both cases, $\alpha = 0.3$, $H^* = 0.5$ and $U^* = 15$.

Since the deformation of a flapping flag is similar to a propagative wave, the forcing term can take the form of $\theta = \Theta_0 e^{j(ks-\omega t)}$, where Θ_0 is a constant, and ω is the flapping frequency. The substitution of θ in Eq. (4.37) by this expression suggests that the voltage v, as a linear response of the forcing θ, must also take a similar form, as

$$v(s,t) = \tilde{V}_0 e^{j(ks-\omega t)}, \tag{4.40}$$

where $\tilde{V}_0$, the complex amplitude of v, is a function of β and β_{ext}. We therefore attempt to find the maximum of harvested power, which, in the current case, is given by:

$$\mathcal{P} = \frac{\tilde{V}_0 \tilde{V}_0^*}{\beta_{\text{ext}}}, \tag{4.41}$$

where $\tilde{V}_0^*$ denotes the complex conjugate of $\tilde{V}_0$. For a given value of β, we derive an expression of β_{ext} maximising $\mathcal{P}$, which is the following:

$$\beta_{\text{ext}}^2 = \frac{\beta(1 + e^{-2\sqrt{2\beta\omega}} - e^{-2\sqrt{2\beta\omega}} \cos\sqrt{2\beta\omega})}{\omega(1 + e^{-2\sqrt{2\beta\omega}} + e^{-2\sqrt{2\beta\omega}} \cos\sqrt{2\beta\omega})}. \tag{4.42}$$

The result obtained using Eq. (4.42) is also plotted on Fig. 4.4*a*, *b* with black dashed curves, superposing the nonlinear numerical simulation results. We notice that Eq. (4.42) does not depend on k, suggesting that in the case of finite length flags, this relation stands valid for all vibration modes. In Fig. 4.4*a*, *b*, we can observe that for both values of M^*, the curve crosses the peaks of energy-harvesting efficiency, while the flapping motion corresponding to these two M^* are different (Fig. 4.4*c*, *d*). The good agreement of Eq. (4.42) with the results of numerical simulations confirms the validity of the relation between β and β_{ext}, given by Eq. (4.42), that leads to high harvesting efficiency, and that this relation is valid regardless of vibration mode.

The reason of the zero-efficiency zone separating two peaks for both M^* can be found by investigating the dissipation in the embedded resistors. This dissipation rate is formally given by:

$$\mathcal{P}_{\text{int}} = \frac{1}{\beta} \int_0^1 v^2 \mathrm{d}s. \tag{4.43}$$

Michelin & Doaré [Michelin 2013] found that the maximal dissipation rate is achieved when the perfect tuning is reached between the circuit's characteristic time scale and the flapping frequency. In our case, the circuit's characteristic time scale τ can be obtained by solving the circuit's equation without the coupling term:

$$\frac{\partial^2 v}{\partial s^2} - \beta \frac{\partial v}{\partial t} = 0, \tag{4.44}$$

with the corresponding boundary conditions given by Eq. (4.38). The solution yields:

$$\tau = \frac{\beta}{\lambda^2}, \tag{4.45}$$

where λ is determined by the following equation:

$$\frac{\lambda}{\tan\lambda} + \frac{\beta}{\beta_{\text{ext}}} = 0. \tag{4.46}$$

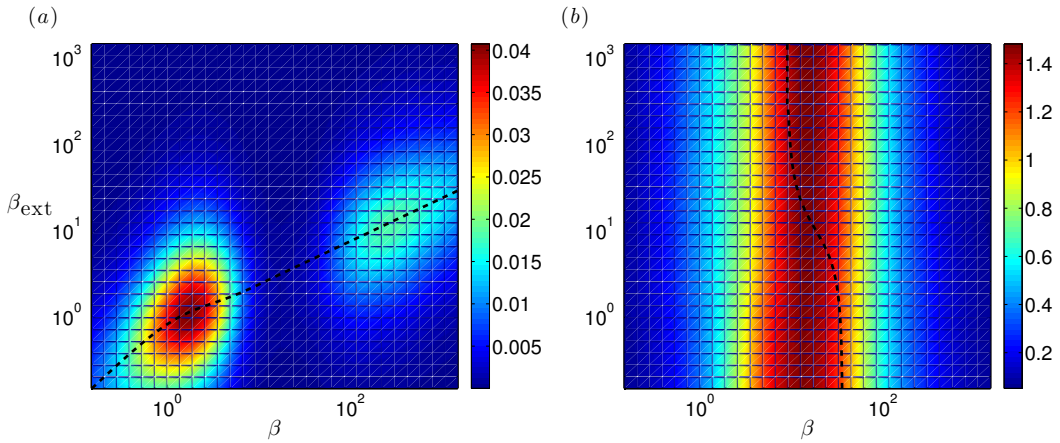

Figure 4.5: (a) Harvested power $\mathcal{P}$ and (b) embedded dissipation rate $\mathcal{P}_{\text{int}}$ as function of β and β_{ext}, with boundary conditions of Type A, $\alpha = 0.3$, $H^* = 0.5$, $M^* = 1$ and $U^* = 15$. Values of β_{ext} given by Eq. (4.42) is presented by the dashed curve in (a), and values of β given by Eq. (4.47) is presented by the dashed curve in (b).

Hence the optimal tuning implies:

$$\beta\omega\lambda^{-2} = 2\pi. \tag{4.47}$$

In Fig. 4.5, we plot both the harvested power $\mathcal{P}$ (Fig. 4.5a) and the rate of dissipation in the embedded resistors $\mathcal{P}_{\text{int}}$ (Fig. 4.5b) for $\alpha = 0.3$, $U^* = 15$, $M^* = 1$ and $H^* = 0.5$. We observe that the dissipation in embedded resistors $\mathcal{P}_{\text{int}}$ is indeed maximal when $\beta\omega\lambda^{-2} \sim 2\pi$ (Fig. 4.5b). When $\mathcal{P}_{\text{int}}$ reaches its maximum, the harvested power $\mathcal{P}$ decrease almost to 0, suggesting that a majority of electrical energy is dissipated in the embedded resistor and little is left for the harvesting resistor. The area of the maximal $\mathcal{P}$ is therefore cut through by the zone of the maximal $\mathcal{P}_{\text{int}}$, hence the presence of two peaks.

The above observation clearly suggests that a maximal dissipation in embedded resistors impairs the energy harvesting. A perfect tuning between τ and ω is undesirable to energy harvesting and therefore should be avoided when designing energy-harvesting devices based on the present electric networks.

4.3 Purely inductive circuits

4.3.1 Frequency lock-in

In a purely inductive circuit, the impedance $\tilde{z}$ is given by Eq. (4.30), hence the governing equation of the circuit:

$$\frac{\partial^2 v}{\partial t^2} - \omega_0^2 \frac{\partial^2 v}{\partial s^2} + \frac{\alpha}{U^*} \frac{\partial^3 \theta}{\partial t \partial s^2} = 0, \tag{4.48}$$

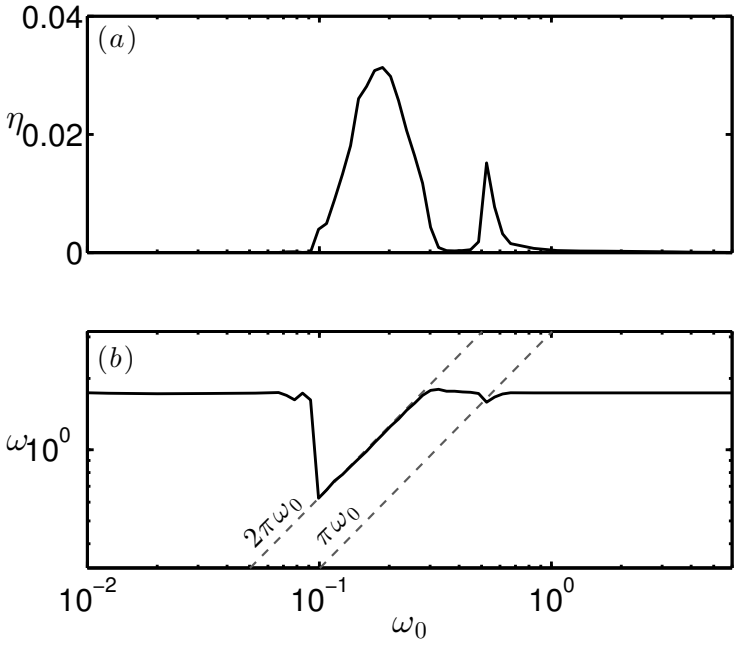

Figure 4.6: (a) Harvesting efficiency and (b) flapping frequency as a function of ω_0, with boundary conditions of Type B, $\alpha = 0.3$, $M^* = 1$, $U^* = 15$, $\beta_{\text{ext}} = 0.15$

with following boundary conditions given by:

$$\text{Type A:} \qquad \frac{\partial v}{\partial t}\Big|_{s=0,t} = \beta_{\text{ext}}\omega_0^2 \frac{\partial v}{\partial s}\Big|_{s=0,t} \qquad v(1,t) = 0, \tag{4.49}$$

$$\text{Type B:} \qquad v(0,t) = 0 \qquad \frac{\partial v}{\partial t}\Big|_{s=1,t} = -\beta_{\text{ext}}\omega_0^2 \frac{\partial v}{\partial s}\Big|_{s=1,t}. \tag{4.50}$$

Equation (4.48) is actually a wave equation with a source term. In this case, the parameter ω_0 represents the ratio of electrical phase speed to the flow speed.

In the case of purely inductive circuits, we study for now only the boundary conditions of Type B. We are interested in the evolution of both harvesting efficiency η and flapping dynamics, represented by the frequency ω, with varying ω_0 and β_{ext}, which are two controlling parameters of the electric network's property. We choose $\alpha = 0.3$, $U^* = 15$, $M^* = 1$ and $H^* = 0.5$ for numerical simulations. In Fig. 4.6, both quantities are plotted with varying ω_0 and $\beta_{\text{ext}} = 0.15$, a relatively small value; while in Fig. 4.7, we plot the two quantities with $\beta_{\text{ext}} = 141$, a larger value.

The harvesting efficiency (Figs. 4.6a and 4.7a) and the flapping frequency (Figs. 4.6b and 4.7b) are reminiscent of results presented in Chapter 3 (Fig. 3.6). In both figures, we can observe an increase in harvesting efficiency accompanied with "frequency lock-in". However, with the non-local electric network, the value which the flapping frequency locks to is not ω_0. And with varying ω_0, the frequency locks to multiple values.

The answer to this observation is to be sought by studying the circuit's property

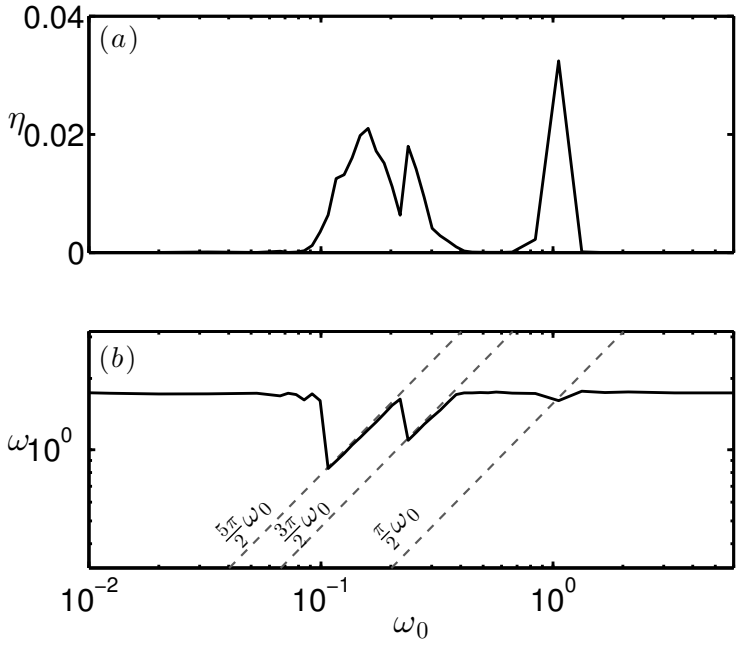

Figure 4.7: (a) Harvesting efficiency and (b) flapping frequency as a function of ω_0, with boundary conditions of Type B, $\alpha = 0.3$, $M^* = 1$, $U^* = 15$, $\beta_{\text{ext}} = 141$

from its governing equation. The equation of the circuit without forcing term reads:

$$\frac{\partial^2 v}{\partial t^2} - \omega_0^2 \frac{\partial^2 v}{\partial s^2} = 0. \tag{4.51}$$

with boundary conditions given by Eq. (4.50). It is a wave equation of which the general solution has the form:

$$v(s,t) = \tilde{V_0} \tilde{f}(s) \mathrm{e}^{\mathrm{j}\tilde{\omega}t}, \tag{4.52}$$

where $\tilde{f}(s) = \mathrm{e}^{\mathrm{j}\tilde{\lambda}s} + \tilde{C}\mathrm{e}^{-\mathrm{j}\tilde{\lambda}s}$ is the solution of the Helmholtz's equation:

$$\frac{\partial^2 \tilde{f}}{\partial s^2} + \tilde{\lambda}^2 \tilde{f} = 0, \tag{4.53}$$

with $\tilde{\lambda} = \pm\tilde{\omega}/\omega_0$.

Using boundary conditions of Type B, given by Eq. (4.50), we can determine that $\tilde{C} = -1$, and the complex $\tilde{\lambda}$, which has two expressions according to the value of $\beta_{\text{ext}}\omega_0$:

$$\beta_{\text{ext}}\omega_0 < 1 : \quad \tilde{\lambda} = n\pi + \frac{\mathrm{j}}{2}\ln\left(\frac{1-\beta_{\text{ext}}\omega_0}{1+\beta_{\text{ext}}\omega_0}\right), \tag{4.54}$$

$$\beta_{\text{ext}}\omega_0 > 1 : \quad \tilde{\lambda} = \left(n+\frac{1}{2}\right)\pi + \frac{\mathrm{j}}{2}\ln\left(\frac{\beta_{\text{ext}}\omega_0-1}{\beta_{\text{ext}}\omega_0+1}\right), \tag{4.55}$$

where n is 0 or a positive integer. The real part of $\tilde{\lambda}$ corresponds to the natural frequency of the circuit, while the imaginary part represents the damping induced by the harvesting resistor. We can see that the value of $\beta_{\text{ext}}\omega_0$ has an important influence on the circuit's behavior: if $\beta_{\text{ext}}\omega_0 \ll 1$, we have $\tilde{\lambda} \sim n\pi$, therefore the natural frequency of the circuit is consequently given by:

$$\omega_c = \omega_0\tilde{\lambda} = n\pi\omega_0, \tag{4.56}$$

and the corresponding mode $\tilde{f}(s)$ is

$$\tilde{f}(s) = \mathrm{e}^{\mathrm{j}\tilde{\lambda}s} - \mathrm{e}^{-\mathrm{j}\tilde{\lambda}s} = \pm\sin n\pi s. \tag{4.57}$$

while when $\beta_{\text{ext}}\omega_0 \gg 1$, we have $\tilde{\lambda} \sim (n+1/2)\pi$, the natural frequency is therefore:

$$\omega_c = \omega_0\tilde{\lambda} = \left(n + \frac{1}{2}\right)\pi\omega_0, \tag{4.58}$$

and the corresponding mode $\tilde{f}(s)$ is

$$\tilde{f}(s) = \mathrm{e}^{\mathrm{j}\tilde{\lambda}s} - \mathrm{e}^{-\mathrm{j}\tilde{\lambda}s} = \pm\sin\left(n + \frac{1}{2}\right)\pi s. \tag{4.59}$$

These results suggest that instead of one single value ω_0, the inductive circuit possesses more than one natural frequencies depending on the value of $\beta_{\text{ext}}\omega_0$. It is therefore reasonable that the flapping frequency does not lock to ω_0. Moreover, these results also imply that the lock-in phenomenon should be observed not only at one single frequency, but at multiple values. This is also confirmed by numerical simulation. In Fig. 4.6, we have $\beta_{\text{ext}} = 0.15$, leading to $\beta_{\text{ext}}\omega_0 \ll 1$ for the considered range of ω_0, and a natural frequency given by Eq. (4.56). Therefore the flapping frequency locks successively to $\pi\omega_0$ and $2\pi\omega_0$ with decreasing ω_0 (Fig. 4.6*b*). In Fig. 4.7, $\beta_{\text{ext}} = 141$, we then have $\beta_{\text{ext}}\omega_0 \gg 1$. The circuit's natural frequency is therefore determined by Eq. (4.58). The flapping frequency in this case locks successively to $\pi/2$, $3\pi/2$ and $5\pi/2$ with decreasing ω_0.

Figure 4.8 shows the flapping motion of flags (Fig. 4.8*a*,*c*) at each range of frequency lock-in, and the corresponding voltage profile along the flag (Fig. 4.8*b*, *d*) for the case of $\beta_{\text{ext}} = 0.15$. As expected, the flag flaps with large amplitude when it is at lock-in. The voltage profile also shows a form close to $\sin(n\pi s)$, which is the mode shape predicted by Eq. (4.57). For the case of $\beta_{\text{ext}} = 141$, results are presented in Fig. 4.9 and the same remarks apply. The accordance between the voltage profile and the electric mode shape indicates that while the system is at lock-in, the high harvesting efficiency is a result of the circuit working at resonance.

Meanwhile, we observe that for both cases ($\beta_{\text{ext}}\omega_0 \gg 1$ and $\beta_{\text{ext}}\omega_0 \ll 1$), similar efficiencies are obtained while the system works at lock-in, suggesting comparable amount of dissipation in β_{ext} in both cases. This observation can be explained from the electrical mode shapes in Figs. 4.8 and 4.9. When $\beta_{\text{ext}}\omega_0 \ll 1$, the electrical mode shape shows relatively low voltage at the trailing edge. However, as the circuit

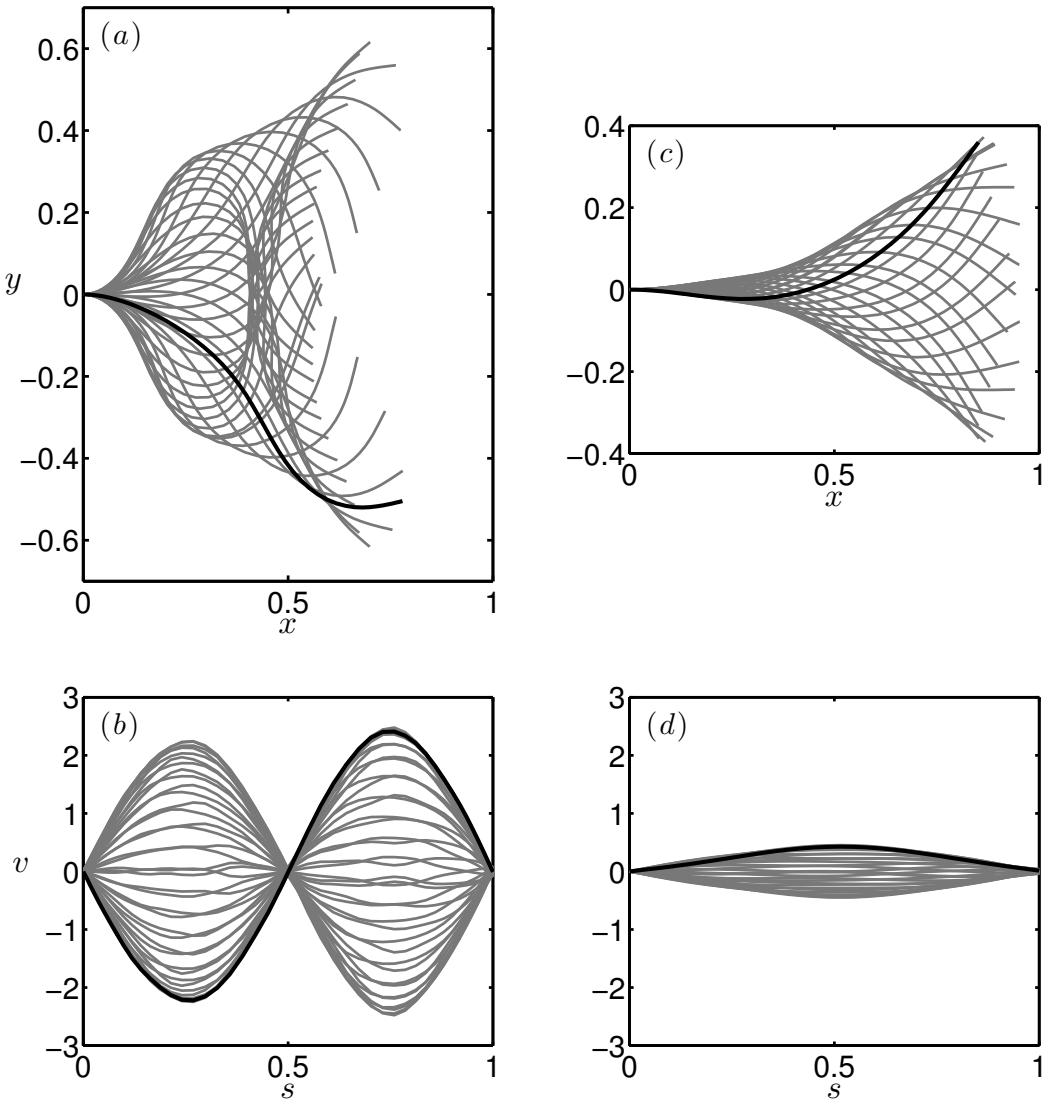

Figure 4.8: $(a, c,)$ Flapping motion of flags and (b, d) electric voltage along the flag with $\alpha = 0.3$, $M^* = 1$, $U^* = 15$, $\beta_{\text{ext}} = 0.15$ and (a, b) $\omega_0 = 0.19$ (c, d) $\omega_0 = 0.52$. The voltage profile is proportional to $\sin(2\pi s)$ in (b) and $\sin(\pi s)$ in (d).

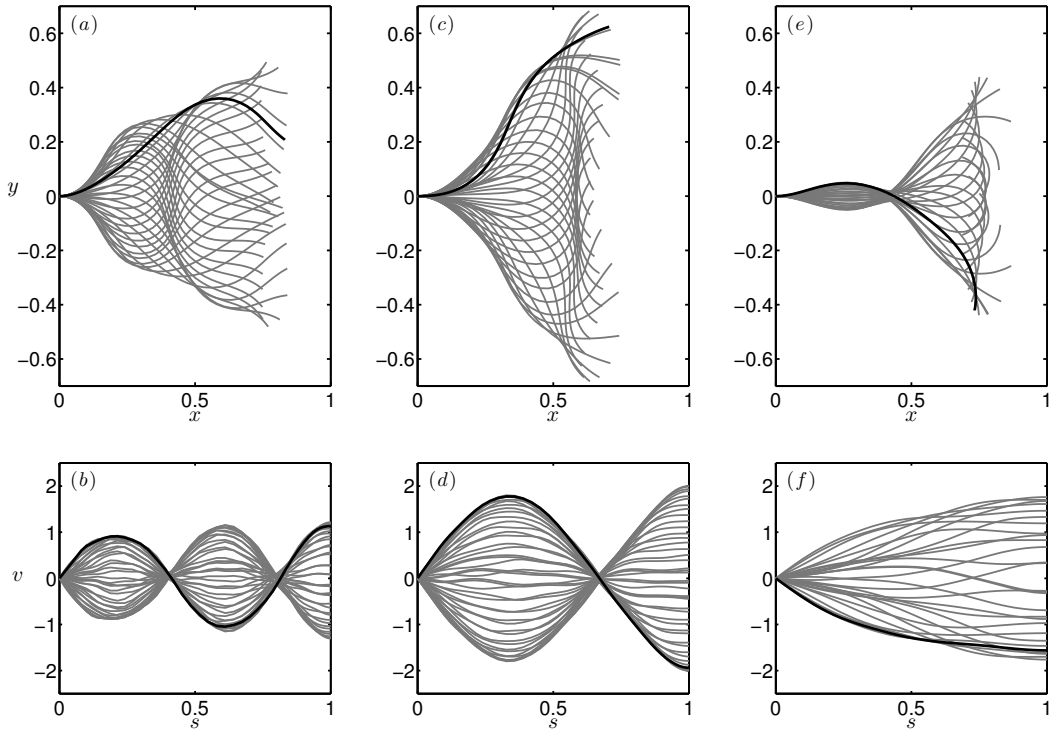

Figure 4.9: (a, c, e) Flapping motion of flags and (b, d, f) electric voltage along the flag with $\alpha = 0.3$, $M^* = 1$, $U^* = 15$, $\beta_{\text{ext}} = 141$ and (a, b) $\omega_0 = 0.16$, (c, d) $\omega_0 = 0.24$, (e, f) $\omega_0 = 1.06$. The voltage profile is proportional to $\sin(5\pi s/2)$ in (b), $\sin(3\pi s/2)$ in (d) and $\sin(\pi s/2)$ in (f).

is connected to a small harvesting resistance, the electrical current passing through the resistor is large enough to ensure a significant dissipation. When $\beta_{\text{ext}}\omega_0 \gg 1$, the circuit is connected to a large resistance, but the electrical modes in this case give a large voltage at the trailing edge, thus a large amount of dissipation in the resistor.

4.3.2 Energy harvesting at $\beta_{\text{ext}}\omega_0 \sim 1$

In Eqs. (4.54) and (4.55), we can see that the imaginary part of $\tilde{\lambda}$ is determined by the following expression:

$$Im(\tilde{\lambda}) = \frac{1}{2}\ln\left(\left|\frac{\beta_{\text{ext}}\omega_0 - 1}{\beta_{\text{ext}}\omega_0 + 1}\right|\right). \tag{4.60}$$

Equation (4.60) leads to the consequence that $Im(\tilde{\lambda}) = -\infty$ when $\beta_{\text{ext}}\omega_0 = 1$. This infinite damping implies two consequences: (i) as the circuit's natural frequency becomes purely imaginary, the frequency lock-in is not going to happen; (ii) a perfect absorption of the electric modes is introduced by the system's damping, of which the only contribution come from the harvesting resistor at $s = 1$. With this perfect absorption condition, theoretically any electrical energy generated in the circuit would be absorbed and dissipated by the harvesting resistor β_{ext}. It is therefore expected that significant improvement would be achieved under this condition even without frequency lock-in. This prediction is confirmed by results in Fig. 4.10, which shows η and ω as functions of β_{ext} for a value of ω_0 that does not lead to lock-in. We observe that when $\beta_{\text{ext}}\omega_0 \sim 1$, an increased harvesting efficiency is obtained even without having the system working at lock-in, as the frequency ω is unchanged, although the efficiency is not yet comparable to that obtained with frequency lock-in.

4.4 Electrical energy flux

In previous parts of this chapter, we studied two basic circuits using two types of boundary conditions. The critical factor that determines which type of boundary conditions to use is the electrical energy flux introduced by the electric network.

From Eqs. (4.27) and (4.28), as well as the direct piezoelectric effect, given by Eq. (3.8), we can derive the equations of local electrical energy conservation. Replacing q in Eq. (4.28) by Eq. (3.8), and multiplying the resulting equation by v, we obtain:

$$v\frac{\partial v}{\partial t} + v\frac{\partial I}{\partial s} + \frac{\alpha}{U^*}v\frac{\partial^2\theta}{\partial t\partial s} = 0, \tag{4.61}$$

which can be arranged and be rewritten as:

$$\frac{1}{2}\frac{\partial}{\partial t}(v^2) + \frac{\partial}{\partial s}(vI) - \frac{\partial v}{\partial s}I + \frac{\alpha}{U^*}v\frac{\partial^2\theta}{\partial t\partial s} = 0. \tag{4.62}$$

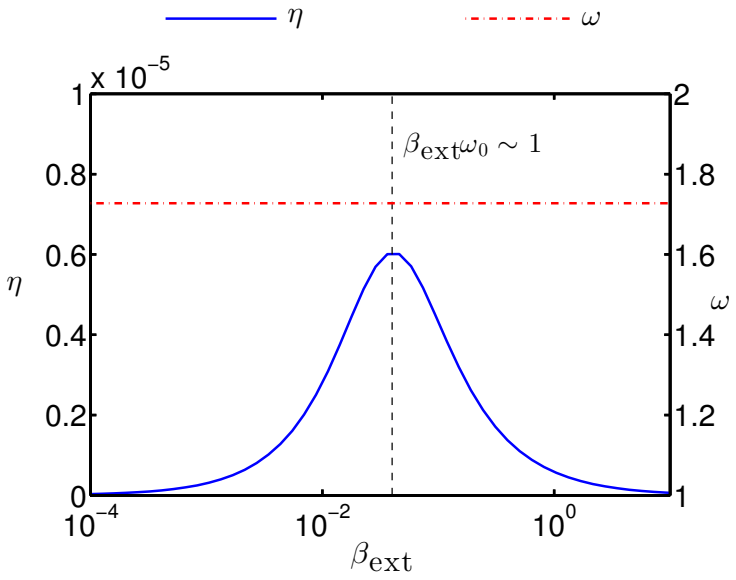

Figure 4.10: Harvesting efficiency and flapping frequency with $\alpha = 0.3$, $M^* = 1$, $U^* = 15$, and $\omega_0 = 6.7$.

Equation (4.27) leads to:

$$\frac{\partial v}{\partial s} I = -(z \cdot I) I. \tag{4.63}$$

Equation (4.62) can therefore be written as:

$$\frac{\partial \mathscr{E}_c}{\partial t} + \mathscr{P}_z = \mathscr{T} + \frac{\partial F_{\text{elec}}}{\partial s}, \tag{4.64}$$

where $\mathscr{E}_C$, $\mathscr{P}_z$, and $\mathscr{T}$ are respectively the energy stored in the intrinsic capacitance, the rate of electrical energy variation due to embedded impedance, and the rate of energy transfer from the structure to the circuit. They are given by:

$$\mathscr{E}_C = \frac{1}{2} v^2, \quad \mathscr{P}_z = (z \cdot I) I, \quad \mathscr{T} = -\frac{\alpha}{U^*} v \frac{\partial^2 \theta}{\partial t \partial s}. \tag{4.65}$$

In the case of the purely resistive circuits, $\mathscr{P}_z = \beta I^2$ represents the rate of dissipation in the embedded resistors, and with the purely inductive circuits, $\mathscr{P}_z$ is the variation of energy stored in the inductance. The electrical energy flux, F_{elec}, is given by:

$$F_{\text{elec}} = -vI. \tag{4.66}$$

The average in time of F_{elec} gives information about the direction of propagation of electrical energy. A better energy harvesting strategy should consist of placing the harvesting resistor on the spot towards which a larger amount of electrical energy converges.

In the case of purely resistive circuits, we plotted the time average of F_{elec} for both Types of boundary conditions in Fig. 4.11. We observe that with Type A, a

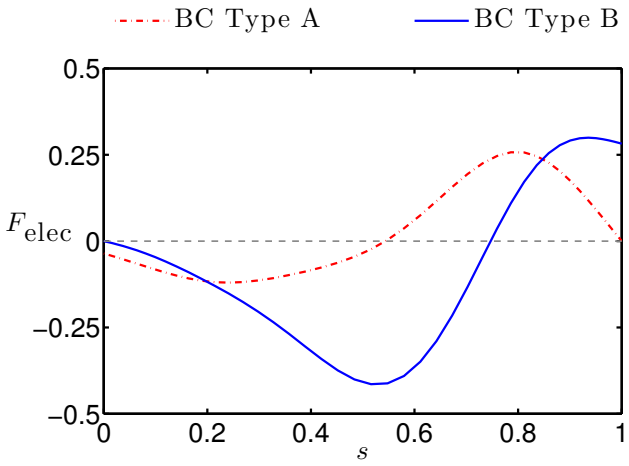

Figure 4.11: Electrical energy flux along the flag using the boundary conditions of Type A and Type B, with $\alpha = 0.3$, $M^* = 1$, $U^* = 15$, $\beta = 0.13$ and $\beta_{\text{ext}} = 0.067$.

small amount of electrical energy is flowing towards and absorbed at $s = 0$, while a much higher peak of electrical energy flux, situated close to $s = 1$, is heading towards the trailing edge. With boundary conditions of Type B, a much larger amount of electrical energy is absorbed at $s = 1$. A high peak of electrical energy flux is also observed heading towards $s = 0$. However, this peak is situated far from $s = 0$, and is decaying rapidly with decreasing s. These results shows clearly that for the same set of parameters, circuits with the boundary conditions of Type B prevails against Type A in terms of energy harvesting.

The efficiency of energy harvesting with Type B is plotted in Fig. 4.12. Comparing Figs. 4.4*a* and 4.12, we observe that with the harvesting resistor placed at the trailing edge, the system harvests nearly 10 times more energy than a resistor placed at the leading edge for the considered parameters. This advantage possessed by the trailing edge harvesting is also reflected in terms of energy dissipation in both embedded resistors and harvesting resistors, plotted in Fig. 4.13. In Fig. 4.13, one can observe that not only more energy is harvested by $\mathcal{R}_{\text{ext}}$ (Fig. 4.13*a*), but also less energy is dissipated in the embedded resistors (Fig. 4.13*b*), which is beneficial to the energy harvesting.

In the case of purely inductive circuits, the same observation holds. In Fig. 4.14, we plot electrical energy flux for both types of boundary conditions using purely inductive circuit, with the parameters satisfying $\beta_{\text{ext}}\omega_0 \sim 1$. Figure 4.14 shows that for the same set of parameters, the boundary conditions of Type B allows almost all electrical energy flux being directed towards the trailing edge, leading to a better energy harvesting performance; while with Type A, only a small amount of electric energy flux is heading toward the leading edge, and the majority of energy flux still tends to flow towards $s = 1$.

An indication of the reason why more electrical energy flux heads towards the trailing edge could be found by studying the relation between F_{elec} and the mechan-

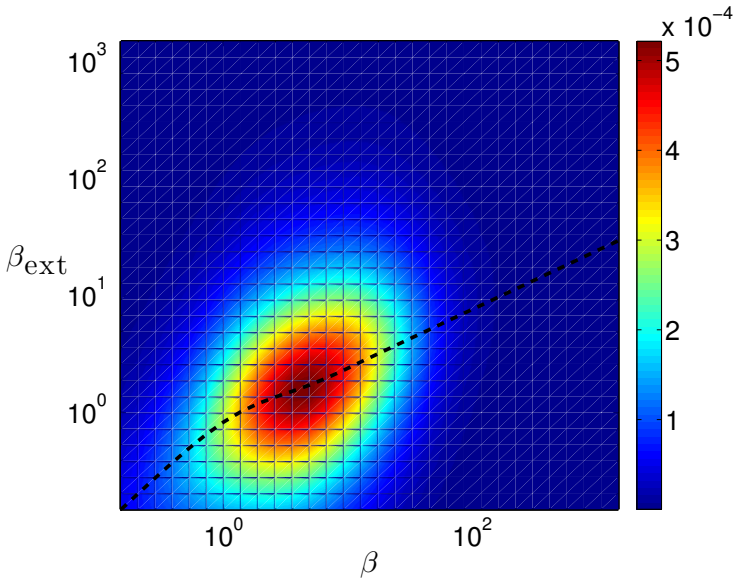

Figure 4.12: Harvesting efficiency η as a function of β and β_{ext}, with boundary conditions of Type B. $\alpha = 0.3$, $H^* = 0.5$, $M^* = 1$ and $U^* = 15$. Values of β_{ext} given by Eq. (4.42) is presented by the dashed curve.

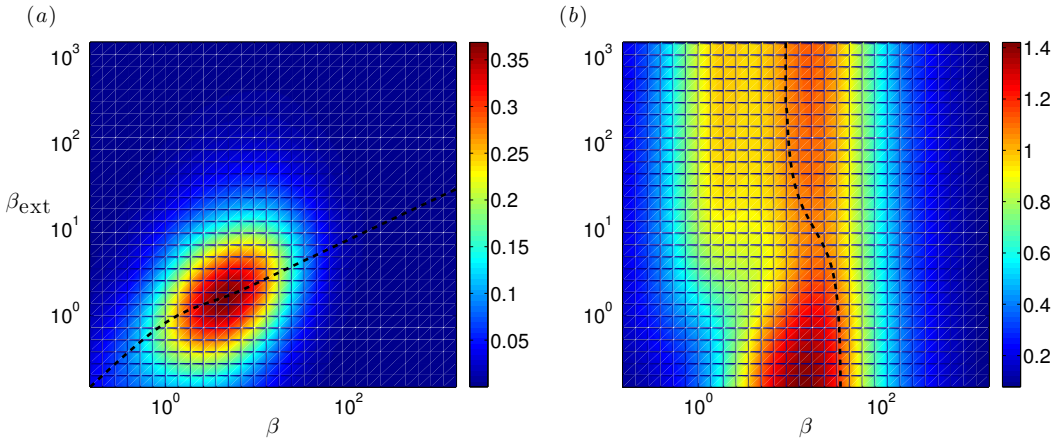

Figure 4.13: (a) Harvested power $\mathcal{P}$ and (b) embedded dissipation rate $\mathcal{P}_{\text{int}}$ as function of β and β_{ext}, with boundary conditions of Type B. $\alpha = 0.3$, $H^* = 0.5$, $M^* = 1$ and $U^* = 15$. Values of β_{ext} given by Eq. (4.42) is presented by the dashed curve in (a), and values of β given by Eq. (4.47) is presented by the dashed curve in (b).

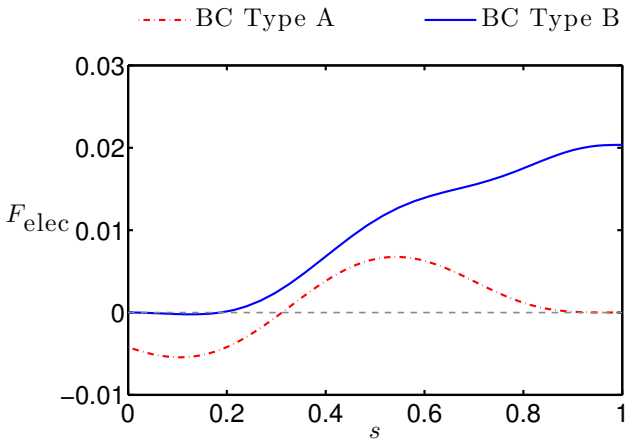

Figure 4.14: Electrical energy flux along the flag with $\alpha = 0.3$, $M^* = 1$, $U^* = 15$, $\omega_0 = 6.7$ and $\beta_{\text{ext}} = 0.04$ ($\beta_{\text{ext}}\omega_0 \sim 1$), for the boundary conditions of Type A (dash-dotted) and Type B (solid)

ical energy flux F_{mech}, defined in the previous chapter by Eq. (3.26). We notice that in Eq. (3.26), two terms represent the contribution of piezoelectric effects to the mechanical energy fluxes. They are given by:

$$F_{\text{p1}} = -\frac{\alpha}{U^*} v \frac{\partial \theta}{\partial t}, \quad F_{\text{p2}} = \frac{\alpha}{U^*} v \frac{\partial \mathbf{x}}{\partial t} \cdot \mathbf{n}. \tag{4.67}$$

From Eq. (4.28), and the direct piezoelectric effect, given by Eq. (3.8), one may notice that the electric current I and the derivative in time of θ are closely related through:

$$\frac{\partial I}{\partial s} = -\frac{\partial q}{\partial t} = \frac{\alpha}{U^*} \frac{\partial^2 \theta}{\partial t \partial s} + \frac{\partial v}{\partial t}. \tag{4.68}$$

Equation (4.68) shows that:

$$I \sim \frac{\partial \theta}{\partial t}, \tag{4.69}$$

suggesting that the electrical energy flux is related to F_{p1}. We plot the three quantities, i.e. F_{p1}, F_{p2} and F_{elec} in Fig. 4.15, using a configuration where $\beta_{\text{ext}} = 0$, i.e. both at leading edge and trailing edge of the flag, two piezoelectric patches are connected by a conducting wire instead of a harvesting resistor. As a result, the influence of boundary conditions on the electrical energy flux is excluded.

The results in Fig. 4.15 clearly show the almost identical evolution of F_{p1} and F_{elec}. Both F_{p1} and F_{elec} show a much higher peak of energy flux flowing towards $s = 1$ near the trailing edge, while for the part of energy flux heading towards $s = 0$, the peak is much lower. Physically, this observation can be explained by the clamped-free boundary conditions applied on the flag. Equation (4.69) shows that the order of magnitude of I, subsequently that of F_{elec}, is proportional to the derivative in time of θ, which is zero at the fixed leading edge, and increases as we move towards the free trailing edge, leading to a high peak of electrical energy flux

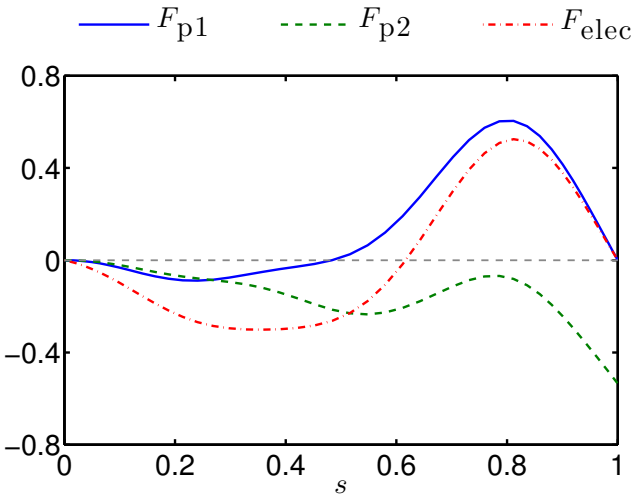

Figure 4.15: Electrical energy flux and the contributions of piezoelectric effects to the mechanical energy flux along the flag with $\beta_{\mathrm{ext}} = 0$, $\alpha = 0.3$, $M^* = 1$, $U^* = 15$, and $\beta = 0.13$.

near the trailing edge. This explanation suggests that near the free end of a flag, one can expect more electrical energy flux available, it is therefore preferable to connect the harvesting resistor to the electrodes situated at the free end of the flag in order to profit from this abundance of energy flux.

4.5 Conclusion and perspectives

In this chapter, we investigated the energy harvesting of piezoelectric flags using a non-local electric network. By studying two elementary configurations, i.e. purely resistive circuits and purely inductive circuits, we observed that by connecting all piezoelectric pairs into one circuit, such non-local electric networks allow energy harvesting by a harvesting resistor placed at one end of the flag. This resistor harvests energy through the electric energy flux flowing along the flag. In the case of purely resistive circuit, the dissipation in the embedded resistors acts against the energy harvesting, therefore needs to be suppressed by avoiding the resistors' tuning with the flapping motion. With purely inductive circuits, we identified that even without frequency lock-in, inductance could act in favour to energy harvesting by applying a perfect absorption boundary condition on either the leading edge or the trailing edge (preferred) of the flag, although frequency lock-in is still a more desirable effect to the energy harvesting.

As mentioned at the beginning of the chapter, in practice, non-local electric networks are more likely to be used than local circuits studied in the previous chapter. The results in this chapter showed the feasibility of such concept and proved that such electric network induces a deeper interaction between the electrical system and the fluid-solid system: the non-local circuits introduce modal dynamics to the

electrical system that interacts with the flag's flexibility, leading to a lock-in phenomenon at multiple frequencies. Although the results presented here are obtained using the assumption of infinitesimal piezoelectric electrodes, we expect them to be also applicable in other configurations consisting of a flag covered by piezoelectric electrodes of finite size [Piñeirua 2015].

The benefit of coupling the piezoelectric flag with a resonant system is again found in this chapter. The inductive network, acting as a multi-modal oscillator, induces a frequency lock-in to the coupled fluid-solid-electric system. This lock-in phenomenon maintains the circuit working at resonance, thus yielding a high energy-harvesting efficiency. Moreover, as in the previous chapter, where we found common points between the piezoelectric flag coupled with resistive-inductive loop with VIV of rigid cylinders through the frequency lock-in phenomenon, a similar comparison can be made here between the non-local electric network and the VIV of flexible cables [Grouthier 2014]. As a flexible cable, an inductive network possesses multiple natural frequencies and natural electrical modes, which appear while frequency lock-in, as shown in Figs. 4.8 and 4.9. The fact that with non-local electric networks, energy harvesting becomes efficient by exploiting electrical energy flux, is also similar to the results in [Grouthier 2014], that a flexible cable generates a mechanical energy flux and produces an efficient energy harvesting.

A more promising strategy to fully exploit the frequency lock-in as well as energy fluxes is to position harvesters at spots corresponding to crests of electric wave, making use of the large amplitude of electric voltage. However, the locations of energy harvesters might also modify the voltage distribution as well as the electrical energy flux. It is therefore important to understand the impact of the energy harvesters' positions on the electrical modes and identify optimal locations of harvesting resistors in future work.

Chapter 5

Coupled flutter

This chapter will focus on the influence of the hydrodynamic coupling between two flags on energy harvesting. The motivation of studying the energy harvesting of two flags lies in the small quantity of energy that one single piezoelectric flag can harvest. Using more than one flags is an interesting path of designing further applications capable of harvesting a large quantity of energy. Investigating the coupling of two flags constitutes a first step on this path.

The coupled flutter is an intriguing subject associated with flapping flags. It involves two or more flexible flags placed in a flow. Under the action of the flow, these flags will become unstable and flap. So far, the most extensively studied configurations are: (i) two flags placed side by side and (ii) two flags placed in tandem. Using ingenious techniques consisting of soap film and flexible filaments, some experimental works [Zhang 2000, Jia 2007] are performed to study two flags placed side-by-side in a 2D uniform flow. The results showed that with varying distance which separates the two flags, the flags establish sometimes an in-phase flapping, sometimes an out-of-phase flapping. This conclusion is substantiated by many numerical studies [Zhu 2003, Farnell 2004, Alben 2009b] where similar observations were found. Some studies, using analytic and numerical approaches, examined the linear stability of two flags placed side by side [Jia 2007, Michelin 2009]. They also found that according to the distance, the most unstable flapping mode switches between the in-phase mode and the out-of-phase mode. In addition, they also discovered the destabilising effect of small distance.

Two flags placed in tandem, i.e. one flag on the direct downstream of the other, are also studied by numerous researchers [Ristroph 2008, Zhu 2009, Alben 2009b]. In this configuration, the *trailing flag* (flag placed downstream) is necessarily forced by the wake of the flapping of the *leading flag* (flag placed upstream), leading to two consequences which are the following:

- Compared with one single flag's flapping, the amplitude of the leading flag is reduced and that of the following flag is increased. In [Ristroph 2008], the authors explained that the reduction of the leading flag's amplitude is a result of the following flag's fixed leading edge, suppressing lateral flow near the leader's trailing edge, thus indirectly confining the leading flag. As for the follower's amplitude, its increase is mainly the result of the leading flag's wake, forcing the follower, and therefore leading to a large amplitude.

- Compared to the case of one single flag, the leading flag experiences less drag, while the trailing flag experiences more drag, contrary to the intuition based

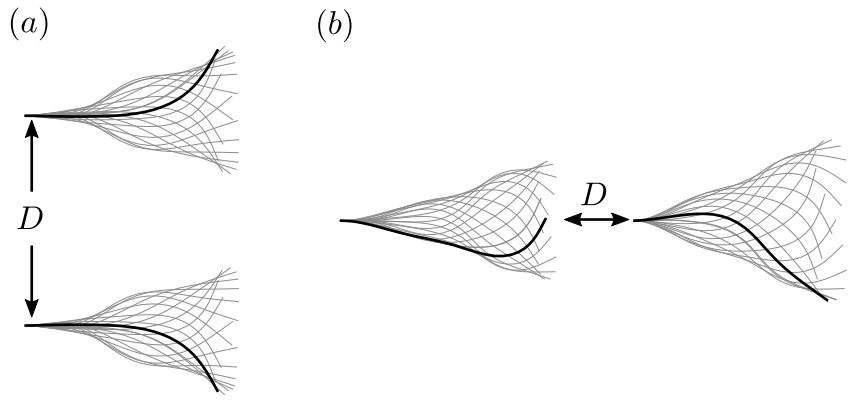

Figure 5.1: Definition of separation distance D for (a) side-by-side flags and (b) tandem flags.

on fixed rigid bodies. Ristroph & Zhang suggested that this observation, named as *inverted drafting*, is a direct consequence of the different amplitude experienced by the two flags [Ristroph 2008]. As the drag is proportional to the cross-section occupied by the flag's motion, characterised by its amplitude, the flag with smaller amplitude, i.e. the leader, experiences less drag than the follower, which flaps with a larger amplitude.

Energy harvesting using two piezoelectric flags is a relatively new field of study and one could not find many existing work. Recently, Song *et al.* [Song 2014] assessed energy harvesting potential of two piezoelectric flags placed in tandem and found that the larger amplitude of the trailing flag enhances the energy harvesting performance.

5.1 Two piezoelectric flags connected in one circuit

5.1.1 Electrical circuits

In our work, we will focus on the most studied configurations, i.e. two flags placed either side by side or in tandem. As presented in Chapter 1, an additional parameter, the separation distance D, will be involved in the modelling of the problem. For the flags placed side by side, D is taken as the distance separating the two flags' leading edge (Fig. 5.1a), while for two flags in tandem, D is taken as the distance separating the leading flag's trailing edge, and the following flag's leading edge, when both flags are at rest (Fig. 5.1b). The corresponding dimensionless parameter is defined as:

$$d = \frac{D}{L}. \tag{5.1}$$

In [Song 2014], Song *et al.* investigated two flags placed in a flow but electrically independent, i.e. their electrodes are not connected in the same circuit. As a result, only hydrodynamic effects were discussed in their work. However, as discussed in

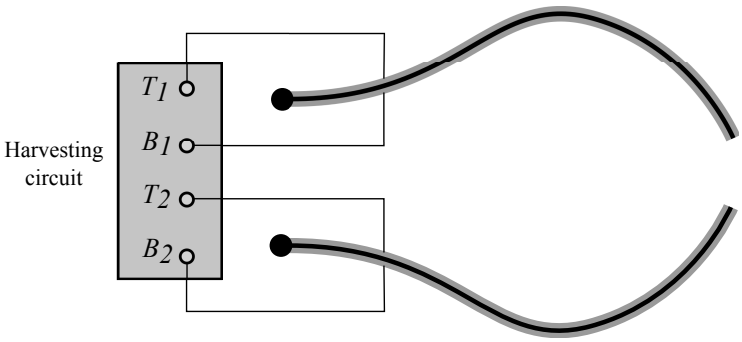

Figure 5.2: Schematic representation of two piezoelectric flags connected to an energy-harvesting electric system.

previous chapters, piezoelectric effects may also play crucial role on the flapping dynamics as well as on the energy harvesting. It is therefore reasonable to ask the following question: if two flags are coupled both hydrodynamically and electrically, how would the hydrodynamic coupling interact with the piezoelectric coupling? More precisely, will these two couplings enhance each other? or impair each other? In order to investigate these questions, we will couple the two flags electrically by connecting their electrodes into a same electric loop (Fig. 5.2).

Each flag considered here is covered by one single piezoelectric pair. From this piezoelectric pair, an electrode stretches out of each patch (see Fig. 5.2), which makes two electrodes per flag, respectively denoted as T for "top" and B for "bottom", with the index 1 and 2 distinguishing flag 1 and flag 2. In the following, flag 1 designates the upper flag in the side-by-side configuration, and the leading flag in the tandem configuration.

As for the circuit into which the flags' electrodes will be plugged, we will consider two simple configurations: a circuit containing only a resistor, called resistive circuit (Fig. 5.3*a*), and a circuit containing a resistor and an inductor connected in parallel, called inductive-resistive circuit (Fig. 5.3*b*). Two flags are connected to each circuit and we consider that the flags are in parallel connection (Fig. 5.3).

Due to the fact that each flag has two electrodes, we may consider two types of connections. The first one is to join T_1 to T_2, and B_1 to B_2. As we consider this connection to be the "normal" way to connect the electrodes, it will be referred as "normal connection" (NC) hereinafter. The second one is to join T_1 to B_2, and B_1 to T_2, which will be referred as "inverse connection" (IC) in contrast with the normal connection.

As a result of these two types of connections, the dimensionless equations of

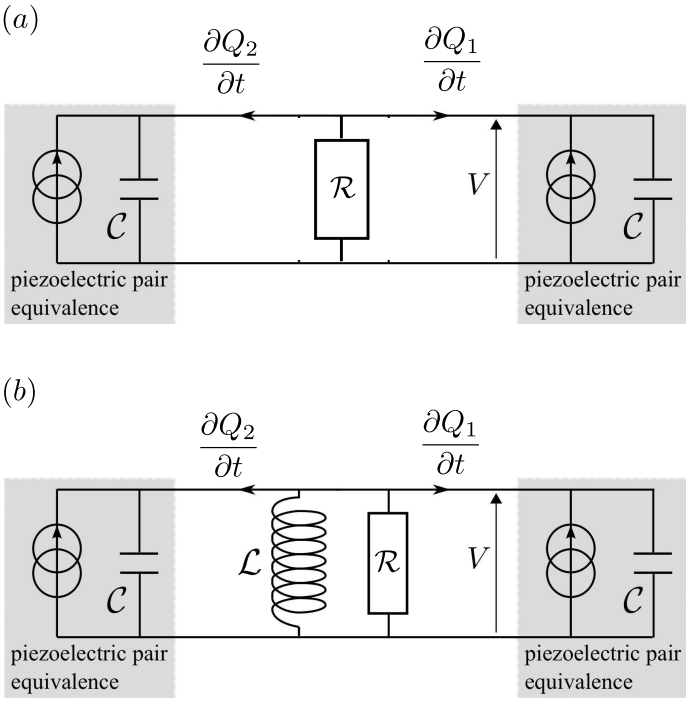

Figure 5.3: Equivalent circuit of two piezoelectric flags in parallel connection to (a) a purely resistive circuit, and (b) a parallel resistive-inductive circuit.

direct piezoelectric effect are written as follows:

$$\text{Normal connection:} \qquad Q_1 = 2[\alpha\theta_1(1) + V], \tag{5.2}$$

$$Q_2 = 2[\alpha\theta_2(1) + V], \tag{5.3}$$

$$\text{Inversed connection:} \qquad Q_1 = 2[\alpha\theta_1(1) + V], \tag{5.4}$$

$$Q_2 = 2[-\alpha\theta_2(1) + V]. \tag{5.5}$$

Indeed, if two flags' electrodes are connected to the same circuit, the voltage applied on them should be identical, hence the term $+V$ in all 4 equations. However, for a flag with inverse connection, the electric charge generated by a deformation characterised by $\theta(1)$ is of the opposite sign to the electric charge that would have been generated had the flag's electrodes are plugged in with normal connection, therefore the presence of "$-\alpha\theta_2(1)$" in Eq. (5.5), as opposed to the corresponding term in Eq. (5.3).

Governing equations for both connections are then derived. The dimensionless equations describing resistive circuits' behaviour are given as follows:

$$\text{NC:} \qquad 2\frac{\partial V}{\partial t} + \frac{V}{2\beta} + \frac{\alpha}{U^*}\left(\frac{\partial \theta_1}{\partial t}\Big|_{s=1} + \frac{\partial \theta_2}{\partial t}\Big|_{s=1}\right) = 0, \tag{5.6}$$

$$\text{IC:} \qquad 2\frac{\partial V}{\partial t} + \frac{V}{2\beta} + \frac{\alpha}{U^*}\left(\frac{\partial \theta_1}{\partial t}\Big|_{s=1} - \frac{\partial \theta_2}{\partial t}\Big|_{s=1}\right) = 0, \tag{5.7}$$

and the equations for resistive-inductive circuits are written as:

$$\text{NC:} \qquad 2\frac{\partial^2 V}{\partial t^2} + \frac{1}{2\beta}\frac{\partial V}{\partial t} + \frac{\omega_0^2}{4}V + \frac{\alpha}{U^*}\left(\frac{\partial^2 \theta_1}{\partial t^2}\Big|_{s=1} + \frac{\partial^2 \theta_2}{\partial t^2}\Big|_{s=1}\right) = 0, \tag{5.8}$$

$$\text{IC:} \qquad 2\frac{\partial^2 V}{\partial t^2} + \frac{1}{2\beta}\frac{\partial V}{\partial t} + \frac{\omega_0^2}{4}V + \frac{\alpha}{U^*}\left(\frac{\partial^2 \theta_1}{\partial t^2}\Big|_{s=1} - \frac{\partial^2 \theta_2}{\partial t^2}\Big|_{s=1}\right) = 0. \tag{5.9}$$

Equations (5.6)–(5.9) are obtained using the same characteristic scales used in previous chapters, so the dimensionless parameters β, α and ω_0 hold the same definitions as in Chapter 2.

Equations (5.6)–(5.9) suggest that the normal and inverse connections would act in favour of different phase shifts through piezoelectric effects. For example, in the normal connection, the additional torque induced by piezoelectric effects is identical on both flags. As a result, the normal connection favours the state of two flags having an in-phase flapping. The inverse connection, on the contrary, would favour the state of two flags having an out-of-phase flapping. As the effects of each connection are expected to be opposite to the other, in the following, we will centre our presentation on the normal connection, while the results obtained using the inverse connection will be briefly presented and compared with the normal connection.

5.1.2 Harvesting efficiency

For the case of two flags, the energy-harvesting efficiency is defined, in its dimensionless form, by the following expression:

$$\eta = \frac{< \mathcal{P} >}{< \mathcal{A}_1 > + < \mathcal{A}_2 >}, \tag{5.10}$$

where $< \mathcal{P} >$ is the time average of the rate of dissipation in the harvesting resistor $\mathcal{R}$, given in its dimensionless form by:

$$\mathcal{P} = \frac{V^2}{\beta}, \tag{5.11}$$

and $\mathcal{A}_1$ and $\mathcal{A}_2$ are respectively the dimensionless flapping amplitude of flag 1 and flag 2. This definition is actually based on the same principle of the efficiency defined in the case of one single flag: they are both defined as the ratio between the useful harvested energy and the energy of the fluid flow in contact with the flags.

5.2 Fluid forcing: vortex sheet model

As mentioned in Chapter 1, the vortex sheet model for the fluid forcing will be used for this chapter, as the slender body approach based on Lighthill's LAEBT, in is local form presented in this work, is unable to reveal how the presence of a solid body, flexible or not, would alter the characteristics of the surrounding flow. The modelling of such characteristics is however paramount in the study of hydrodynamic

coupling of two or more flags. Consequently, we abandon the slender body approach and adopt the vortex sheet model [Alben 2009a], which has already been used for the study of two flags' coupled flutter [Alben 2009b].

In high Reynolds number flows, a vortex sheet is a simplified modelling for the effect of viscosity in producing vorticity within boundary layers along a solid/flow interface, which, in our case, is the flag. The vorticity is developed along the flag, and is shed from the flag's trailing edge. The vorticity zone corresponding to each flag (flag i, $i = 1, 2$) is modelled as a vortex sheet represented by the contour C_i, which is composed of a bound vortex sheet attached to the flag, denoted by the contour C_f^i, and a free vortex sheet representing the wake being shed from the flag's trailing edge, denoted by C_w^i [Alben 2009a]. This vortex sheet is characterised by its strength $\gamma(s,t)$, which gives the tangential velocity jump across C_i. The flow is inviscid and irrotational outside of each vortex sheet, and its velocity is a sum of a uniform base flow along the x-direction, and the velocity induced by the vortex sheets through the Biot-Savart kernel [Saffman 1992]. In the case of two flags, the velocity of the flow is written in dimensionless form as:

$$\tilde{\mathbf{U}}(\mathbf{x},t) = \mathbf{e}_x + \frac{1}{2\pi \mathrm{j}} \int_{C_1} \frac{\gamma_1(s',t)}{\mathbf{x} - \mathbf{x}_1(s',t)} \mathrm{d}s' + \frac{1}{2\pi \mathrm{j}} \int_{C_2} \frac{\gamma_2(s',t)}{\mathbf{x} - \mathbf{x}_2(s',t)} \mathrm{d}s', \tag{5.12}$$

where $\tilde{\mathbf{U}}$ denotes the complex conjugate of the flow velocity $\mathbf{U}$. The first integral on the right-hand side of Eq. (5.12) represents the contribution of the vortex sheet belonging to flag 1, and the second integral represents the contribution given by the vortex sheet of flag 2. It is therefore necessary to find γ in order to obtain the full description of the flow.

The variable γ is determined by studying the relation between the flag and the vortex sheet. The presence of the flag on C_f^i enforces the condition of impermeability, i.e. the normal component of the vortex sheet velocity $\mathbf{u}_i$ should be equal to the normal component of the flag's velocity, given by $\partial \mathbf{x}_i / \partial t$. Taking the flag 1 for example, its impermeability condition is written as:

$$\frac{\partial \mathbf{x}_1}{\partial t} \cdot \mathbf{n}_1 = \mathbf{u}_1(s,t) \cdot \mathbf{n}_1, \quad s \in C_f^1. \tag{5.13}$$

In Eq. (5.13), the motion of the flag is governed by the Euler-Bernoulli beam model with the clamped-free boundary conditions, as given by Eq. (1.3) in Chapter 1; while the velocity of the vortex sheet $\mathbf{u}$ is found through averaging the limits of $\mathbf{U}$ from above and below C_f^1. The velocity of the vortex sheet of flag 1, noted by $\mathbf{u}_1$ in Eq. (5.13), is given by:

$$\tilde{\mathbf{u}}_1(s,t) = \mathbf{e}_x + \frac{1}{2\pi \mathrm{j}} \fint_{C_1} \frac{\gamma_1(s',t)}{\mathbf{x}_1(s,t) - \mathbf{x}_1(s',t)} \mathrm{d}s' + \frac{1}{2\pi \mathrm{j}} \int_{C_2} \frac{\gamma_2(s',t)}{\mathbf{x}_1(s,t) - \mathbf{x}_2(s',t)} \mathrm{d}s', \tag{5.14}$$

where the the first integral on the right-hand side is a principal-value integral. In order to solve Eq. (5.13), an additional constraint is required on the total circulation about the flag and its shed vortex sheet. At each instant, the value of γ at

the trailing edge of the flag ($s = 1$), representing the rate of circulation flux from C_f^1 into C_w^1, is determined by an unsteady Kutta condition which enforces a finite velocity [Jones 2003]. Meanwhile, on the free vortex sheet C_w^1, Helmholtz's circulation theorem [Saffman 1992] ensures that the circulation of any material points on C_w^1, where there is no pressure jump, is invariant with time and space, i.e. the circulation of a material point located on s at a given instant t on C_w^1 is equal to its circulation when it is shed at $s = 1$ at a previous instant t_0. This circulation can be computed by applying Kelvin's theorem on C_f^1:

$$\Gamma_1(s,t) = \int_{s_m}^{s} \gamma_1(s',t)\mathrm{d}s' = \Gamma_1(1,t_0) = \int_0^1 \gamma_1(s',t_0)\mathrm{d}s', \quad s \in C_w^1, \tag{5.15}$$

where s_m represents the Lagrangian coordinate of the most dowstream point in the free vortex sheet. The invariance of Γ makes it convenient to describe the behaviour of C_w^i by studying its evolution in the Lagrangian frame attached to its average velocity.

The fluid forcing $\mathbf{F}_{\text{fluid}}$ applied on the flag 1 is the difference of the pressure forces above and below C_w^1. It is obtained using the Bernoulli's theorem [Jones 2003, Michelin 2008, Alben 2009a].

$$\mathbf{F}_{\text{fluid}} = [p]_1(s,t)\mathbf{n}_1 = \left(\int_0^s \frac{\partial \gamma_1}{\partial t} + [\mathbf{u}_{r1}(s,t) \cdot \boldsymbol{\tau}_1]\gamma_1(s,t) \right) \mathbf{n}_1, \tag{5.16}$$

where $\mathbf{u}_{r1}$ is the relative velocity between the flag 1 and the velocity of the vortex sheet C_f^1. With the pressure $[p]_1(s,t)$ applied on flag 1, it would perceive the presence of flag 2 and act consequently, thereby revealing the hydrodynamic coupling. The hydrodynamic effect is applied on the flag 2 in the reciprocal way.

The fluid-solid system of two flags is therefore described by Eqs. (5.13)–(5.16), as well as the Kutta's condition taken as a boundary condition for the vortex sheet at $s = 1$. These equations are solved numerically using a second-order scheme for the time-marching, and a Chebyshev collocation method for the derivation and integration in space. The numerical solution allows us to obtain γ, $\mathbf{x}$, and the circulation Γ of C_w^i, which are necessary quantities for describing the dynamics of the fluid-solid system. The details of the numerical method can be found in Appendix B.

5.3 Side-by-side flags

In this section, we will study the energy harvesting using two flags placed side-by-side. The main part of this section will be dedicated to the study of resistive circuits, while the results obtained using inductive circuits will be briefly presented at the end of the section. The interaction between the hydrodynamic coupling and the piezoelectric effects as well as their impacts on the energy harvesting will be the centre of this section. An important feature of coupled flutter is the phase difference $\Delta\phi$ between two flags. Many studies [Zhang 2000, Farnell 2004, Jia 2007] reported

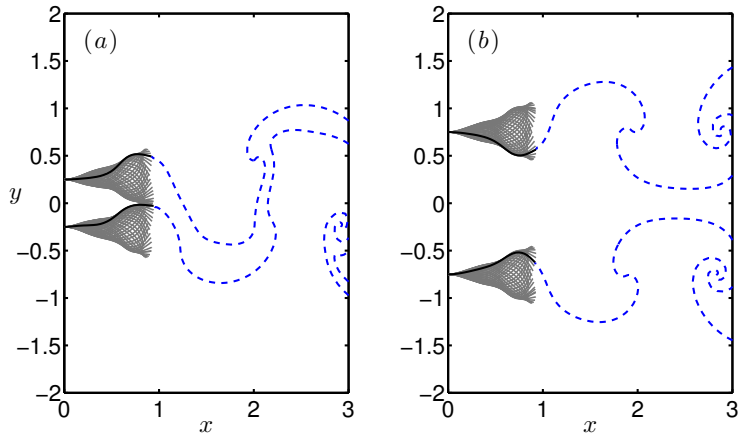

Figure 5.4: Flapping motion of two side-by-side flags without piezoelectric coupling ($\alpha = 0$). In (a): $d = 0.5$, in-phase flapping and in (b): $d = 1.5$, out-of-phase flapping. Other parameters are $M^* = 3$ and $U^* = 13$.

two possible states: (i) in-phase flapping, or $\Delta\phi = 0$, and (ii) out-of-phase flapping, corresponding to $\Delta\phi = \pm\pi$. The transition between the two states occurs when the distance separating the two flags varies. In order to illustrate how the phase shift impacts the energy harvesting, we choose at first two distances: $d = 0.5$, where two flags of $M^* = 3$ and $U^* = 13$ with $\alpha = 0$ exhibit in-phase flapping (Fig. 5.4a), and $d = 1.5$, where the flapping is out of phase (Fig. 5.4b).

Using the parameters M^*, U^* and d, we investigate the influence of these two flapping states on the energy harvesting. As mentioned previously, we will elaborate our presentation using the normal connection. In the last paragraph of this section, results obtained using the inverse connection will be briefly presented, and then compared with the normal connection.

5.3.1 Influence of in-phase and out-of-phase flapping

We start by assessing the influence of the flapping pattern on the energy-harvesting performance. We place two flags at two different distances, one corresponding to an in-phase flapping and the other an out-of-phase flapping. The energy harvesting efficiency for both cases are plotted in Fig. 5.5.

In Fig. 5.5, we observe that with normal connection, the in-phase flapping mode leads to a much higher energy-harvesting efficiency than the out-of-phase flapping mode. These results show that the phase difference has an important impact on the energy harvesting. We can explain this observation by examining the equations describing the resistive circuit using the normal connection. In Eq. (5.6), the term accounting for the electric charge generation reads:

$$\text{coupling} = \frac{\alpha}{U^*}\left(\frac{\partial\theta_1}{\partial t}\Big|_{s=1} + \frac{\partial\theta_2}{\partial t}\Big|_{s=1}\right). \tag{5.17}$$

This term involves time derivatives of two flags' trailing edge angle: $\theta_1(1)$ and $\theta_2(1)$,

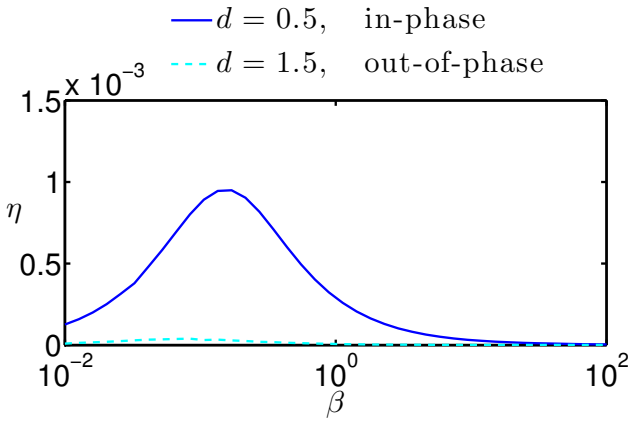

Figure 5.5: Harvesting efficiency η as function of β with $d = 0.5$ and $d = 1.5$ using Normal Connection. Other parameters are $M^* = 3$, $U^* = 13$, $\alpha = 0.3$.

which are of same order of magnitude both in the case of in-phase and out-of-phase flapping, but of different sign in the latter case. As a result, with the normal connection, the in-phase flapping leads to a reinforced coupling while the out-of-phase flapping cancels out the coupling, leading to a negligible amount of harvested energy.

In addition, the flapping frequencies of both flags are almost identical, $\omega_1 = \omega_2 = 3.26$, and are not changed with varying β. The value of β leading to the maximal efficiency corresponds to the situation where the circuit's time scale is tuned with the flags' flapping frequency, as reported in [Michelin 2013]. In the case of two flags, the circuit's characteristic time scale is determined by the resistance and the intrinsic capacitance of both flags, and the perfect tuning is achieved when $\beta\omega \sim 1/2$.

5.3.2 Influence of separation distance d

In [Alben 2009b], Alben, also using the vortex sheet model, has found that instead of switching between 0 and π, $\Delta\phi$ actually varies continuously with the distance d. Based on the results in Fig. 5.5 showing the critical impact of $\Delta\phi$, we may expect that the evolution of efficiency η would follow the variation of $\Delta\phi$. In Fig. 5.6, we plot the phase difference $\Delta\phi$ (Fig. 5.6*a*) and the harvesting efficiency η (Fig. 5.6*b*) as function of d, for different values of α. In Fig. 5.6, For $\alpha = 0.3$ and $\alpha = 0.6$, we observe that at small values of d, $\Delta\phi$ evolves in the same way as the case of $\alpha = 0$ (Fig. 5.6*a*), with $\Delta\phi \sim 0$ at first, leading to high efficiency η (Fig. 5.6*b*), which starts to drop as $\Delta\phi$ varies to $-\pi$ with increasing d. However, at large d, $\Delta\phi$ no longer follows the evolution obtained with $\alpha = 0$, and tends to a fixed value that is close to $\Delta\phi = 0$. Meanwhile, η starts to increase again as d increases, which undoubtedly due to a flapping pattern tending to an in-phase one, favoured by the normal connection.

The results shown above suggest that when two flags are close, the hydrodynamic effect still dominates, and acts either to enhance the energy harvesting or to diminish

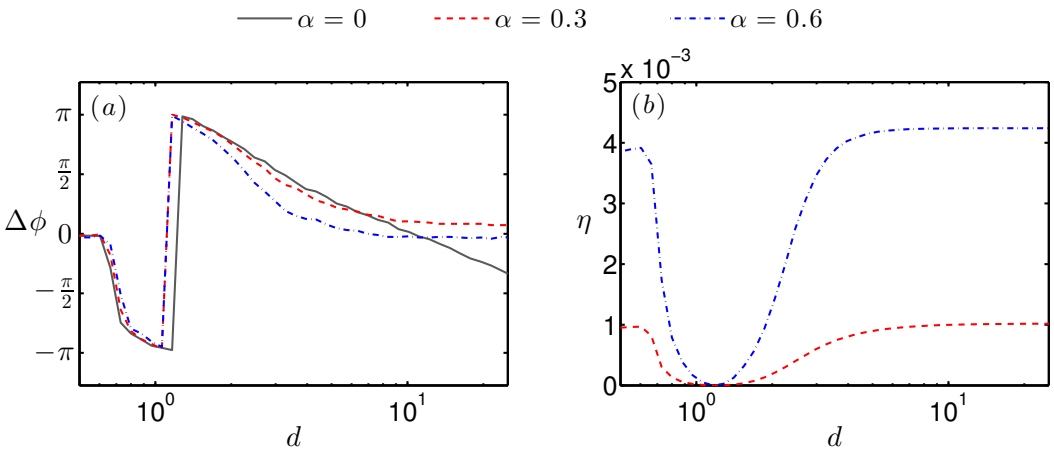

Figure 5.6: (a) Phase shift $\Delta\phi$ and (b) harvesting efficiency η as function of distance d, for $\alpha = 0$, $\alpha = 0.3$, and $\alpha = 0.6$, using normal connection. Other parameters are $M^* = 3$, $U^* = 13$, $\beta = 0.15$.

it. The hydrodynamic effect is weakened with increasing d, giving an opportunity to the piezoelectric effect to take control of the flapping pattern. With the parameters used in Fig. 5.6 ($M^* = 3$ and $U^* = 13$), the piezoelectric effect acts in phase and therefore dictates the phase difference $\Delta\phi$.

At some other cases, the piezoelectric coupling still impacts on $\Delta\phi$ but may not be completely in favour of the energy harvesting. In Fig. 5.7, the phase shift (Fig. 5.7a) and the efficiency (Fig. 5.7b) are plotted for $M^* = 3$ and $U^* = 15$ with varying distance d. Figure 5.7a shows that with $M^* = 3$ and $U^* = 15$, the phase difference $\Delta\phi$ undergoes a steeper evolution with varying d at $\alpha = 0$. Under the effect of piezoelectric coupling, characterised by $\alpha = 0.3$, the evolution of $\Delta\phi$ with d is altered, and remains at a value close to $-\pi$, which is not favoured by the normal connection used in this case. Meanwhile, at $\Delta\phi = 0$, a peak of η is found, confirming that $\Delta\phi = 0$ indeed enhances energy harvesting with the normal connection.

From Fig. 5.6, where different values of α are tested, we can see that with larger α, the piezoelectric effect seemingly takes control of $\Delta\phi$ at smaller d. It is therefore interesting to determine a characteristic distance d_c above which the piezoelectric effect becomes dominant compared to the hydrodynamic forcing.

Scaling law between the hydrodynamic and piezoelectric forcing

The piezoelectric effect, represented in its dimensional form by an added torque $\mathcal{M}_{\text{piezo}}$ on each flag's trailing edge, is scaled as:

$$\mathcal{M}_{\text{piezo}} \sim \chi[V] \sim \frac{\chi^2[\theta]}{\mathcal{C}}, \tag{5.18}$$

where $[\theta]$ is the scale of leading edge angle. With the parameters studied in the present work, we have $[\theta] \sim \mathcal{O}(1)$. The fluid forcing on one flag due to the motion

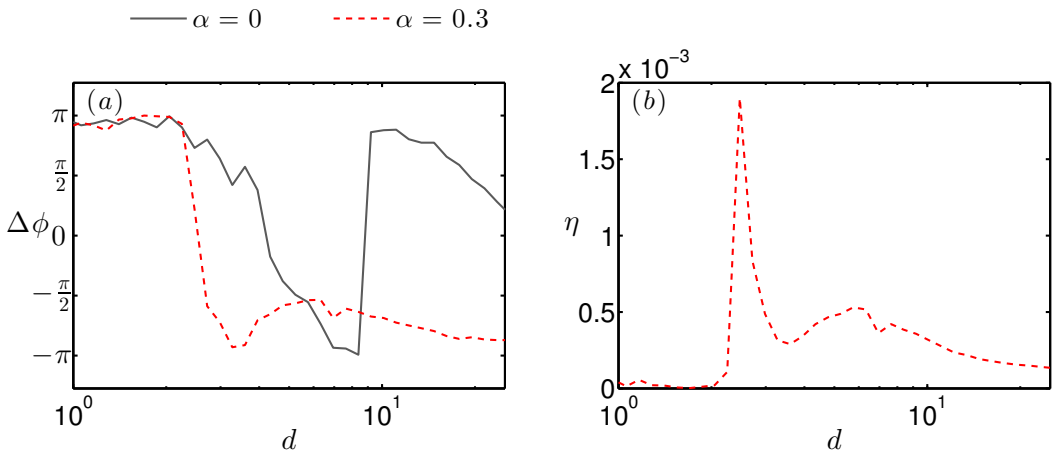

Figure 5.7: (a) Phase shift $\Delta\phi$ and (b) harvesting efficiency η as function of distance d for $\alpha = 0$ and $\alpha = 0.3$ using normal connection. Other parameters are $M^* = 3$, $U^* = 15$, $\beta = 0.15$.

of the other flag, noted as $\mathcal{M}_{\text{fluid}}$, is scaled as:

$$\mathcal{M}_{\text{fluid}} \sim \rho_f^s [u]^2 L^2, \tag{5.19}$$

where $[u]$ is the scale of velocity perturbation due to the other flag, which is scaled as, according to the Biot-Savart kernel given by Eq. (5.12):

$$[u] \sim U_\infty \frac{L}{D}. \tag{5.20}$$

Therefore, Eq. (5.19) becomes:

$$\mathcal{M}_{\text{fluid}} \sim \rho_f^s L^2 U_\infty^2 \frac{L^2}{D^2}. \tag{5.21}$$

The relative importance between $\mathcal{M}_{\text{piezo}}$ and $\mathcal{M}_{\text{fluid}}$ is given by their ratio:

$$\frac{\mathcal{M}_{\text{piezo}}}{\mathcal{M}_{\text{fluid}}} \sim \frac{\chi^2[\theta]}{\rho_f^s L^2 U_\infty^2 \mathcal{C}} \left(\frac{D}{L}\right)^2 \sim \left(\frac{d}{d_c^*}\right)^2. \tag{5.22}$$

Equation (5.22) shows that the ratio of $\mathcal{M}_{\text{piezo}}$ and $\mathcal{M}_{\text{fluid}}$ is proportional to the square of the ratio between the dimensionless distance d, and a dimensionless critical distance d_c^*, given by:

$$d_c^{*2} = \frac{\rho_f^s L^2 U_\infty^2 \mathcal{C}}{\chi^2[\theta]} = U_\infty^2 L^2 \frac{\mu}{B} \frac{\rho_f^s L}{\mu} \frac{B\mathcal{C}}{\chi^2[\theta]}. \tag{5.23}$$

When $\mathcal{M}_{\text{piezo}}$ and $\mathcal{M}_{\text{fluid}}$ are of the same order of magnitude, one has $d \sim d_c^*$. When $d < d_c^*$, the hydrodynamic forcing remains dominant and controls the evolution of $\Delta\phi$. When $d > d_c^*$, the fluid forcing becomes less important and is eventually

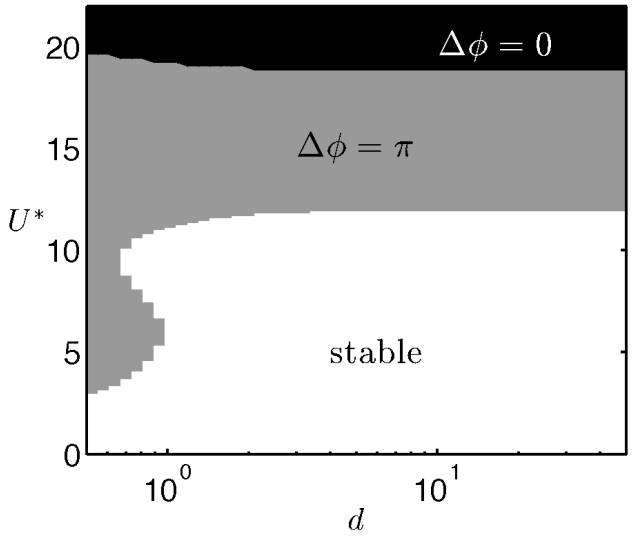

Figure 5.8: Phase shift $\Delta\phi$ of the most unstable mode as a function of d and U^*, for two side-by-side flags with $M^* = 3$ and $\alpha = 0$.

subdued by the piezoelectric forcing. In Eq. (5.23), one may recognise the definitions of α, M^*, and U^* from the above relation. We therefore obtain:

$$d_c^* = \frac{U^*}{\alpha}\sqrt{\frac{M^*}{[\theta]}}. \tag{5.24}$$

Equation (5.24) implies that d_c^* is proportional to α^{-1}, suggesting that under a stronger piezoelectric coupling, the piezoelectric forcing takes control of the system over the fluid forcing at a smaller distance.

Linear analysis

To confirm the relation $d_c^* \sim \alpha^{-1}$, we use the method proposed in [Alben 2008b] to convert the governing equations into a nonlinear eigenvalue problem (see Appendix C). Solving this eigenvalue problem allows us to obtain the phase difference of the most unstable mode with a given set of parameters.

Without piezoelectric coupling ($\alpha = 0$), we show in Fig. 5.8 the phase shift $\Delta\phi$ of the most unstable mode for $M^* = 3$, while varying U^* and d. For every tested value of d, above the critical velocity, we observe a phase shift of $\Delta\phi = \pi$, which is switched to $\Delta\phi = 0$ at a higher velocity ($U^* > 20$) without showing continuous evolution with either U^* or d. Unlike the results of nonlinear simulations, the fact that the linear analysis gives only $\Delta\phi = \pi$ or $\Delta\phi = 0$ is a necessary consequence due to symmetry reasons which are well explained in [Michelin 2009].

The next step is to choose several values of U^* corresponding to $\Delta\phi = \pi$, and then to observe the variation of $\Delta\phi$ with different values of d, and varying piezoelectric coupling, characterised by α. Figure 5.9 shows $\Delta\phi$ of the most unstable

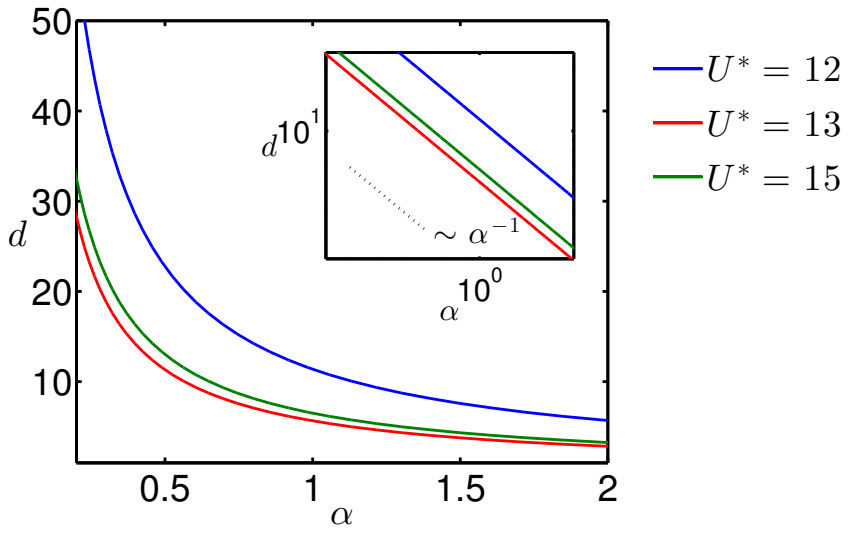

Figure 5.9: Phase shift of the most unstable coupled mode obtained from linear analysis as function of α and d with $U^* = 12$, $U^* = 13$, $U^* = 15$, using normal connection, and $M^* = 3$. For each U^*, phase shift is $\Delta\phi = \pi$ below the corresponding curve, and $\Delta\phi = 0$ above the curve. The inset shows the same quantities in logarithmic scale.

mode as function of α and d, with $\beta = 0.15$ and 3 different values of flow velocity: $U^* = 12$, $U^* = 13$, and $U^* = 15$.

We observe that for each value of U^*, the phase shift $\Delta\phi$, which is π for $\alpha = 0$, switches from π to 0 at a certain distance. A relation indeed exists between α and the value of d above which the switch of phase difference happens. As shown in the inset of Fig. 5.9, for all values of U^*, this relation is scaled as $d \sim \alpha^{-1}$, showing good agreement with Eq. (5.24). One will therefore ask whether in nonlinear simulations, same results would be obtained.

Comparison between linear and nonlinear results

As we observed previously that in nonlinear simulations, $\Delta\phi$ does not switch between π and 0 but evolves continuously between $-\pi$ and π, it is therefore necessary to define a criterion in terms of $\Delta\phi$ to illustrate the influence of piezoelectric effect. This criterion is chosen as $\Delta\phi_c = 1$. For fixed values of M^* and U^*, nonlinear simulations are performed by varying α and d. For each value of α, we identify the first value of d for which $\Delta\phi < \Delta\phi_c$ as the critical distance d_c above which the piezoelectric effect will take control over the hydrodynamic effect.

We plot the critical distance d_c as a function of α obtained from nonlinear numerical simulation in Fig. 5.10. The relation $d_c^* \sim \alpha^{-1}$ is also plotted in the same figure for comparison. We observe first that with increasing α, the critical distance d_c decreases. It shows that a stronger piezoelectric coupling indeed shows effect at a smaller distance. However, the evolution of d_c with α does not follow $d_c^* \sim \alpha^{-1}$.

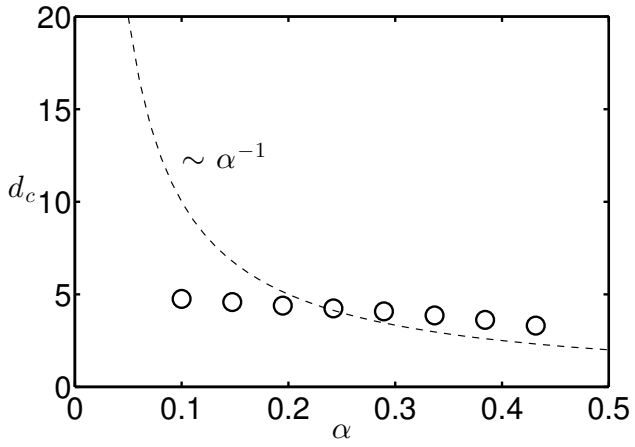

Figure 5.10: (◯) Nonlinear results of critical distance d_c for $\Delta\phi = 1$ as a function of α. Other parameters are $M^* = 3$, $U^* = 13$. Comparison between nonlinear results and (curve) the relation $d_c \sim \alpha^{-1}$.

This discrepancy would also be a result of complexity of the nonlinear simulations. While the origin of this discrepancy remains an open question, a possible explanation might reside in the large deformation of both flags in the nonlinear regime. Such a large deformation is not taken into account in the linear analysis, where only small vertical displacements are considered.

5.3.2.1 Inverse connection

In this section, we present briefly the results obtained using the inverse connection. We mentioned that since the inverse connection reverses the piezoelectric effects, the results obtained using this connection are expected to be somehow “inverse" compared with the normal connection.

In Fig. 5.11, we plot the phase difference $\Delta\phi$ (Fig. 5.11*a*) and the energy harvesting efficiency η (Fig. 5.11*b*) using the inverse connection for different values of α. The observations indeed suggest that the inverse connection leads to the opposite results with the normal connection. At small d, where the hydrodynamic effect still dominates, the in-phase flapping leads to low harvesting efficiency, while the out-of-phase flapping leads to high harvesting efficiency. With increasing d and a weakening hydrodynamic effect, the piezoelectric effect's impact becomes visible on the phase shift, which stops following the evolution of $\Delta\phi$ obtained with $\alpha = 0$ and stays close to $\Delta\phi = \pi$, the flapping pattern favoured by the inverse connection. Meanwhile, with larger α, the piezoelectric effect takes control of $\Delta\phi$ at smaller d.

5.3.2.2 Summary on resistive circuits

We investigated the energy-harvesting performance of two side-by-side flags whose electrodes are connected to one resistive circuit. While the normal connection tends

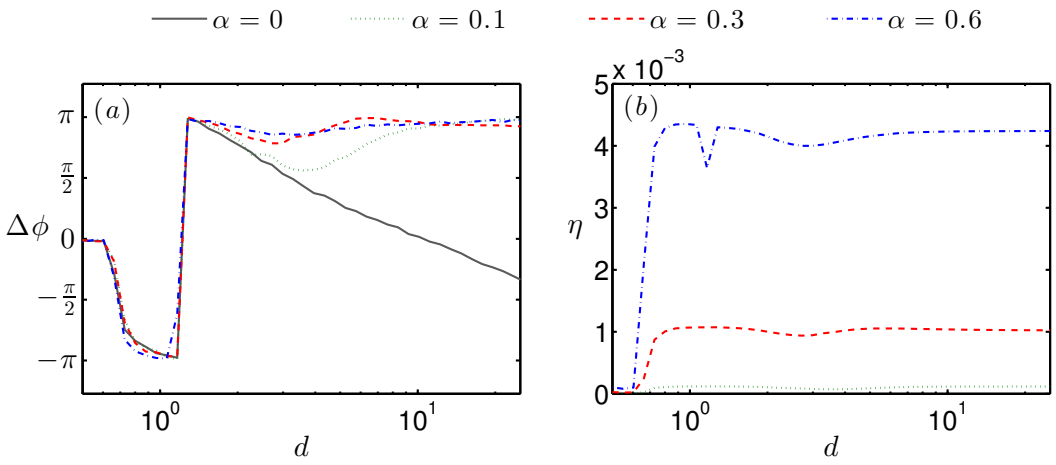

Figure 5.11: (a) Phase shift $\Delta\phi$ and (b) harvesting efficiency η as function of distance d, for $\alpha = 0$, $\alpha = 0.1$, $\alpha = 0.3$, and $\alpha = 0.6$, using the inverse connection. Other parameters are $M^* = 3$, $U^* = 13$, $\beta = 0.15$.

to impose an in-phase flapping of two flags, the inverse connection tends to favour an out-of-phase one. However, when the distance separating two flags is small, the action of both connections is observed to be too weak to have an observable influence on the flapping pattern. The phase difference $\Delta\phi$ is therefore still controlled by the hydrodynamic effect that impacts critically the energy harvesting. With increasing d, as indicated by Eq. (5.22), the hydrodynamic effect is weakened and is eventually prevailed by the piezoelectric effect, which starts to impose a visible impact on the phase shift $\Delta\phi$ so that the latter would be sometimes beneficial to the energy harvesting. However, the piezoelectric effect reveals itself only at large distance, otherwise, a potent coupling coefficient is necessary. Our results also suggest that at small d where hydrodynamic effect is still strong, one has to adapt the connection to the flapping pattern in order to maintain a satisfactory energy-harvesting performance.

5.3.3 Resistive-inductive circuits

A perspective of the work on the purely resistive circuits is to add inductance in the circuit. As seen in previous chapters, the inductance introduces resonant properties to the circuit, and is capable of strengthening the piezoelectric effects. In this section, the resistive-inductive circuits will be studied. The results obtained using both normal and inverse connections will be presented.

A resistive-inductive circuit introduces a natural frequency ω_c to the circuit, which is given by:

$$\omega_c = \frac{\omega_0}{\sqrt{2}}, \tag{5.25}$$

as two flags are connected in the same circuit, resulting to twice the intrinsic capaci-

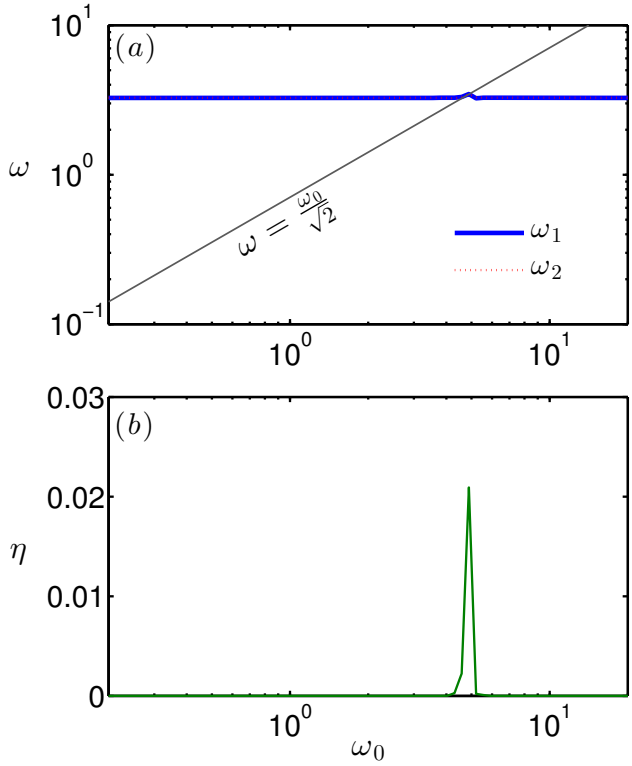

Figure 5.12: (a) Flapping frequency ω and (b) harvesting efficiency η with the normal connection, $d = 1.5$, $\alpha = 0.3$, $M^* = 3$, $U^* = 13$, $\beta = 10$

tance. Since in previous chapters, we have already identified improvement of energy harvesting by resonance, it would be reasonable to start by observing the effect of resonance on two flags.

In Fig. 5.12, we plot the evolution of flapping frequency of both flags, ω_1, ω_2 (Fig. 5.12a) and the energy harvesting efficiency η (Fig. 5.12b). Unsurprisingly, figure 5.12 shows that when the flapping frequency matches the circuit's natural frequency (Fig. 5.12a), the energy harvesting efficiency η reaches its peak value, an expected consequence of resonance (Fig. 5.12b). However, for the set of parameters used in Fig. 5.12, $d = 1.5$ should correspond to an out-of-phase flapping when $\alpha = 0$ (Fig. 5.4b), which is not favoured by the normal connection used here, and should diminish the energy harvesting. In this sense, such a high efficiency is also somehow an unexpected result.

The explanation to the seemingly unexpected high efficiency observed in Fig. 5.12 can be found by studying the flapping motion at resonance. The motion of flags in resonance with the resistive-inductive circuit are plotted in Fig. 5.13b, c, respectively for the normal connection and the inverse connection. These two cases are in comparison with the motion at $\alpha = 0$, plotted in Fig. 5.13a. In Fig. 5.13b, we can see that instead of being out-of-phase as in Fig. 5.13a, where $\alpha = 0$, the flapping motion is in-phase, a state favoured by the normal connection, leading to high

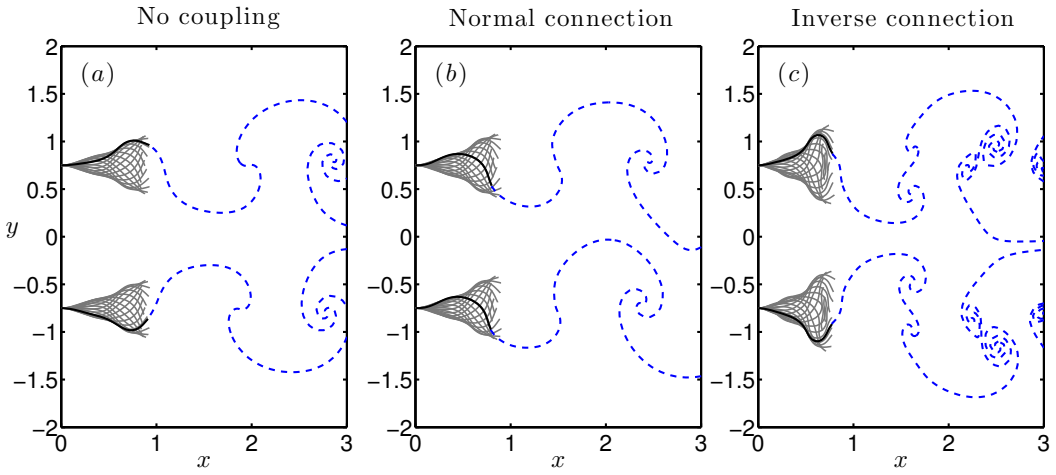

Figure 5.13: Flapping motion of two flags with $d = 1.5$, $M^* = 3$, $U^* = 13$ and (a) $\alpha = 0$, (b) $\alpha = 0.3$, $\beta = 10$, $\omega_0 = 4.88$, normal connection at resonance, $\eta = 0.011$, and (c) $\alpha = 0.3$, $\beta = 10$, $\omega_0 = 4.88$, inverse connection at resonance, $\eta = 0.029$.

harvesting efficiency. By adding an inductance, the circuit is capable of altering the flapping pattern to the one that is favoured by the given connection. The inductance therefore reinforces the piezoelectric effect so that it could apply a strong impact on the flapping pattern even at a small distance, where a resistive circuit is unable to manifest a visible impact. Moreover, as shown in Fig. 5.13*c*, if the connection is already the one in favour of the flapping pattern, two flags will keep flapping that way but with a much higher amplitude at resonance (Fig. 5.13), leading to a higher efficiency ($\eta = 0.029$).

The strengthened piezoelectric effect is effectively maintained at larger distances, as shown in Fig. 5.14. At such distances, the flapping pattern is always controlled by the piezoelectric effect, leading to $\Delta\phi = 0$ for the normal connection (Fig. 5.15). As a result, the favoured flapping pattern is reinforced by the resonance, leading to an increased harvesting efficiency and a large flapping amplitude.

5.4 Flags in tandem

Two flags placed in tandem are more sensitive to the hydrodynamic effect, as the trailing flag is permanently forced by the leading flag's wake. In this section, we will study whether the energy harvesting would be efficient under such strong hydrodynamic forcing. In particular, we are going to investigate whether the piezoelectric effect would still be able to prevail over the hydrodynamic effect. And if yes, under what condition the piezoelectric effect prevails and what influence it might have on the energy harvesting. In this part, we will study exclusively the normal connection.

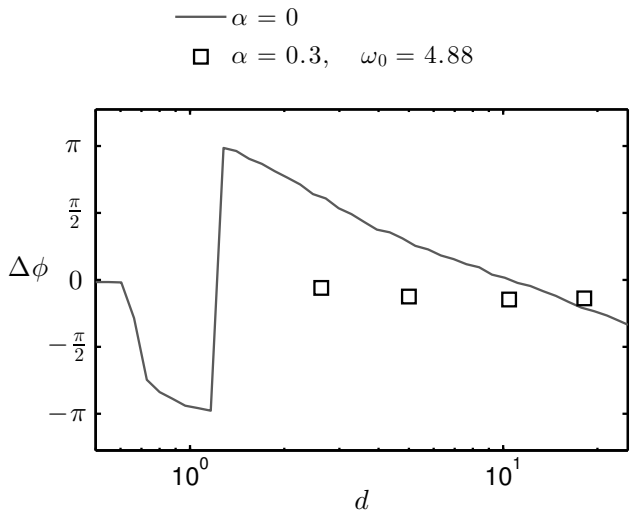

Figure 5.14: Phase shift $\Delta\phi$ as function of distance d using resistive-inductive circuit at resonance, with $M^* = 3$, $U^* = 15$, $\beta = 10$, and $\omega_0 = 4.88$, using the normal connection.

5.4.1 Resistive circuit

We start by using the resistive circuit. The phase shift $\Delta\phi$ and the energy harvesting efficiency η as functions of d are plotted in Fig. 5.16. The results presented in Fig. 5.16 show that under the action of a resistive circuit with $\alpha = 0.3$, the evolution of the phase difference $\Delta\phi$ with d is identical to that in the case of $\alpha = 0$ (Fig. 5.16*a*), while the peaks of η are observed only when $\Delta\phi = 0$ (Fig. 5.16*b*), favoured by the normal connection. This observation suggests that with the resistive circuit, the flapping pattern is primarily controlled by the hydrodynamic effect, and the harvesting efficiency η is increased only when the flapping pattern is favoured by the connection.

5.4.2 Resistive-inductive circuit

Next, we turn to the resistive-inductive circuit, which, in the side-by-side case, enhanced the piezoelectric effect so that it prevails against the hydrodynamic effect even at small d. The phase shift $\Delta\phi$ and the energy harvesting efficiency η obtained with the resistive-inductive circuit are plotted in Fig. 5.17. From Fig. 5.17*a*, we observe that the phase shift is slightly deviated from, but in general still follows the evolution of $\Delta\phi$ in the case of $\alpha = 0$. The harvesting efficiency η shows a similar evolution with the case of purely resistive circuit: despite its significant increase due to the resonance, this improvement happens only at values of d corresponding to $\Delta\phi = 0$. This result suggests that with two flags in tandem, the hydrodynamic effect still plays a dominant role and dictates the evolution of $\Delta\phi$, thereby that of η with d.

However, when the resonance occurs at $\Delta\phi = 0$, the piezoelectric effect is capa-

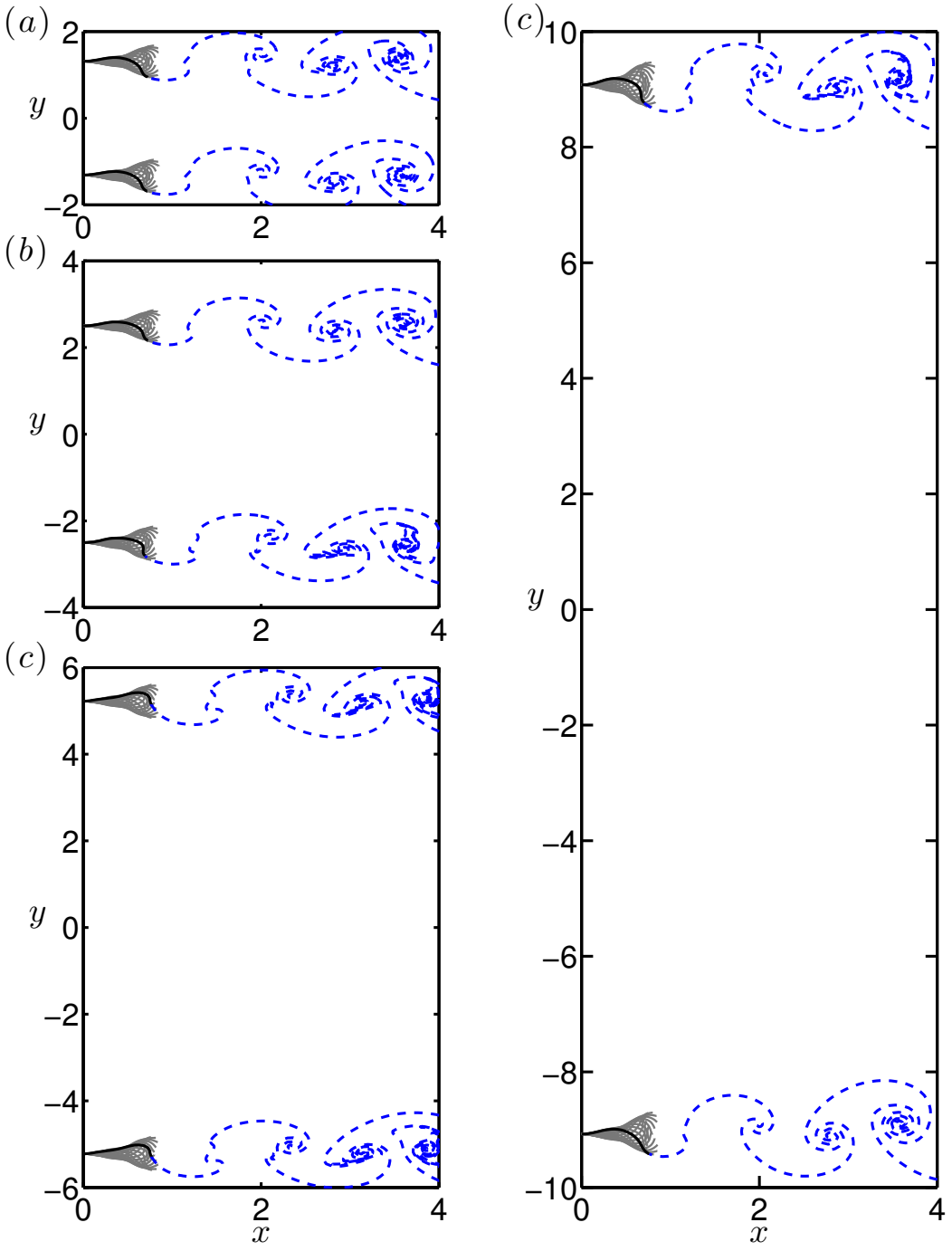

Figure 5.15: Flapping motion of two flags using resistive-inductive circuit, using the normal connection $\alpha = 0.3$, $M^* = 3$, $U^* = 13$, $\beta = 0.15$ and (a): $d = 2.6$, $\eta = 0.018$, (b): $d = 5$, $\eta = 0.018$, (c): $d = 10$, $\eta = 0.017$, and (d): $d = 18$, $\eta = 0.017$.

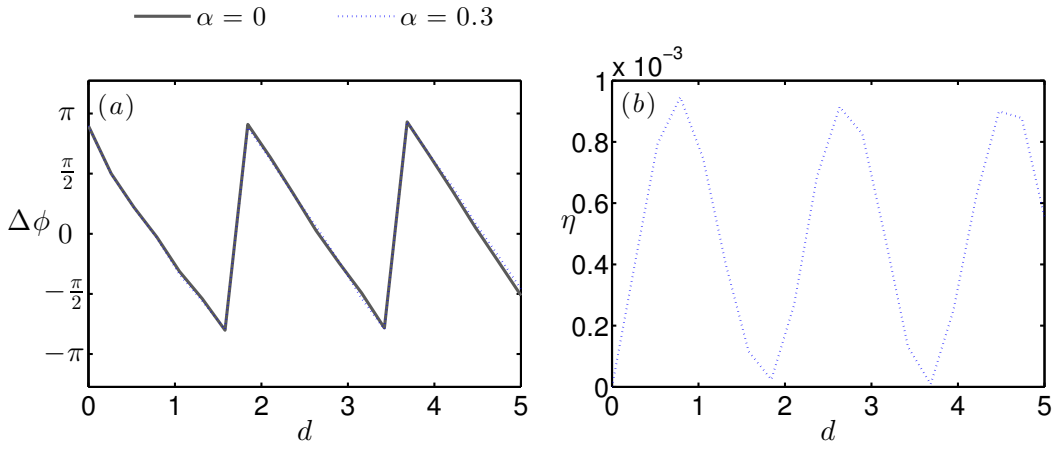

Figure 5.16: (a) Phase shift $\Delta\phi$ and (b) harvesting efficiency η as function of distance d of two flags on tandem using purely resistive circuit and the normal connection, with $\alpha = 0$ and $\alpha = 0.3$. Other parameters are $M^* = 3$, $U^* = 13$, $\beta = 0.15$.

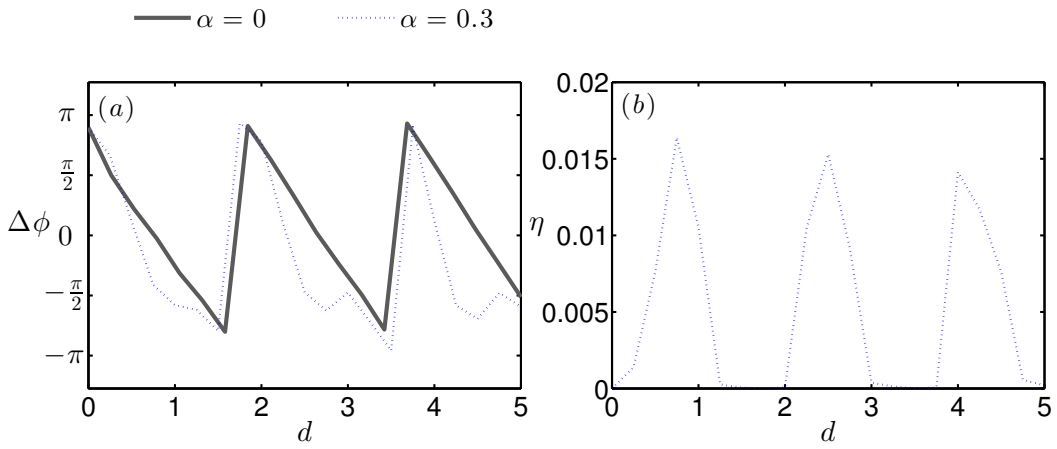

Figure 5.17: (a) Phase shift $\Delta\phi$ and (b) harvesting efficiency η as function of distance d of two flags in tandem using resistive-inductive circuit and the normal connection, with $\alpha = 0$ and $\alpha = 0.3$. Other parameters are $M^* = 3$, $U^* = 13$, $\beta = 10$, and $\omega = 4.88$ (resonance)

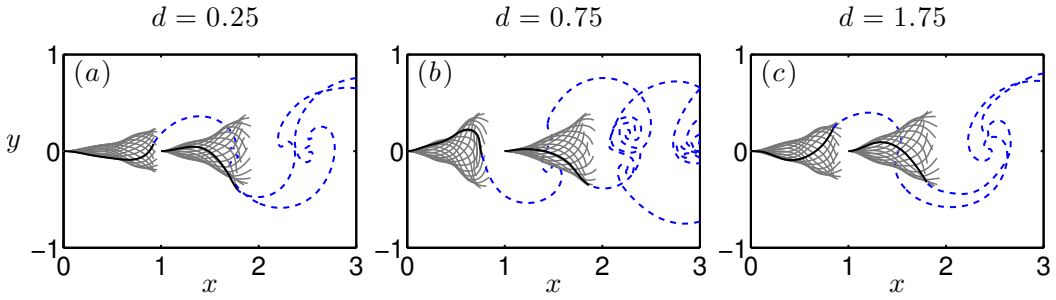

Figure 5.18: Flapping motion of two flags on tandem using resistive-inductive circuit and the normal connection, with $\alpha = 0.3$, $M^* = 3$, $U^* = 13$, $\omega_0 = 4.88$ and (a): $d = 0.25$, $\eta = 0.0014$, (b): $d = 0.75$, $\eta = 0.017$, (c): $d = 1.75$, $\eta \sim 10^{-6}$.

ble of exhibiting a stronger impact that overshadows the hydrodynamic effect on the flapping pattern, which is different to that determined solely by the hydrodynamic effect. In Fig. 5.18, we plot the flapping motion of two flags at three values of d, corresponding to $\Delta\phi \neq 0$ (Fig. 5.18a, c), and $\Delta\phi = 0$ (Fig. 5.18b). When d corresponds to a value of $\Delta\phi$ close to 0 (Fig. 5.18b), in addition to a high harvesting efficiency, we also observe that the leading flag has a slightly larger amplitude than the trailing flag, which is the opposite to the existing results of two flags placed in tandem [Ristroph 2008, Alben 2009b]. This observation suggests that the hydrodynamic effect which reduces the leading flag's amplitude is subdued by the piezoelectric effect enhanced by resonance. Meanwhile, the trailing flag shows no larger amplitude, suggesting that it's motion is dominated by a hydrodynamic forcing stronger than the effect of resonance. When $\Delta\phi$ is far from 0 (Fig. 5.18a, c) the flapping motion corresponds to the classically reported version: the leading flag has a smaller amplitude compared to the trailing flag. The hydrodynamic effect disrupts the resonance, leading to low harvesting efficiency.

5.5 Conclusion and perspectives

In this chapter, we investigated the coupled flutter and its effects on energy harvesting. We considered that the two flags' electrodes are connected to the same harvesting circuit, therefore in addition of the hydrodynamic coupling, an electrical coupling via the piezoelectric effects is added between them.

Both resistive circuits and resistive-inductive circuits are investigated, with flags both placed side by side and in tandem. With flags placed side-by-side, impacts issued from the piezoelectric effects are found on the flapping pattern: with resistive circuits, the flapping pattern is altered by the piezoelectric effect when two flags are sufficiently distant from each other. However, this change in the flapping pattern does not necessarily act in favour to the energy harvesting. When inductance is added, the piezoelectric effect is significantly strengthened when the flags and the

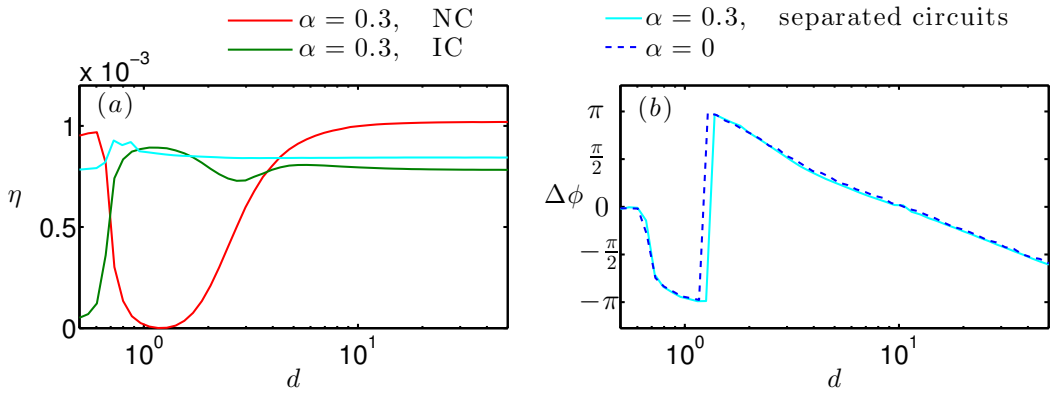

Figure 5.19: (*a*) Harvesting efficiency η with two side-by-side flags and $M^* = 3$, $U^* = 13$ and $\alpha = 0.3$, using both normal and inverse connections, and two separated circuits connected to each flag. (*b*) Phase shift $\Delta\phi$ as function of d for $\alpha = 0$ and $\alpha = 0.3$ with two separated circuits connected to each flag. Purely resistive circuit is used and $\beta = 0.15$.

circuit are at resonance. The reinforced piezoelectric effect is able to reverse the flapping pattern into the one favourable to the energy harvesting. However, the piezoelectric effects on the flags' flapping are almost unremarkable if the two flags are placed in tandem. The flags' flapping pattern is primarily dictated by the hydrodynamic effect, which overshadows the electrical coupling generated by both resistive and inductive circuits.

Compared with the configuration proposed in [Song 2014], i.e. two flags electrically independent, we believe that our results showed a new perspective by connecting two flags' electrodes in the same circuit. In Fig. 5.19, we provide a comparison between the energy-harvesting performance obtained using both normal and inverse connections, as well as a third configuration where two flags' electrodes are connected to separated circuits. Both the energy harvesting efficiency and phase difference are plotted. In terms of η (Fig. 5.19*a*), it is clear that when the chosen connection is favourable to a phase difference, and when d is sufficiently large so that $\Delta\phi$ is controlled by the piezoelectric effects, two flags connected in the same circuit deliver an output comparable with the sum of two flags connected in separated circuits. While two electrically independent flags would be useful to power two different devices, the advantage of the configuration studied in the present work, i.e. the summed and synchronised output, over the one in [Song 2014] makes it conceivable to design energy-harvesting systems based on the "two-flags-in-one-circuit" configuration that is capable to fuel devices which are too energy-consuming for one single piezoelectric flag.

Between the side-by-side and tandem configurations, we observed that the tandem configuration is more sensitive to the hydrodynamic effect, even at relatively large distances ($d \sim 5$) with inductive circuits, while in the side-by-side config-

uration, such distances are already sufficiently large to enable a flapping pattern controlled by piezoelectric effect. In reality, as it evolves downstream, the wake of the leading flag would surely be dissipated by viscosity so that it would not be "felt" by the following flag at large distances. In such case, one might expect the flapping pattern to be controlled by the piezoelectric effect. However, the effects that could have been brought by the hydrodynamic coupling, such as large amplitude of the trailing edge, which is beneficial to the energy harvesting, would have gone also with the dissipated wake, and the "tandem" configuration becomes equivalent to the side-by-side configuration at very large distances. We therefore believe that it is preferable, in terms of the ability of controlling flapping pattern, to opt for the side-by-side configuration, as it is less sensitive to hydrodynamic effects, and therefore is more likely to produce a synchronised output.

It would be however regrettable that the large amplitude of the trailing flag in the tandem configuration could not be exploited. One may envision, for the tandem configuration, a "feedback" device that adjust the distance between the two flags so that they flap in phase while the trailing flag would take profit from the leading flag's wake and produces a large amplitude. In addition, output-synchronising techniques through interfacing circuits are also interesting perspectives for harvesting energy with two unsynchronised flags, in both side-by-side and tandem case [Chen 2015].

Further works on this subject can be developed through the following paths:

- A thorough assessment of the influence of the coupling coefficient α. In our work with the side-by-side configuration, we have already identified its influence on the critical distance d_c above which piezoelectric effect starts to impact significantly on the phase shift $\Delta\phi$. However, there are other issues associated with α that are not addressed in our work. For instance, in Fig. 5.6, it can already be seen that two different values of α lead to different $\Delta\phi$ when d is very large. And in Fig. 5.7, the value of $\Delta\phi$ at very large d is not close to 0, which might also be a consequence of α. It is therefore necessary to study the role of α in the value of $\Delta\phi$ at very large distances.

- In terms of numerical methods used for nonlinear simulations, it would be of great interest to develop other models that is capable of accounting for a finite span, which is closer to the real life situation. In [Candelier 2013], Candelier proposed a variation of Lighthill's LAEBT that is compatible with a non-uniform flow. Inspired by this work, Jérôme Mougel & Sébastien Michelin in LadHyX have been working on an new method based on LAEBT to simulate the flapping of two side-by-side flags. Other works using alternative methods, such as ALE [Gurugubelli 2014], may also provide new insights on this aspect.

Chapter 6

Conclusion and perspectives

6.1 Conclusion

The goal of this dissertation is to identify the impact of different factors involved in a energy-harvesting mechanism based on piezoelectric flags. More precisely, three major factors impacting critically the energy-harvesting performance of piezoelectric flags are identified: the impact of circuits used for harvesting energy from piezoelectricity, the piezoelectric material used for fabricating the flag, and the impact of other flags in the same flow.

Firstly, a circuit containing a resistor and an inductor is chosen and the sensitivity of the coupled fluid-solid-electric system to the circuit's properties is investigated. In Chapter 2, experiments are performed to show that the resonant property of the inductive-resistive circuit indeed enhances the energy-harvesting performance: in the experiments, resonant circuits allow to harvest twice as much the energy as with a purely resistive circuit. Also, differences brought by the choice of materials are identified. The understanding of these two aspects is deepened through numerical studies conducted in Chapters 3 and 4. In these two chapters, a frequency lock-in mechanism is identified, using two different types of circuits. This lock-in phenomenon is able to considerably improve a piezoelectric flag's energy-harvesting efficiency. The common ingredient of these two types of circuits is still their resonant property, which is the underlying key factor of the improvement in energy harvesting associated with these two types of circuits. Besides, this frequency lock-in phenomenon is equally determined by the choice of materials, characterised by the coupling coefficient α: a more potent material, capable of offering a larger α, would allow a larger range of lock-in, as well as a higher harvesting efficiency.

In Chapter 5, the influence of the presence of an additional piezoelectric flag, both in the flow and in the circuit, on the energy harvesting is studied. The importance of flapping pattern to the energy harvesting is identified: the flapping pattern, characterised by the phase shift between two flags, could be constructive and destructive to the energy harvesting. Connecting the electrodes of the two flags in the same circuit tends to alter the phase shift in the way that the latter would be always favourable to the energy harvesting.

Based on the results of the present work, one may draw the following conclusion: **Using resonant circuits, the performance of energy-harvesting piezoelectric flags can be considerably improved through the piezoelectric effects enhanced by resonance.**

This conclusion is substantiated by the following observations:

6.1.1 Frequency lock-in

The essential reason of the frequency lock-in observed in the present work is the use of resonant circuits. Through resonance, the circuit produces large voltage, thereby enhancing the inverse piezoelectric effect and controlling the flag's dynamics.

By using local circuits presented in Chapter 3, the numerical study showed that thanks to the frequency lock-in, an efficiency of $\eta \sim 6\%$ is achieved with a flag covered by continuously distributed piezoelectric electrodes, and $\eta \sim 4\%$ with a flag covered by a single pair of electrodes. Note that these efficiencies are obtained only with $M^* = 1$, $U^* = 13$, and $\alpha = 0.3$, which are parameters that only lead to $\eta \sim 0.1\%$ with resistive circuits [Michelin 2013]. Based on the conclusion in [Michelin 2013] that larger M^* would lead to even higher efficiency, it is reasonable to expect even higher harvesting efficiency to be achieved through the frequency lock-in phenomenon by exploring a larger range of parameters.

A new perspective is opened by the observation of the frequency lock-in at multiple frequencies using non-local inductive networks. This result implies that with a given inductive network, characterised by its inductance ω_0, frequency lock-in may occur between the circuit and flags flapping at different frequencies. One can therefore expect that under certain flow conditions for which the flag's flapping frequency tends to vary greatly, this type of resonant network would be capable to adapt to the varying frequency, thereby maintaining the system to work at frequency lock-in and to yield a high efficiency.

6.1.2 Two flags' synchronisation through the fluid-solid-electric resonance

While more flags indeed imply a larger quantity of harvested energy, the real question is to synchronise and sum each flag's productivity. The results in Chapter 5 using two side-by-side flags showed that even when the distance separating the two flags is small, i.e. the hydrodynamic effect remains strong, connecting two flags' electrodes to a resonant circuit can successfully synchronise the motion of the two flags through the inverse piezoelectric effect enhanced by resonance. This resonance-induced synchronisation effectively incorporates the productivity of each flag, and yields a high efficiency.

6.2 Perspectives

The present dissertation constitutes a first step of investigating the potential of piezoelectric flags as an energy-harvesting mechanism. This work demonstrated a strong potential for such energy-harvesting concept, and clearly pointed out that a promising path of development is to consider the coupling of the piezoelectric flags with resonant circuits. Meanwhile, more work need to be done in order to fully exploit other aspects relating to piezoelectric flags. In addition to specific perspectives presented at the end of each chapter, several more general directions

towards which future work may advance are outlined here.

6.2.1 External forcing-induced vibration of piezoelectric flag

Large deformation of piezoelectric flag is always beneficial to the energy harvesting. Such large amplitude is achieved in our work through an instability, while other routes towards large amplitude are available. Another route leading to large amplitude vibration of flexible structures consist of making use of a bluff body's wake as a forcing to drive a structure. This idea is already proposed in [Allen 2001]. A piezoelectric membrane will oscillate under the action of the bluff body's wake and consequently converting mechanical deformation to electricity. With such concept, the piezoelectric membrane may oscillate even with a low flow velocity, without the need of triggering an instability. Further work on this subject may focus on a configuration involving more than one piezoelectric membranes and study the interaction of the bluff body's wake and that of the piezoelectric membranes, and the consequence on the energy harvesting.

6.2.2 Flags placed in other types of flows

In the present work, we studied piezoelectric flags placed in inviscid, incompressible uniform flows. It is therefore natural to imagine piezoelectric flags being used in other flows. An interesting example would be flows of the waste gas emitted by vehicle engines. Such flows are usually non-uniform and highly turbulent. It is therefore interesting to study how the turbulence impacts the energy harvesting using piezoelectric flags. In addition, the high temperature of these gas flows would provide additional challenges if one continues on this path.

Another domain where energy-harvesting piezoelectric flags would be applied is the biomedical applications. Some researchers proposed *in vivo* piezoelectric energy-harvesting systems to power other *in vivo* devices monitoring body functioning. The flows of the body fluid are highly viscous. It is therefore essential to understand the role of the viscosity on the energy harvesting.

6.2.3 Flags positioned in alternative configurations

Configurations with flags placed in a different manner than the one in our work are also interesting objects for future investigation. An example of alternative configurations is the inverted flag, i.e. a flag with a free leading edge but a fixed trailing edge. Dynamics of such flags have been recently studied [Kim 2013, Ryu 2015, Tang 2015] and research work on energy harvesting using such configuration is in its starting stage: with this configuration, a flag is able to flap, thereby converting energy into electrical form at a much lower flow velocity [Gurugubelli 2015]. The drawback of this configuration is that the flag would be more likely to show buckling when the flow velocity is too large [Kim 2013]. Additional efforts are therefore needed to advance on this subject. Meanwhile, the configuration consisting of placing a flag perpendicular to the incoming flow constitutes also an interesting option to study.

Appendices

Appendix A

Measurement of coupling coefficient of the PVDF flag

In this appendix, we explain the process employed to determine the coupling coefficient α, for the PVDF flag used in the experimental study (Chapter 2). The coupling coefficient is defined as:

$$\alpha = \frac{\chi}{\sqrt{Bc}}, \tag{A.1}$$

where χ, B and $c = \mathcal{C}/L$ are the mechanical/electrical conversion factor of PVDF, the bending rigidity and the linear density of the intrinsic capacitance of the piezoelectric pair, respectively. Among these quantities, c can be obtained directly by measuring the effective length L and the total capacitance $\mathcal{C}$ ($\mathcal{C}$ = 14 nF) of the flag. Note that since the entire flag, i.e. both the clamped part and the effective part, is connected in the circuit, the total intrinsic capacitance remains the same regardless of the effective length. The values of c obtained for different L are shown in Table A.1:

L (cm)	5	6	7	8
c (μF/m)	0.28	0.23	0.2	0.175

Table A.1: Measurements of linear density of intrinsic capacitance c with different values of effective length L.

The following text will therefore mainly focus on the determination of χ and B.

A.1 Measurement of B

The bending rigidity of a three-layer sandwich plate of width H is given by the following formula [Lee 1989]:

$$B = \frac{E_0 h_0^3 H}{12(1-\nu_0^2)} + \frac{2E_p h_p H}{1-\nu_p^2}\left(\frac{h_0^2}{4} + \frac{h_0 h_p}{2} + \frac{h_p^2}{3}\right), \tag{A.2}$$

where E are ν are respectively the Young's modulus and the Poisson's coefficient of corresponding material, h is the thickness of a layer. The subscripts 0 and p indicate the middle layer and the piezoelectric layers of the flag.

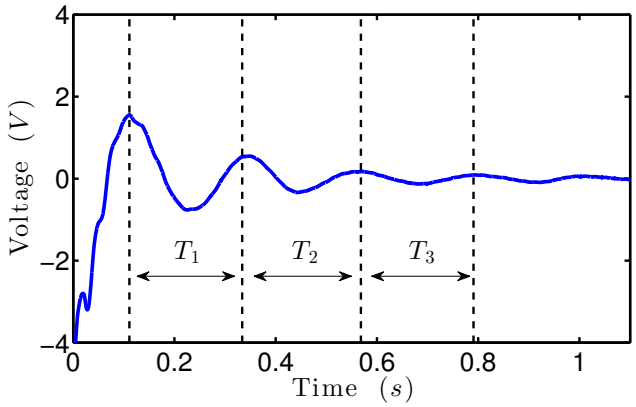

Figure A.1: Example of voltage signal obtained using flag with $L = 8$ cm.

Since it is difficult to determine the Young's modulus of the middle layer, which is made of a double-face adhesive strap, we opt an alternative way to determine B, which is based on the flag's first natural frequency, using the following equation [Timoshenko 1953]:

$$f_0 = \frac{3.515}{2\pi L^2}\sqrt{\frac{B}{\mu}}, \tag{A.3}$$

where μ is the mass per unit length of the flag.

To measure the natural frequency f_0, we choose the flags of two different lengths: $L = 7$ cm and 8 cm. The choice of the lengths is based on two considerations: on one hand, 8 cm is the maximal effective length that the piezoelectric flag could reach; on the other hand, for smaller values of length, the free vibration is too quickly damped out and we could not retrieve any usable vibration period.

Each flag is then connected to a data acquisition board (DAQ) so that the vibration-induced voltage signal would be recorded. For each test, we bend initially each flag by fixing one end and displacing the other. At $t = 0$, the displaced end is released and the flag undergoes a damped vibration, during which a voltage signal is generated and recorded, as shown in Fig. A.1.

For each flag, such test is performed several times and for each test. Two or three usable vibration periods are extracted from each test, and the average period is taken from 15 measurements, from which the natural frequency is deduced. In Table A.2, we show results obtained with two flags. The results show that it is reasonable to choose $B = 1.178 \times 10^{-5}$ N·m^2 for the rest of our work.

A.2 Measurement of χ and α

In Chapter 2, we showed that with a PVDF flag connected directly to the data acquisition board (DAQ), without any additional loading in the circuit, χ can be

Length (cm)	T (s)	f (Hz)	B $(N \cdot m^2)$
7	0.168±0.006	5.952±0.2	1.217×10^{-5}
8	0.227±0.005	4.405±0.1	1.137×10^{-5}

Table A.2: Measurement results and bending rigidity obtained with flags of length $L = 7$ cm and 8 cm.

Length (cm)	U_1 (m/s)	U_2 (m/s)	U_3 (m/s)	U_4 (m/s)
5	19.4	20.3	20.9	21.8
6	15.7	16.3	17.5	18.5
7	11.9	12.9	13.7	14.8
8	11.3	12.2	13.5	14.1

Table A.3: Length of each flag and flow velocity used in each test

computed using the following equation:

$$\chi = \frac{V_0}{\omega \Theta_0} \sqrt{\left(\frac{1}{\mathcal{R}_d^2} + \omega^2 C^2 \right)}, \tag{A.4}$$

with $\omega = 2\pi f$ is the flapping frequency in rad/s. V_0 and Θ_0 are respectively the amplitude of the voltage and the leading edge angle while flapping, and $\mathcal{R}_d$ is the internal resistance of the DAQ, which is fixed at $\mathcal{R}_d = 10^6 \Omega$.

We perform experiments using flags of four different lengths: $L = 5$ cm, 6 cm, 7 cm, and 8 cm. And for each flag, wind tunnel tests are performed with four different flow velocities listed in Table A.3. During each test, a high speed camera is used to record the flapping motion, and the DAQ is used to record the voltage signal. Both recordings are then used to extract f, Θ_0 and V_0 for each test, as shown in Fig. A.2.

The results obtained from measurement as well as calculation are shown in Tables A.4–A.7. The values of α corresponding to different effective length L are shown in Table A.8.

Velocity (cm/s)	f (Hz)	Θ_0 (degree)	Θ_0 (rad)	V_0 (V)	χ (C)	α
19.4	79.1	74.2	1.30	12.26	1.34×10^{-7}	0.074
20.3	81.1	91.5	1.60	13.21	1.17×10^{-7}	0.064
20.9	82.3	96.4	1.68	13.90	1.17×10^{-7}	0.064
21.8	86.3	100.1	1.75	14.78	1.19×10^{-7}	0.066

Table A.4: Experimental results and α obtained with $L = 5$ cm

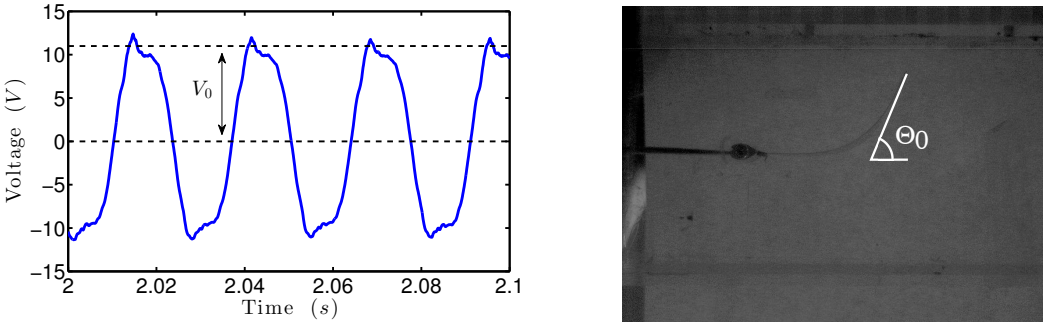

Figure A.2: Examples of measurement of (left) voltage and (right) angle for $L = 8$ cm and $U = 11.3$ m/s.

Velocity (cm/s)	f (Hz)	Θ_0 (degree)	Θ_0 (rad)	V_0 (V)	χ (C)	α
15.7	59.7	77.8	1.36	11.74	1.23×10^{-7}	0.074
16.3	61.5	81.1	1.42	13.09	1.32×10^{-7}	0.079
17.5	65.3	82.4	1.44	15.06	1.49×10^{-7}	0.090
18.5	69.4	86.8	1.51	16.44	1.54×10^{-7}	0.093

Table A.5: Experimental results and α obtained with $L = 6$ cm

Velocity (cm/s)	f (Hz)	Θ_0 (degree)	Θ_0 (rad)	V_0 (V)	χ (C)	α
11.9	43.6	72.5	1.27	10.18	1.16×10^{-7}	0.076
12.9	45.8	74.2	1.30	12.44	1.38×10^{-7}	0.090
13.7	48.8	79.4	1.39	14.34	1.49×10^{-7}	0.097
14.8	52.4	87.8	1.53	18.84	1.76×10^{-7}	0.115

Table A.6: Experimental results and α obtained with $L = 7$ cm

Velocity (cm/s)	f (Hz)	Θ_0 (degree)	Θ_0 (rad)	V_0 (V)	χ (C)	α
11.3	37.5	77.7	1.36	13.51	1.46×10^{-7}	0.101
12.2	40.5	84.7	1.48	14.92	1.47×10^{-7}	0.102
13.5	44.2	88.4	1.54	16.82	1.58×10^{-7}	0.110
14.1	45.5	90.0	1.57	17.19	1.58×10^{-7}	0.110

Table A.7: Experimental results and α obtained with $L = 8$ cm

L (cm)	5	6	7	8
α	0.067±0.006	0.084±0.01	0.094±0.02	0.106±0.004

Table A.8: Values of the coupling coefficient α corresponding to different values of effective length L.

Appendix B

Flexible body vortex sheet model

B.1 Governing equations

In this appendix, we will be interested in the vortex sheet model applied on one single flag. The extension to the situation of two flags is straightforward. Following the notations introduced in Chapter 5, C represents the contour of the vortex sheet, and $C = C_f + C_w$, with C_f representing the bound vortex sheet and C_w the free vortex sheet. The system of dimensionless equations to be solved is the following:

$$\tilde{\mathbf{u}}(s,t) = \mathbf{e}_x + \frac{1}{2\pi \mathrm{i}} \fint_{C_f} \frac{\gamma(s',t)}{\mathbf{x}(s,t) - \mathbf{x}(s',t)} \mathrm{d}s' + \frac{1}{2\pi \mathrm{i}} \int_{C_w} \frac{\gamma(s',t)}{\mathbf{x}(s,t) - \mathbf{x}(s',t)} \mathrm{d}s', \tag{B.1}$$

$$\frac{\partial \mathbf{x}}{\partial t} \cdot \mathbf{n} = \mathbf{u}(s,t) \cdot \mathbf{n}, \quad s \in C_f, \tag{B.2}$$

$$\mathbf{F}_{\text{fluid}} = [p](s,t)\mathbf{n} = \left(\int_0^s \frac{\partial \gamma}{\partial t} + [\mathbf{u}_r(s,t) \cdot \boldsymbol{\tau}] \gamma(s,t) \right) \mathbf{n}, \quad s \in C_f \tag{B.3}$$

$$\Gamma(s,t) = \int_{s_m}^{s} \gamma(s',t) \mathrm{d}s' = \Gamma(1,t_0) = \int_{C_f} \gamma(s',t_0) \mathrm{d}s', \quad s \in C_w. \tag{B.4}$$

$$\frac{\partial^2 \mathbf{x}}{\partial t^2} = \frac{\partial}{\partial s} \left[T\boldsymbol{\tau} - \frac{\partial \mathcal{M}}{\partial s} \mathbf{n} \right] + M^* \mathbf{F}_{\text{fluid}}, \tag{B.5}$$

with the clamped-free boundary conditions:

$$\text{at} \quad s = 0 : \ \mathbf{x} = \theta = 0, \tag{B.6}$$

$$\text{at} \quad s = 1 : \ T = \mathcal{M} = \frac{\partial \mathcal{M}}{\partial s} = 0. \tag{B.7}$$

Equation (B.1) computes the velocity of the vortex sheet by taking the limits of flow velocity above and below the vortex sheet, Eq. (B.2) is the impermeability condition applied on the flag, Eq. (B.3) computes the pressure jump on the flag, Eq. (B.4) is Kelvin's theorem for computing the circulation Γ of each material point on the free vortex sheet C_w, using the invariance of circulation, and Eq. (B.5) is the Euler-Bernoulli beam model with the clamped-free boundary conditions given by Eqs. (B.6) and (B.7).

Before introducing more details, we would like to mention that in the following text, we use complex numbers to represent 2D vectors. For example, the variable

$\hat{x} = x + \mathrm{i}y$ is the complex representation of vector $\mathbf{x}$, and $\tilde{x}$ would be its complex conjugate. The scalar product of two vectors $\hat{w}_1 = a + \mathrm{i}b$ and $\hat{w}_2 = c + \mathrm{i}d$ is given by the following relation:

$$\mathbf{w}_1 \cdot \mathbf{w}_2 = Re(\hat{w}_1 \tilde{w}_2), \tag{B.8}$$

which shall be extensively used in the forthcoming text.

Another prerequisite is about the dimensionless equations. In all Chapters of the present work, the length of the flag L is chosen as the characteristic length of the system, the flag being placed between 0 and L, the corresponding dimensionless coordinates is therefore $0 \leq s \leq 1$. However, in order to solve the Eqs. (B.1) and (B.2), it is necessary to extensively use the properties of Chebyshev polynomials, which are defined between -1 and 1. As a result, in this appendix, we exceptionally opt for another non-dimensionlisation, which is based on the half-length of the flag $L/2$, with the flag being placed between $-L/2$ and $L/2$. The dimensionless coordinate corresponding to the flag becomes $-1 \leq z \leq 1$. The results presented in Chapter 5 are converted from the half-length non-dimensionalisation through a rescaling.

Using the complex representation, and the new characteristic length $L/2$, we may rewrite Eq. (B.1)–(B.7) into the following form:

Average velocity of the vortex sheet

$$\tilde{u}(z,t) = 1 + \frac{1}{2\pi\mathrm{i}} \fint_{-1}^{1} \frac{\gamma(z',t)}{\hat{x} - \hat{x}(z',t)} \mathrm{d}z' + \frac{1}{2\pi\mathrm{i}} \fint_{1}^{z_{\max}} \frac{\gamma(z',t)}{\hat{x} - \hat{x}(z',t)} \mathrm{d}z', \quad z \in C \tag{B.9}$$

Impermeability condition

$$Re\left(\frac{\partial \hat{x}}{\partial t}\tilde{n}\right) = Re\left(\hat{u}(z,t)\tilde{n}\right), \quad z \in C_f, \tag{B.10}$$

Kelvin's theorem

$$\Gamma(z,t) = \int_{z_m}^{z} \gamma(z',t)\mathrm{d}z' = \Gamma(1,t_0) = -\int_{-1}^{1} \gamma(z',t_0)\mathrm{d}z', \quad z \in C_w. \tag{B.11}$$

Bernoulli's theorem for the pressure jump

$$[p](z,t) = \int_{-1}^{z} \frac{\partial \gamma}{\partial t} + \hat{u}_r(z,t)\gamma(z,t), \tag{B.12}$$

where $\hat{u}_r$, the average of the relative tangential fluid velocities on either sides of the flag is given by:

$$\hat{u}_r(z,t) = Re\left(\left(\hat{u} - \frac{\partial \hat{x}}{\partial t}\right)\tilde{\tau}\right). \tag{B.13}$$

Euler-Bernoulli Beam model

$$\frac{\partial^2 \hat{x}}{\partial t^2} = 2\frac{\partial T\hat{\tau}}{\partial z} - \frac{8}{U^{*2}}\frac{\partial}{\partial z}\left(\frac{\partial \kappa}{\partial z}\hat{n}\right) - \frac{1}{2}M^*[p]\hat{n} \tag{B.14}$$

with the clamped-free boundary conditions:

$$\text{at} \quad z = -1: \ \hat{x} = \theta = 0, \tag{B.15}$$

$$\text{at} \quad z = 1: \ T = \kappa = \frac{\partial \kappa}{\partial z} = 0. \tag{B.16}$$

In Eq. (B.14), $\kappa = \partial\theta/\partial z$ is the local curvature of the flag.

B.2 Calculation of the free vortex sheet

The second integral on the right-hand side of Eq. (B.9) can be re-parametrised using the invariance of Γ on the free vortex sheet. Using Eq. (B.11), we actually have:

$$\gamma(z,t)\mathrm{d}z = \mathrm{d}\Gamma, \quad z \in C_w \tag{B.17}$$

thus Eq. (B.9) is rewritten as:

$$\tilde{u}(z,t) = 1 + \frac{1}{2\pi \mathrm{i}}\fint_{-1}^{1} \frac{\gamma(z',t)}{\hat{x} - \hat{x}(z',t)}\mathrm{d}z' - \frac{1}{2\pi \mathrm{i}}\fint_{0}^{\Gamma_t(t)} \frac{\mathrm{d}\Gamma'}{\hat{x}(\Gamma,t) - \hat{x}(\Gamma',t)}, \tag{B.18}$$

where

$$\Gamma_t(t) = \int_{z_{\max}}^{1} \gamma(z',t)\mathrm{d}z' = -\int_{-1}^{1} \gamma(z',t)\mathrm{d}z' \tag{B.19}$$

is the total circulation of the free vortex sheet.

Another problem of this integral is that it is singular at $z = 1$. This singularity can be removed using a smoothing parameter δ [Krasny 1986]. Using this smoothing parameter, Eq. (B.18) becomes:

$$\tilde{u}(z,t) = 1 + \frac{1}{2\pi \mathrm{i}}\fint_{-1}^{1} \frac{\gamma(z',t)}{\hat{x} - \hat{x}(z',t)}\mathrm{d}z' - \frac{1}{2\pi \mathrm{i}}\int_{0}^{\Gamma_t(t)} \frac{\overline{\hat{x}(\Gamma,t) - \hat{x}(\Gamma',t)}}{|\hat{x}(\Gamma,t) - \hat{x}(\Gamma',t)|^2 + \delta^2}\mathrm{d}\Gamma'. \tag{B.20}$$

The value of the smoothing parameter is set to be $\delta = 0.2$ for the present work as used in [Alben 2008a]. In [Alben 2009a], Alben pointed out that this smoothing using a constant δ would introduce a discontinuity of γ at $z = 1$, as no such smoothing is used for the bound vortex sheet, and consequently impair the description of the details of the vortex shedding. The author proposed a tapered δ-smoothing [Alben 2009a, Alben 2010] consisting of setting δ as a function of z on the free vortex sheet: $\delta = 0$ at $z = 1$, and tends asymptotically to a constant value δ_0 with increasing s, thereby ensuring a smooth transition from the bound vortex sheet to the free vortex sheet at $z = 1$. This tapered smoothing is however not used in the present work as we focus mainly on the coupled flapping instead of the vortex shedding.

The evolution of the free vortex sheet is described by the Birkhoff-Rott equation [Saffman 1992], which states that the fluid particles in the free vortex sheet move with the mean velocity $\hat{u}$ given in Eq. (B.20). This equation is written as:

$$\frac{\partial \tilde{x}}{\partial t}(\Gamma,t) = 1 + \frac{1}{2\pi \mathrm{i}} \fint_{-1}^{1} \frac{\gamma(z',t)}{\hat{x}(\Gamma,t) - \hat{x}(z',t)} \mathrm{d}z' - \frac{1}{2\pi \mathrm{i}} \int_{0}^{\Gamma_t(t)} \frac{\overline{\hat{x}(\Gamma,t) - \hat{x}(\Gamma',t)}}{|\hat{x}(\Gamma,t) - \hat{x}(\Gamma',t)|^2 + \delta^2} \mathrm{d}\Gamma', \quad \hat{x}(\Gamma,t) \in C_f. \tag{B.21}$$

The circulation of every material point, except the one at $z = 1$, on the free vortex sheet is known since its circulation is computed at the moment when it is shed from $z = 1$ using Eq. (B.11). The next section will show the method to find the circulation of the material point at $z = 1$ as well as the strength γ of the bound vortex sheet C_f.

B.3 Calculation of the bound vortex sheet

In this section, we present the solution to all variable attached to the flag, i.e. the bound vortex sheet's strength γ and $\hat{x}$

The strength of the bound vortex sheet γ is computed using Eqs. (B.10) and (B.18), as well as the Kutta's condition imposing a finite flow velocity at $z = 1$. According to [Muskhelishvili 2008], the general solution of $\gamma(z,t)$ has inverse-square singularities at $z = \pm 1$. We therefore define $v(z,t)$, the bounded part of $\gamma(z,t)$, by:

$$\gamma(z,t) = \frac{v(z,t)}{\sqrt{1-z^2}}. \quad z \in C_f \tag{B.22}$$

Using $v(z,t)$, Eq. (B.10) is written as:

$$\begin{aligned} Re\left(\hat{n}\frac{\partial \tilde{x}}{\partial t}\right) = Re\Bigg(\hat{n}\Bigg(1 + \frac{1}{2\pi \mathrm{i}} \fint_{-1}^{1} \frac{v(z',t)}{\sqrt{1-z'^2}(\hat{x}(z,t) - \hat{x}(z',t))} \mathrm{d}z' \\ - \frac{1}{2\pi \mathrm{i}} \int_{0}^{\Gamma_t(t)} \frac{\overline{\hat{x}(z,t) - \hat{x}(\Gamma',t)}}{|\hat{x}(z,t) - \hat{x}(\Gamma',t)|^2 + \delta^2} \mathrm{d}\Gamma'\Bigg)\Bigg), \quad z \in C_f, \end{aligned} \tag{B.23}$$

and the Kutta's condition is:

$$v(1,t) = 0. \tag{B.24}$$

To find $v(z,t)$ from the integro-differential equation given by Eq. (B.23), we define a function f by:

$$\begin{aligned} f(z,t) = -Re\Bigg(\hat{n}\Bigg(1 - \frac{1}{2\pi \mathrm{i}} \int_{0}^{\Gamma_t(t)} \frac{\overline{\hat{x}(z,t) - \hat{x}(\Gamma',t)}}{|\hat{x}(z,t) - \hat{x}(\Gamma',t)|^2 + \delta^2} \mathrm{d}\Gamma' - \frac{\partial \tilde{x}}{\partial t} \\ + \frac{1}{2\pi \mathrm{i}} \left(\frac{\partial \hat{x}}{\partial z}\right)^{-1} \fint_{-1}^{1} K(z,z',t) \frac{v(z',t)}{\sqrt{1-z'^2}} \mathrm{d}z'\Bigg)\Bigg), \quad z \in C_f, \end{aligned} \tag{B.25}$$

where the term $K(z, z', t)$ is the regular part of the Cauchy-type kernel appeared in Eq. (B.23):

$$\frac{1}{\hat{x}(z,t) - \hat{x}(z',t)} = \left(\frac{\partial \hat{x}}{\partial z}\right)^{-1} \frac{1}{z - z'} + \left(\frac{\partial \hat{x}}{\partial z}\right)^{-1} K(z, z', t), \quad z \neq z', \quad z, z' \in C_f. \tag{B.26}$$

The value of $K(z, z', t)$ can be evaluated at singularity $z = z'$ by expanding $\hat{x}$ into Taylor series about $z = z'$:

$$K(z, z', t) = \mathrm{i}\frac{\kappa(z,t)}{2}, \quad z \in C_f \tag{B.27}$$

Using the function f and the Kelvin's theorem, we give the expression for $v(z, t)$ as the following one:

$$v(z,t) = 2\sum_{k=1}^{N} f_k(t) \sin\theta \sin k\theta - f_1(t) - 2f_0(t)z + \frac{\Gamma_t(t)}{\pi}, \tag{B.28}$$

and the expression of the Kutta's condition (Eq. (B.24)) as:

$$-f_1(t) - 2f_0(t) + \frac{\Gamma_t(t)}{\pi} = 0. \tag{B.29}$$

In Eqs. (B.28) and (B.29), f_i are the expansion of the function f on Chebyshev polynomials of the first kind [Mason 2002]:

$$f(z,t) = \sum_{k=0}^{N} f_k(t) T_k(z), \tag{B.30}$$

The last element necessary to evaluate the function f is the information of the flag's displacement, which can be obtained from Eq. (B.14). The flag's motion is computed based on the local curvature κ. We integrate κ once to recover θ, and twice to obtain $\hat{x}$, by considering the clamped-free boundary conditions:

$$\theta(z,t) = \int_{-1}^{z} \kappa(z',t)\mathrm{d}z', \quad \hat{x}(z,t) = \int_{-1}^{z} \mathrm{e}^{\mathrm{i}\theta(z',t)}\mathrm{d}z'. \tag{B.31}$$

If we replace $\hat{x}$ in Eq. (B.14) using Eq. (B.31), the curvature κ becomes the only unknown in Eq. (B.14).

Equations (B.28), (B.29), and (B.14) constitute a nonlinear system allowing us to obtain $v(z, t)$, Γ_t, and κ, which are variables necessary to reconstruct the dynamics of both the flag and its vortex sheet.

B.4 Numerical method

We present in this section some details of the numerical method used to solve the nonlinear system composed by Eqs. (B.28), (B.29), and (B.14). The numerical solution is performed using a coupled explicit-implicit method.

Initialisation At $t = t_1 = 0$, we assume that the flag is at rest but has an initial deformation. This condition is given by:

$$\hat{x}(z,0) \neq 0, \quad \frac{\partial \hat{x}}{\partial t} = 0, \quad \kappa(z,0) \neq 0. \tag{B.32}$$

For the vortex sheet, we assume that at $t = t_1 = 0$, both the bound vortex sheet C_f as well as the free vortex C_w has zero vorticity, which is expressed as:

$$\begin{aligned} &v(z,0) = 0, -1 \leq s \leq 1, \\ &\Gamma_t(1,0) = 0. \end{aligned} \tag{B.33}$$

For subsequent time steps t_{k+1}, with k=1, 2,..., we first apply an explicit method to compute the evolution of the free vortex sheet, which is convected downstream by its local velocity given by Eq. (B.21), and can be computed using the values of $\hat{x}(z,t)$, $\partial\hat{x}(z,t)/\partial t$, $v(z,k)$ and $\hat{x}(\Gamma,t)$ at previous time steps. We then use a Forward Euler scheme to compute the position of the newly created point at $t = t_k$ using the previously local velocity:

$$\hat{x}_k(t_{k+1}) = \hat{x}_f(t_k) + (t_{k+1} - t_k)\frac{\partial \hat{x}}{\partial t}\bigg|_{\hat{x}=\hat{x}_k, t=t_k} \tag{B.34}$$

and a second-order explicit Adams-Bashforth scheme to compute the displacement of the remaining $k-1$ points convected by local velocities at times t_k and t_{k-1}

$$\hat{x}_j(t_{k+1}) = \hat{x}_j(t_k) + (t_{k+1} - t_k)\left(A\,\frac{\partial \hat{x}}{\partial t}\bigg|_{\hat{x}=\hat{x}_j, t=t_k} + (1-A)\frac{\partial \hat{x}}{\partial t}\bigg|_{\hat{x}=\hat{x}_j, t=t_{k-1}}\right), \quad j = 1, ..., k-1, \tag{B.35}$$

where the parameter A is given by:

$$A = \frac{t_k + t_{k+1} - 2t_{k-1}}{2(t_k - t_{k-1})}. \tag{B.36}$$

For the bound vortex sheet, i.e. the flag, the variables v and κ are computed using an implicit method on N Chebyshev-Lobatto nodes in $-1 \leq z \leq 1$. The total circulation Γ_t, which is also the circulation of the newly created point of the free vortex sheet, located at $z = 1$, is also computed at this step. The integration and derivations in space of κ are computed using collocation operators introduced in [Weideman 2000]. At the time step $t = t_{k+1}$, the discrete nonlinear system $\mathbf{F}(\mathbf{q}) = 0$, solving the body variables, is given by, for $i = 1, ..., N$:

$$F_i(\mathbf{q}) = v(z_i, t_{k+1}) - 2\sum_{j=1}^{N} f_j(t)\sin\theta\sin j\theta + f_1(t) + 2f_0(t) - \frac{\Gamma_t(t)}{\pi}. \tag{B.37}$$

$$
\begin{aligned}
F_{i+N}(\mathbf{q}) &= Re\left(\left.\frac{\partial^2 \hat{x}}{\partial t^2}\right|_{z_i,t_{k+1}} \tilde{n}\right) + \frac{8}{U^{*2}}\left.\frac{\partial^2 \kappa}{\partial z^2}\right|_{z_i,t_{k+1}} - T(z_i,t_{k+1})\kappa(z_i,t_{k+1}) + \frac{M^*}{2}[p](z_i,t_{k+1}),\\
F_{2N-1}(\mathbf{q}) &= \kappa(z_N,t_{k+1}),\\
F_{2N-2}(\mathbf{q}) &= \left.\frac{\partial \kappa}{\partial z}\right|_{z_N,t_{k+1}}.
\end{aligned}
\tag{B.38}
$$

$$
F_{2N+1}(\mathbf{q}) - f_1(t) - 2f_0(t) + \frac{\Gamma_t(t)}{\pi} = 0. \tag{B.39}
$$

Equations (B.37), (B.38), and (B.39) are respectively the projection on the Chebyshev-Lobatto nodes of Eqs (B.28), (B.14), and (B.29). The vector of unknowns $\mathbf{q}$ is given by:

$$
\begin{aligned}
&q_j = v(z_j,t_{k+1}), \quad j = 1,...,N,\\
&q_{j+N} = \kappa(z_j,t_{k+1}), \quad j = 1,...,N,\\
&q_{2N+1} = \Gamma_t(t_{k+1}).
\end{aligned}
\tag{B.40}
$$

This nonlinear system is solved with the Broyden's method, an iterative quasi-Newton method proposed in [Broyden 1965]. At $t = t_{k+1}$, an initial guess of $\mathbf{q}^0_{k+1}$ is obtained using a second-order extrapolation with $\mathbf{q}_k$ and $\mathbf{q}_{k-1}$. This initial guess is then used for iterations until a solution $\mathbf{q}_{k+1}$ satisfying $\mathbf{F}(\mathbf{q}) = 0$ is found. In order to ensure small relative changes in the solution between time steps, we use an adaptive time stepping. At each time step, we compute the relative difference between the current solution $\mathbf{q}_{k+1}$ and the initial guess $\mathbf{q}^0_{k+1}$. If the relative difference exceeds a tolerance ε, the time step is multiplied by 0.95, while if the relative difference is smaller than $\varepsilon/3$, the time step is multiplied by 1.05. The solution at $t = t_{k+1}$ is computed again using the new time step. In the current work, we choose $\varepsilon = 0.005$.

Appendix C

Linear equations for Flexible body vortex sheet model applied on two flags

In this appendix, we will present the formulation of an eigenvalue problem using the flexible body vortex sheet model. In [Alben 2008b], an eigenvalue problem is formulated using the same model applied on a single flag. In this text, this formulation will be extended to two flags placed side by side.

Before showing details of formulation, we establish the terminology that will be used in the following text. In our point of view, the flag placed over the other will be referred as the flag 1, and the one below as the flag 2. The distance separating the two flags is d. In order to use Cheybshev polynomials, all variables are rendered dimensionless using the same characteristic scales as in Appendix B.

Firstly, we write the governing linear equations of the coupled dynamics of the two flags. Note that at this stage, only the equations of the flag 1 will be presented, and those of the flag 2 are straightforward to obtain by changing indexes.

$$\frac{\partial^2 y_1}{\partial t^2} + \frac{8}{U^{*2}}\frac{\partial^4 y_1}{\partial x_1^4} + \frac{M^*}{2}[p]_1 = 0, \tag{C.1}$$

$$\frac{\partial \gamma_1}{\partial t} + \frac{\partial \gamma_1}{\partial s} = \frac{\partial [p]_1}{\partial x_1}. \tag{C.2}$$

$$\frac{\partial y_1}{\partial t} + \frac{\partial y_1}{\partial x_1} = \frac{1}{2\pi}\int_{-1}^{1} \frac{\gamma_1(x_1', t)}{x_1 - x_1'}\mathrm{d}x_1' + \frac{1}{2\pi}\int_{1}^{C_w^1} \frac{\gamma_1(x_1', t)}{x_1 - x_1'}\mathrm{d}x_1' + U_{2\to 1}(x_1, t), \tag{C.3}$$

$$\int_{-1}^{1} \frac{\gamma_1(x_1', t)}{x_1 - x_1'}\mathrm{d}x_1' + \Gamma_1(1, t) = 0. \tag{C.4}$$

Equations (C.1)–(C.4) represent respectively the Euler-Bernoulli beam model, the Bernoulli's theorem for computing the pressure jump, the impermeable condition on the flag, and the Kelvin's theorem concerning the total circulation. The variable x_1 is the coordinate along the flag and the free vortex sheet, y_1 is the flag's vertical displacement, γ_1 is the vorticity strength. The term $U_{2\to 1}(x_1, t)$ in Eq. (C.3) represents the contribution of the lower flag to the flow field surrounding the upper flag. It is given by:

$$U_{2\to 1}(x_1, t) = \frac{1}{2\pi}\int_{-1}^{1} \frac{\gamma_2(x_2', t)(x_1 - x_2')}{(x_1 - x_1')^2 + d^2}\mathrm{d}x_2' + \frac{1}{2\pi}\int_{1}^{C_w^2} \frac{\gamma_2(x_2', t)}{(x_1 - x_1')^2 + d^2}\mathrm{d}x_2' \tag{C.5}$$

We assume that all variables take the following form:

$$y_1 = Y_1(x_1)\mathrm{e}^{-\mathrm{i}\omega t}, \quad \gamma_1 = g_1(x_1)\mathrm{e}^{-\mathrm{i}\omega t}, \quad v_1 = V_1(x_1)\mathrm{e}^{-\mathrm{i}\omega t}, \quad \Gamma_1 = \Gamma_1(x_1)\mathrm{e}^{-\mathrm{i}\omega t}, \tag{C.6}$$

where v_1 is the regular part of γ_1, defined by:

$$v_1(x_1,t) = \frac{\gamma_1(x_1,t)}{\sqrt{1-x_1'^2}}, \quad V_1(x_1) = \frac{g_1(x_1)}{\sqrt{1-x_1'^2}}. \tag{C.7}$$

Using variables in the form presented in Eq. (C.6), we will show how to re-write Eqs. (C.1)–(C.4) into an eigenvalue problem.

Let us start with Eqs (C.1) and (C.2). By developing time derivatives in these two equations, we have:

$$-\omega^2 Y_1(x_1) + \frac{8}{U^{*2}}\frac{\partial^4 Y_1(x_1)}{\partial x_1^4} + \frac{M^*}{2}[p_1](x_1) = 0, \tag{C.8}$$

$$[p_1](x_1) = -\mathrm{i}\omega\int_{-1}^{x_1} g_1(x_1')\mathrm{d}x_1' + g_1(x_1). \tag{C.9}$$

Hence

$$-\omega^2 Y_1(x_1) + \frac{8}{U^{*2}}\frac{\partial^4 Y_1(x_1)}{\partial x_1^4} - \mathrm{i}\omega\frac{M^*}{2}\int_{-1}^{x_1} g_1(x_1')\mathrm{d}x_1' + \frac{M^*}{2}g_1(x_1) = 0. \tag{C.10}$$

Next, we re-write Eq. (C.3) into the following form:

$$\begin{aligned}-\mathrm{i}\omega Y_1 + \frac{\partial Y_1}{\partial x_1} = \frac{1}{2\pi}\fint_{-1}^{1}\frac{V_1(x_1')}{\sqrt{1-x_1^2}(x_1-x_1')}\mathrm{d}x_1' + \frac{1}{2\pi}\int_{-1}^{1}\frac{V_2(x_2',t)(x_1-x_2')}{\sqrt{1-x_2^2}[(x_1-x_2')^2+d^2]}\mathrm{d}x_2' \\ + \frac{1}{2\pi}\fint_{1}^{C_w}\frac{g_1(x_1',t)}{x_1-x_1'}\mathrm{d}x_1' + \frac{1}{2\pi}\int_{1}^{C_w}\frac{g_2(x_2',t)}{(x_1-x_1')^2+d^2}\mathrm{d}x_2'.\end{aligned} \tag{C.11}$$

We use now the following change of variables:

$$x_1 = \cos\theta_1 \quad \rightarrow \quad \mathrm{d}x_1 = -\sin\theta_1\mathrm{d}\theta_1. \tag{C.12}$$

As $x \in [-1,1]$, the variable θ is defined as $\theta \in [\pi,1]$ This change of variable also implies that:

$$\sqrt{1-x_1^2} = |\sin\theta_1|. \tag{C.13}$$

Using Eqs. (C.12) and (C.13), for both flags, Equations (C.10) and (C.11) becomes:

$$-\omega^2 Y_1(x_1) + \frac{8}{U^{*2}}\frac{\partial^4 Y_1(x_1)}{\partial x_1^4} - \mathrm{i}\omega\frac{M^*}{2}\int_0^{\theta_1} v_1(\theta_1')\mathrm{d}\theta_1' + \frac{M^*}{2}\frac{v_1(x_1)}{\sqrt{1-x_1^2}} = 0. \tag{C.14}$$

$$-\omega^2 Y_2(x_2) + \frac{8}{U^{*2}}\frac{\partial^4 Y_2(x_2)}{\partial x_2^4} - \frac{M^*}{2}\mathrm{i}\omega\int_0^{\theta_2} v_2(\theta_2')\mathrm{d}\theta_2' + \frac{M^*}{2}\frac{v_2(x_2)}{\sqrt{1-x_2^2}} = 0. \tag{C.15}$$

$$-\mathrm{i}\omega Y_1+\frac{\partial Y_1}{\partial x_1}=\underbrace{\frac{1}{2\pi}\fint_{-1}^{1}\frac{V_1(x_1')}{\sqrt{1-x_1^2}(x_1-x_1')}\mathrm{d}x_1'}_{A_1}+\underbrace{\frac{1}{2\pi}\int_{-1}^{1}\frac{V_2(x_2',t)(x_1-x_2')}{\sqrt{1-x_2'^2}[(x_1-x_2')^2+d^2]}\mathrm{d}x_2'}_{B_1}$$
$$+\underbrace{\frac{1}{2\pi}\fint_{1}^{C_w}\frac{g_1(x_1',t)}{x_1-x_1'}\mathrm{d}x_1'}_{C_1}+\underbrace{\frac{1}{2\pi}\int_{1}^{C_w}\frac{g_2(x_2',t)}{(x_1-x_2')^2+d^2}\mathrm{d}x_2'}_{D_1} \tag{C.16}$$

$$-\mathrm{i}\omega Y_2+\frac{\partial Y_2}{\partial x_2}=\underbrace{\frac{1}{2\pi}\fint_{-1}^{1}\frac{V_2(x_2')}{\sqrt{1-x_2^2}(x_2-x_2')}\mathrm{d}x_2'}_{A_2}+\underbrace{\frac{1}{2\pi}\int_{-1}^{1}\frac{V_1(x_1',t)(x_2-x_1')}{\sqrt{1-x_1'^2}[(x_2-x_1')^2+d^2]}\mathrm{d}x_2'}_{B_2}$$
$$+\underbrace{\frac{1}{2\pi}\fint_{1}^{C_w}\frac{g_2(x_2',t)}{x_2-x_2'}\mathrm{d}x_1'}_{C_2}+\underbrace{\frac{1}{2\pi}\int_{1}^{C_w}\frac{g_1(x_1',t)}{(x_2-x_1')^2+d^2}\mathrm{d}x_1'}_{D_2} \tag{C.17}$$

For Eq. (C.4), the Kelvin's theorem, we use the invariance of the circulation $\Gamma_1(x_1,t)$ on each material point of the free vortex sheet that is convected downstream at dimensionless speed 1. Therefore, the material point at location $x\geq 1$ at time t was at location $x=1$ at time $t-(x-1)$. Thus by Eq. (C.6), we have:

$$\Gamma_1(x,t)=\Gamma_1^0\mathrm{e}^{-\mathrm{i}\omega(t-(x_1-1))},\quad 1\leq x\leq C_w. \tag{C.18}$$

As a result, the vorticity strength on the free vortex sheet is given by:

$$\gamma_1(x_1,t)=\frac{\partial\Gamma_1}{\partial x_1}=\mathrm{i}\omega\Gamma_1^0\mathrm{e}^{-\mathrm{i}\omega(t-(x_1-1))},\quad 1\leq x\leq C_w, \tag{C.19}$$

and

$$g_1(x_1)=\mathrm{i}\omega\Gamma_1^0\mathrm{e}^{\mathrm{i}\omega(x_1-1)},\quad 1\leq x\leq C_w. \tag{C.20}$$

Note that the result in Eq. (C.20) are to be applied to Eqs. (C.16) and (C.17), to simplify the calculation of terms C_1, D_1, C_2 and D_2.

The Kelvin's theorem is therefore written, for both flags as:

$$\int_0^{\pi}v_1(\theta_1)\mathrm{d}\theta_1+\Gamma_1^0=0, \tag{C.21}$$
$$\int_0^{\pi}v_2(\theta_2)\mathrm{d}\theta_2+\Gamma_2^0=0, \tag{C.22}$$

Equations (C.14)–(C.17), and (C.21)–(C.22) are then to be written into matrix form. All body variables Y and V will be expanded using Chebyshev polynomials as:

$$\begin{aligned}Y_1(x_1)&=\sum_{k=1}^{m+1}Y_1^kT_k(x_1),\quad Y_2(x_2)=\sum_{k=1}^{m+1}Y_2^kT_k(x_2),\\ V_1(x_1)&=\sum_{k=1}^{m+1}V_1^kT_k(x_1),\quad V_2(x_2)=\sum_{k=1}^{m+1}V_2^kT_k(x_2),\end{aligned} \tag{C.23}$$

where T_k are the Cheybshev polynomials of the first kind.

We still start with Eqs. (C.14) and (C.15), their matrix form is written as:

$$-\omega^2\mathbf{I}\cdot\mathbf{Y}_1 - \mathrm{i}\omega\mathbf{IPh}\cdot\mathbf{V}_1 + \frac{8}{U^{*2}}\mathbf{D}_4\cdot\mathbf{Y}_1 + \mathbf{K}\cdot\mathbf{V}_1 = \mathbf{0}, \tag{C.24}$$

$$-\omega^2\mathbf{I}\cdot\mathbf{Y}_2 - \mathrm{i}\omega\mathbf{IPh}\cdot\mathbf{V}_2 + \frac{8}{U^{*2}}\mathbf{D}_4\cdot\mathbf{Y}_2 + \mathbf{K}\cdot\mathbf{V}_2 = \mathbf{0}. \tag{C.25}$$

where

$$\{\mathbf{Y}_{1(2)}\}_k = Y_{1(2)}(x_k), \quad \{\mathbf{V}_{1(2)}\}_k = V_{1(2)}(x_k), \quad k = 1, ..., m+1. \tag{C.26}$$

In Eqs. (C.24) and (C.25), $\mathbf{I}$ is a $N \times N$ identity matrix. The operator $\mathbf{IPh}$ is an $N \times N$ matrix that multiplies an vector to obtains the latter's integration on θ. To give an example, supposing an vector $\mathbf{q}$ given by the function $q(x)$ defined on $x \in [-1, 1]$ as:

$$\{\mathbf{q}\}_j = q(x_j) = q(\cos\theta_j). \tag{C.27}$$

where $\theta \in [\pi, 0]$. The operator $\mathbf{IPh}$ gives the following result:

$$\mathbf{IPh}\cdot\mathbf{q} = \mathbf{Q}, \tag{C.28}$$

where $\mathbf{Q}$ is given by:

$$\{\mathbf{Q}\}_j = \int_0^{\theta_j} q(\cos\theta')\mathrm{d}\theta'. \tag{C.29}$$

The operator $\mathbf{D}_n$ computes the n^{th} derivative in space of this vector on every node. Finally, the operator $\mathbf{K}$ is a diagonal matrix that is defined by:

$$\{\mathbf{K}\}_{j,j} = \frac{1}{\sqrt{1-x_j^2}}. \tag{C.30}$$

Equations (C.16) and (C.17) are slightly more difficult to be written into matrix form. The following identity will be used in the ensuing calculation:

$$\int_{-1}^{1} \frac{T_n(x')}{\sqrt{1-x'^2}(x-x')}\mathrm{d}x' = -\pi U_{n-1}(x), \tag{C.31}$$

where U_n are the Chebyshev polynomials of the second kind. Using this equality, the terms A_1 and A_2 are written as follows:

$$A_1: \quad -\frac{1}{2}\mathbf{U}\cdot\mathbf{Inv}\cdot\mathbf{V}_1, \quad A_2: \quad -\frac{1}{2}\mathbf{U}\cdot\mathbf{Inv}\cdot\mathbf{V}_2. \tag{C.32}$$

In Eq. (C.32), $\mathbf{U}$ is defined as:

$$\{\mathbf{U}\}_{j,1} = 0, \quad \{\mathbf{U}\}_{j,k} = U_{k-1}(x_j), \quad k = 2, ..., N. \tag{C.33}$$

The operators $\mathbf{Inv}$ multiplies a vector $\mathbf{a}$ to obtain another vector $\tilde{\mathbf{a}}$ composed by the coefficients obtained by expanding the vector $\mathbf{a}$ on $\{T_n\}$:

$$\mathbf{a} = \sum_{k=1}^{N} \tilde{a}_k T_k(\mathbf{x}) \quad \rightarrow \quad \tilde{\mathbf{a}} = \mathbf{Inv}\cdot\mathbf{a}. \tag{C.34}$$

The terms B_1 and B_2 are written as:

$$B_1: \quad \frac{1}{2\pi}\mathbf{L}_1 \cdot \mathbf{Inv} \cdot \mathbf{V}_1, \quad B_2: \quad \frac{1}{2\pi}\mathbf{L}_2 \cdot \mathbf{Inv} \cdot \mathbf{V}_2, \tag{C.35}$$

where the operators $\mathbf{L}_1$ and $\mathbf{L}_2$ are defined as

$$\{\mathbf{L}_1\}_{j,k} = \int_{-1}^{1} \frac{T_k(x_2')(x_1^j - x_2')}{\sqrt{1-x_1'^2}[(x_1^j - x_2')^2 + d^2]}, \quad \{\mathbf{L}_2\}_{j,k} = \int_{-1}^{1} \frac{T_k(x_1')(x_2^j - x_1')}{\sqrt{1-x_2'^2}[(x_2^j - x_1')^2 + d^2]}. \tag{C.36}$$

Using Eqs. (C.20), the terms B_1 and B_2 are written as:

$$\begin{aligned} C_1: \quad & \frac{1}{2\pi}\mathrm{i}\omega\Gamma_1^0 \int_1^{C_w} \frac{\mathrm{e}^{\mathrm{i}(x_1'-1)}}{x_1 - x_1'} \to \omega\Gamma_1^0\mathbf{b}_1, \\ C_2: \quad & \frac{1}{2\pi}\mathrm{i}\omega\Gamma_2^0 \int_1^{C_w} \frac{\mathrm{e}^{\mathrm{i}(x_2'-1)}}{x_2 - x_2'} \to \omega\Gamma_2^0\mathbf{b}_2, \end{aligned} \tag{C.37}$$

where the vectors $\mathbf{b}_1$ and $\mathbf{b}_2$ are given by:

$$\{\mathbf{b}_1\}_j = \frac{\mathrm{i}}{2\pi}\int_1^{C_w} \frac{\mathrm{e}^{\mathrm{i}(x_1'-1)}}{x_1^j - x_1'}, \quad \{\mathbf{b}_2\}_j = \frac{\mathrm{i}}{2\pi}\int_1^{C_w} \frac{\mathrm{e}^{\mathrm{i}(x_2'-1)}}{x_2^j - x_2'}. \tag{C.38}$$

Finally, the terms D_1 and D_2 are written as

$$\begin{aligned} D_1: \quad & \frac{1}{2\pi}\mathrm{i}\omega\Gamma_2^0 \int_1^{C_w} \frac{\mathrm{e}^{\mathrm{i}(x_2'-1)}(x_1 - x_2')}{(x_1 - x_2')^2 + d^2} \to \omega\Gamma_2^0\mathbf{b}_{2\to1}, \\ D_2: \quad & \frac{1}{2\pi}\mathrm{i}\omega\Gamma_1^0 \int_1^{C_w} \frac{\mathrm{e}^{\mathrm{i}(x_1'-1)}(x_2 - x_1')}{(x_2 - x_1')^2 + d^2} \to \omega\Gamma_1^0\mathbf{b}_{1\to2}, \end{aligned} \tag{C.39}$$

where the vectors $\mathbf{b}_{2\to1}$ and $\mathbf{b}_{1\to2}$ are given by:

$$\{\mathbf{b}_{2\to1}\}_j = \frac{\mathrm{i}}{2\pi}\int_1^{C_w} \frac{\mathrm{e}^{\mathrm{i}(x_2'-1)}(x_1^j - x_2')}{(x_1^j - x_2')^2 + d^2}, \quad \{\mathbf{b}_{1\to2}\}_j = \frac{\mathrm{i}}{2\pi}\int_1^{C_w} \frac{\mathrm{e}^{\mathrm{i}(x_1'-1)}(x_2^j - x_1')}{(x_2^j - x_1')^2 + d^2}. \tag{C.40}$$

The matrix form of Eqs (C.16) and (C.17) are finally obtained as:

$$-\mathrm{i}\omega\mathbf{Y}_1 - \omega\Gamma_1^0\mathbf{b}_1 - \omega\Gamma_2^0\mathbf{b}_{2\to1} + \mathbf{D}_1 \cdot \mathbf{Y}_1 + \frac{1}{2}\mathbf{U} \cdot \mathbf{Inv} \cdot \mathbf{V}_1 - \frac{1}{2\pi}\mathbf{L}_1 \cdot \mathbf{Inv} \cdot \mathbf{V}_2 = 0, \tag{C.41}$$

$$-\mathrm{i}\omega\mathbf{Y}_2 - \omega\Gamma_1^0\mathbf{b}_{1\to2} - \omega\Gamma_2^0\mathbf{b}_2 + \mathbf{D}_1 \cdot \mathbf{Y}_2 - \frac{1}{2\pi}\mathbf{L}_2 \cdot \mathbf{Inv} \cdot \mathbf{V}_1 + \frac{1}{2}\mathbf{U} \cdot \mathbf{Inv} \cdot \mathbf{V}_2 = 0. \tag{C.42}$$

Finally, the matrix equations corresponding to the Kelvin's theorem are the following:

$$\mathbf{IPh}_0^\pi \cdot \mathbf{V}_1 + \Gamma_1^0 = 0, \tag{C.43}$$

$$\mathbf{IPh}_0^\pi \cdot \mathbf{V}_2 + \Gamma_2^0 = 0, \tag{C.44}$$

where the operator $\mathbf{IPh}_0^\pi$ multiplies a vector to compute its integration over the interval $[0, \pi]$.

The nonlinear eigenvalue problem is therefore written as:

$$\omega^2 \mathbf{A}_2 + \omega \mathbf{A}_1 + \mathbf{A}_0 = 0. \tag{C.45}$$

The matrices $\mathbf{A}_2$, $\mathbf{A}_1$, and $\mathbf{A}_0$ take the following form:

$$\mathbf{A}_2 = \begin{bmatrix} \mathbf{A}_2^1 & \mathbf{O} \\ \mathbf{O} & \mathbf{A}_2^2 \end{bmatrix}, \quad \mathbf{A}_1 = \begin{bmatrix} \mathbf{A}_1^1 & \mathbf{A}_1^{2\to1} \\ \mathbf{A}_1^{1\to2} & \mathbf{A}_1^2 \end{bmatrix}, \quad \mathbf{A}_0 = \begin{bmatrix} \mathbf{A}_0^1 & \mathbf{A}_0^{2\to1} \\ \mathbf{A}_0^{1\to2} & \mathbf{A}_0^2 \end{bmatrix}. \tag{C.46}$$

And their components are given by following matrices:

$$\mathbf{A}_2^1 = \begin{bmatrix} -\mathbf{I} & \mathbf{O} & \mathbf{0} \\ \mathbf{O} & \mathbf{O} & \mathbf{0} \\ \mathbf{0}^T & \mathbf{0}^T & 0 \end{bmatrix}, \quad \mathbf{A}_1^1 = \begin{bmatrix} \mathbf{O} & -\mathrm{i}\mathbf{IPh} & \mathbf{0} \\ -\mathrm{i}\mathbf{I} & \mathbf{O} & -\mathbf{b}_1 \\ \mathbf{0}^T & \mathbf{0}^T & 0 \end{bmatrix}, \quad \mathbf{A}_1^{2\to1} = \begin{bmatrix} \mathbf{O} & \mathbf{O} & \mathbf{0} \\ \mathbf{O} & \mathbf{O} & -\mathbf{b}_{2\to1} \\ \mathbf{0}^T & \mathbf{0}^T & 0 \end{bmatrix} \tag{C.47}$$

$$\mathbf{A}_0^1 = \begin{bmatrix} \frac{8}{U^{*2}}\mathbf{D}_4 & \mathbf{K} & \mathbf{0} \\ \mathbf{D}_1 & \frac{1}{2}\mathbf{U}\cdot\mathbf{Inv} & \mathbf{0} \\ \mathbf{0}^T & \mathbf{IPh}_0^\pi & 1 \end{bmatrix}, \quad \mathbf{A}_0^{2\to1} = \begin{bmatrix} \mathbf{O} & \mathbf{O} & \mathbf{0} \\ \mathbf{O} & \frac{1}{2}\mathbf{L}_1\cdot\mathbf{Inv} & \mathbf{0} \\ \mathbf{0}^T & \mathbf{0}^T & 0 \end{bmatrix} \tag{C.48}$$

$$\mathbf{A}_2^2 = \begin{bmatrix} -\mathbf{I} & \mathbf{O} & \mathbf{0} \\ \mathbf{O} & \mathbf{O} & \mathbf{0} \\ \mathbf{0}^T & \mathbf{0}^T & 0 \end{bmatrix}, \quad \mathbf{A}_1^2 = \begin{bmatrix} \mathbf{O} & -\mathrm{i}\mathbf{IPh} & \mathbf{0} \\ -\mathrm{i}\mathbf{I} & \mathbf{O} & -\mathbf{b}_2 \\ \mathbf{0}^T & \mathbf{0}^T & 0 \end{bmatrix}, \quad \mathbf{A}_1^{1\to2} = \begin{bmatrix} \mathbf{O} & \mathbf{O} & \mathbf{0} \\ \mathbf{O} & \mathbf{O} & -\mathbf{b}_{1\to2} \\ \mathbf{0}^T & \mathbf{0}^T & 0 \end{bmatrix} \tag{C.49}$$

$$\mathbf{A}_0^2 = \begin{bmatrix} \frac{8}{U^{*2}}\mathbf{D}_4 & \mathbf{K} & \mathbf{0} \\ \mathbf{D}_1 & \frac{1}{2}\mathbf{U}\cdot\mathbf{Inv} & \mathbf{0} \\ \mathbf{0}^T & \mathbf{IPh}_0^\pi & 1 \end{bmatrix}, \quad \mathbf{A}_0^{1\to2} = \begin{bmatrix} \mathbf{O} & \mathbf{O} & \mathbf{0} \\ \mathbf{O} & \frac{1}{2}\mathbf{L}_2\cdot\mathbf{Inv} & \mathbf{0} \\ \mathbf{0}^T & \mathbf{0}^T & 0 \end{bmatrix} \tag{C.50}$$

Note that $\mathbf{O}$ is a $N \times N$ zero matrix, and $\mathbf{0}$ is a $N \times 1$ zero vector.

Bibliography

[Akcabay 2012] D. T. Akcabay and Y. L. Young. *Hydroelastic response and energy harvesting potential of flexible piezoelectric beams in viscous flow.* Phys. Fluids., vol. 24, no. 054106, 2012. (Cited on pages 9 and 12.)

[Alben 2008a] S. Alben and M. J. Shelley. *Flapping States of a Flag in a Inviscid Fluid: Bistability and the Transition to Chaos.* Phys. Rev. Lett., vol. 100, page 074301, 2008. (Cited on pages 4, 26 and 117.)

[Alben 2008b] Silas Alben. *The flapping-flag instability as a nonlinear eigenvalue problem.* Physics of Fluids (1994-present), vol. 20, no. 10, page 104106, 2008. (Cited on pages 92 and 123.)

[Alben 2009a] S. Alben. *Simulating the dynamics of flexible bodies and vortex sheets.* J. Comput. Phys., vol. 228, pages 2587–2603, 2009. (Cited on pages 19, 48, 86, 87 and 117.)

[Alben 2009b] Silas Alben. *Wake-mediated synchronization and drafting in coupled flags.* Journal of Fluid Mechanics, vol. 641, pages 489–496, 2009. (Cited on pages 7, 8, 81, 86, 89 and 101.)

[Alben 2010] S. Alben. *Regularizing a vortex sheet near a separation point.* J. Comput. Phys., vol. 229, no. 13, pages 5280 – 5298, 2010. (Cited on page 117.)

[Alben 2015] Silas Alben. *Flag flutter in inviscid channel flow.* Physics of Fluids (1994-present), vol. 27, no. 3, page 033603, 2015. (Cited on pages 5 and 6.)

[Allen 2001] J. J. Allen and A. J. Smits. *Energy harvesting eel.* J. Fluids Struct., vol. 15, pages 629–640, 2001. (Cited on pages 8, 12, 50 and 107.)

[Antman 1995] Stuart S Antman. Nonlinear problems of elasticity. Springer, 1995. (Cited on page 13.)

[Anton 2007] S.R. Anton and H.A.Sodano. *A review of power harvesting using piezoelectric materials (2003–2006).* Smart Mater. Struct., vol. 16, no. 3, page R1, 2007. (Cited on pages 11 and 52.)

[Belanger 1995] Francois Belanger, Michael P Paidoussis and Emmanuel de Langre. *Time-marching analysis of fluid-coupled systems with large added mass.* AIAA journal, vol. 33, no. 4, pages 752–757, 1995. (Cited on pages 5, 6 and 33.)

[Bernitsas 2008] M. M. Bernitsas, K. Raghavan, Y. Ben-Simon and E. M. Garcia. *VIVACE (Vortex Induced Vibration Aquatic Clean Energy): A New Concept in Generation of Clean and Renewable Energy From Fluid Flow.* J. Offshore Mech. Arct. Eng., vol. 130, page 041101, 2008. (Cited on page 1.)

[Bisegna 2006] P. Bisegna, G. Caruso and F. Maceri. *Optimized electric networks for vibration damping of piezoactuated beams.* J. Sound Vib., vol. 289, pages 908–937, 2006. (Cited on pages 11, 58, 59 and 61.)

[Boragno 2012] C Boragno, R Festa and A Mazzino. *Elastically bounded flapping wing for energy harvesting.* Applied Physics Letters, vol. 100, no. 25, page 253906, 2012. (Cited on page 1.)

[Bourlet 2015] Thibaut F Bourlet, Pardha S Gurugubelli and Rajeev K Jaiman. *The boundary layer development and traveling wave mechanisms during flapping of a flexible foil.* Journal of Fluids and Structures, vol. 54, pages 784–801, 2015. (Cited on page 5.)

[Broyden 1965] C. G. Broyden. *A Class of Methods for Solving Nonlinear Simultaneous Equations.* Mathematics of Computation, vol. 19, pages 577 – 593, 1965. (Cited on pages 48 and 121.)

[Buchak 2010] Peter Buchak, Christophe Eloy and Pedro M Reis. *The Clapping Book: wind-driven oscillations in a stack of elastic sheets.* Phys. Rev. Lett., vol. 105, no. 19, page 194301, 2010. (Cited on page 15.)

[Caliò 2014] Renato Caliò, Udaya Bhaskar Rongala, Domenico Camboni, Mario Milazzo, Cesare Stefanini, Gianluca de Petris and Calogero Maria Oddo. *Piezoelectric Energy Harvesting Solutions.* Sensors, vol. 14, no. 3, pages 4755–4790, 2014. (Cited on pages 11 and 52.)

[Candelier 2011] F. Candelier, F. Boyer and A. Leroyer. *Three-dimensional extension of Lighthill's large-amplitude elongated-body theory of fish locomotion.* J. Fluid Mech., vol. 674, pages 196–226, 2011. (Cited on pages 4 and 15.)

[Candelier 2013] Fabien Candelier, Mathieu Porez and Frederic Boyer. *Note on the swimming of an elongated body in a non-uniform flow.* Journal of Fluid Mechanics, vol. 716, pages 616–637, 2013. (Cited on page 103.)

[Chen 2015] Yu-Yin Chen and Dejan Vasic. *Energy harvesting of two cantilever beams structure: interfacing circuit discussion.* In SPIE Smart Structures and Materials+ Nondestructive Evaluation and Health Monitoring, pages 943508–943508. International Society for Optics and Photonics, 2015. (Cited on page 103.)

[Curie 1880a] Jacques Curie and Pierre Curie. *Développement par compression de l'électricité polaire dans les cristaux hémièdres à faces inclinées.* Bulletin de la Société minérologique de France, vol. 3, pages 90–93, 1880. (Cited on page 9.)

[Curie 1880b] Jacques Curie and Pierre Curie. *Sur l'électricité polaire dans les cristaux hémièdres à faces inclinées.* Comptes rendus hebdomadaires des

séances de l'Académie des sciences, vol. 91, pages 383–386, 1880. (Cited on page 9.)

[Curie 1881] Jacques Curie and Pierre Curie. *Contractions et dilatations produites par des tensions dans les cristaux hémièdres à faces inclinées.* Comptes rendus hebdomadaires des séances de l'Académie des sciences, vol. 93, pages 1137–1140, 1881. (Cited on page 9.)

[Cushing 1968] DH Cushing and FR Jones. *Why do fish school?* Nature, vol. 218, no. 5145, pages 918–920, 1968. (Cited on page 6.)

[De Marqui 2011] Carlos De Marqui, Wander GR Vieira, Alper Erturk and Daniel J Inman. *Modeling and analysis of piezoelectric energy harvesting from aeroelastic vibrations using the doublet-lattice method.* J. Vib. Acoust., vol. 133, no. 1, page 011003, 2011. (Cited on page 12.)

[Dessi 2015] Daniele Dessi and Saverio Mazzocconi. *Aeroelastic behavior of a flag in ground effect.* Journal of Fluids and Structures, vol. 55, pages 303–323, 2015. (Cited on page 5.)

[Dias 2013] J. A. C. Dias, Jr. C. De Marqui and A. Erturk. *Hybrid piezoelectric–inductive flow energy harvesting and dimensionless electroaeroelastic analysis for scaling.* App. Phys. Lett., vol. 102, no. 4, page 044101, 2013. (Cited on page 12.)

[Doaré 2010] O. Doaré. *Dissipation effect on local and global stability of fluid-conveying pipes.* J. Sound Vib., vol. 329, no. 1, pages 72 – 83, 2010. (Cited on pages 20 and 47.)

[Doaré 2011a] O. Doaré and S. Michelin. *Piezoelectric coupling in energy-harvesting fluttering flexible plates: linear stability analysis and conversion efficiency.* J. Fluids Struct., vol. 27, no. 8, pages 1357 – 1375, 2011. (Cited on pages 9, 12, 20, 23, 42, 46, 47, 52 and 54.)

[Doaré 2011b] O. Doaré, M. Sauzade and C. Eloy. *Flutter of an elastic plate in a channel flow: Confinement and finite-size effects.* Journal of Fluids and Structures, vol. 27, no. 1, pages 76 – 88, 2011. (Cited on page 6.)

[Doaré 2011c] Olivier Doaré, David Mano and Juan Carlos Bilbao Ludena. *Effect of spanwise confinement on flag flutter: Experimental measurements.* Physics of Fluids, vol. 23, no. 11, pages –, 2011. (Cited on pages 6 and 23.)

[Ducarne 2012] J Ducarne, O Thomas and J-F Deü. *Placement and dimension optimization of shunted piezoelectric patches for vibration reduction.* Journal of Sound and Vibration, vol. 331, no. 14, pages 3286–3303, 2012. (Cited on pages 11, 16 and 54.)

[Dunnmon 2011] J. A. Dunnmon, S. C. Stanton, B. P. Mann and E. H. Dowell. *Power extraction from aeroelastic limit cycle oscillations.* J. Fluids Struct., vol. 27, no. 8, pages 1182–1198, 2011. (Cited on pages 9, 12, 20 and 23.)

[Eloy 2007] C. Eloy, C. Souilliez and L. Schouveiler. *Flutter of a rectangular plate.* J. Fluids Struct., vol. 23, no. 6, pages 904 – 919, 2007. (Cited on pages 3, 4, 26 and 46.)

[Eloy 2008] C. Eloy, R. Lagrange, C. Souilliez and L. Schouveiler. *Aeroelastic instability of cantilevered flexible plates in uniform flow.* J. Fluid Mech., vol. 611, pages 97 – 106, 2008. (Cited on page 26.)

[Eloy 2012] C. Eloy, N. Kofman and L. Schouveiler. *The origin of hysteresis in the flag instability.* J. Fluid Mech., vol. 691, pages 583–593, 2012. (Cited on pages 4, 15, 16 and 26.)

[Erturk 2009] A Erturk and Daniel J Inman. *An experimentally validated bimorph cantilever model for piezoelectric energy harvesting from base excitations.* Smart Materials and Structures, vol. 18, no. 2, page 025009, 2009. (Cited on page 16.)

[Erturk 2011] Alper Erturk and Daniel J Inman. Piezoelectric energy harvesting. John Wiley & Sons, 2011. (Cited on page 11.)

[Farnell 2004] DJJ Farnell, T David and DC Barton. *Coupled states of flapping flags.* Journal of fluids and structures, vol. 19, no. 1, pages 29–36, 2004. (Cited on pages 7, 81 and 87.)

[Giacomello 2011] A. Giacomello and M. Porfiri. *Underwater energy harvesting from a heavy flag hosting ionic polymer metal composites.* J Appl. Phys., vol. 109, no. 8, pages 084903–084903–10, 2011. (Cited on page 9.)

[Gibbs 2012] S Chad Gibbs, Ivan Wang and Earl Dowell. *Theory and experiment for flutter of a rectangular plate with a fixed leading edge in three-dimensional axial flow.* Journal of Fluids and Structures, vol. 34, pages 68–83, 2012. (Cited on page 4.)

[Gibbs 2014] SC Gibbs, Sebastiano Fichera, Alex Zanotti, Sergio Ricci and Earl H Dowell. *Flow field around the flapping flag.* Journal of Fluids and Structures, vol. 48, pages 507–513, 2014. (Cited on page 4.)

[Grouthier 2013] C. Grouthier, S. Michelin, Y. Modarres-Sadeghi and E. de Langre. *Self–similar vortex–induced vibrations of a hanging string.* J. Fluid Mech., vol. 724, 2013. (Cited on page 49.)

[Grouthier 2014] Clément Grouthier, Sébastien Michelin, Rémi Bourguet, Yahya Modarres-Sadeghi and Emmanuel de Langre. *On the efficiency of energy harvesting using vortex-induced vibrations of cables.* J. Fluids Struct., vol. 49, pages 427–440, 2014. (Cited on pages 1, 57 and 80.)

[Guo 2000] CQ Guo and MP Paidoussis. *Stability of rectangular plates with free side-edges in two-dimensional inviscid channel flow.* Journal of Applied Mechanics, vol. 67, no. 1, pages 171–176, 2000. (Cited on pages 5 and 6.)

[Gurugubelli 2014] Pardha S Gurugubelli, Rajeev K Jaiman and Boo Cheong Khoo. *Flexible Flapping Dynamics of Parallel Elastic Plates in a Uniform Flow: Application to Energy Harvesting Devices.* In ASME 2014 33rd International Conference on Ocean, Offshore and Arctic Engineering, pages V002T08A038–V002T08A038. American Society of Mechanical Engineers, 2014. (Cited on page 103.)

[Gurugubelli 2015] Pardha S Gurugubelli and Rajeev K Jaiman. *Energy Harvesting using flapping dynamics of piezoelectric inverted flexible foil.* In ASME 2015 34rd International Conference on Ocean, Offshore and Arctic Engineering. American Society of Mechanical Engineers, 2015. (Cited on page 107.)

[Hagood 1991] N. W. Hagood and A. von Flotow. *Damping of structural vibrations with piezoelectric materials and passive electrical networks.* J. Sound Vib., vol. 146, no. 2, pages 243–68, 1991. (Cited on page 11.)

[Huang 1995] L. Huang. *Flutter of cantilevered plates in axial flow.* J. Fluids Struct., vol. 9, no. 2, pages 127–147, 1995. (Cited on page 3.)

[Jia 2007] Lai-Bing Jia, Fang Li, Xie-Zhen Yin and Xie-Yuan Yin. *Coupling modes between two flapping filaments.* Journal of Fluid Mechanics, vol. 581, pages 199–220, 2007. (Cited on pages 7, 81 and 87.)

[Jia 2008] Lai-Bing Jia and Xie-Zhen Yin. *Passive oscillations of two tandem flexible filaments in a flowing soap film.* Physical review letters, vol. 100, no. 22, page 228104, 2008. (Cited on page 8.)

[Jones 2003] Marvin A Jones. *The separated flow of an inviscid fluid around a moving flat plate.* Journal of Fluid Mechanics, vol. 496, pages 405–441, 2003. (Cited on page 87.)

[Kim 2010] Sohae Kim, Wei-Xi Huang and Hyung Jin Sung. *Constructive and destructive interaction modes between two tandem flexible flags in viscous flow.* Journal of Fluid Mechanics, vol. 661, pages 511–521, 2010. (Cited on page 8.)

[Kim 2013] Daegyoum Kim, Julia Cossé, Cecilia Huertas Cerdeira and Morteza Gharib. *Flapping dynamics of an inverted flag.* Journal of Fluid Mechanics, vol. 736, page R1, 2013. (Cited on page 107.)

[King 1973] R. King, M. J. Prosser and D. J. Johns. *On vortex excitation of model piles in water.* J. Sound Vib., vol. 29, no. 2, pages 169 – IN2, 1973. (Cited on page 49.)

[Kornecki 1976] A Kornecki, EH Dowell and J O'brien. *On the aeroelastic instability of two-dimensional panels in uniform incompressible flow.* Journal of Sound and Vibration, vol. 47, no. 2, pages 163–178, 1976. (Cited on page 3.)

[Krasny 1986] Robert Krasny. *Desingularization of periodic vortex sheet roll-up.* Journal of Computational Physics, vol. 65, no. 2, pages 292–313, 1986. (Cited on page 117.)

[Kwon 2010] Soon-Duck Kwon. *A T-shaped piezoelectric cantilever for fluid energy harvesting.* Appl. Phys. Lett., vol. 97, no. 16, page 164102, 2010. (Cited on page 12.)

[Lee 1989] C-K Lee and FC Moon. *Laminated piezopolymer plates for torsion and bending sensors and actuators.* The Journal of the Acoustical Society of America, vol. 85, no. 6, pages 2432–2439, 1989. (Cited on pages 30 and 111.)

[Lefeuvre 2006] E. Lefeuvre, A. Badel, C. Richard, L. Petit and D. Guyomar. *A comparison between several vibration-powered piezoelectric generators for standalone systems.* Sens. Actuat. A Phys., vol. A 126, pages 405–416, 2006. (Cited on page 58.)

[Lemaitre 2005] C Lemaitre, Pascal Hémon and Emmanuel De Langre. *Instability of a long ribbon hanging in axial air flow.* Journal of Fluids and Structures, vol. 20, no. 7, pages 913–925, 2005. (Cited on page 4.)

[Lighthill 1960] M. J. Lighthill. *Note on the swimming of slender fish.* J. Fluid Mech., vol. 9, pages 305–317, 1960. (Cited on page 14.)

[Lighthill 1970] M. J. Lighthill. *Aquatic animal propulsion of high hydromechanical efficiency.* J. Fluid Mech., vol. 44, pages 265–301, 1970. part 2. (Cited on pages 14 and 15.)

[Lighthill 1971] M. J. Lighthill. *Large-amplitude elongated-body theory of fish locomotion.* Proc. R. Soc. Lond. B, vol. 179, pages 125–138, 1971. (Cited on pages 4, 13, 14 and 15.)

[Lippmann 1881] Gabriel Lippmann. *Principe de la conservation de l'électricité.* Annales de chimie et de physique, vol. 24, page 145, 1881. (Cited on page 9.)

[Mason 2002] John C Mason and David C Handscomb. Chebyshev polynomials. CRC Press, 2002. (Cited on page 119.)

[Michelin 2008] S. Michelin, S. Llewellyn Smith and B. Glover. *Vortex shedding model of a flapping flag.* J. Fluid Mech., vol. 617, pages 1–10, 2008. (Cited on pages 4, 26 and 87.)

[Michelin 2009] S. Michelin and S. G. Llewellyn Smith. *Linear stability analysis of coupled parallel flexible plates in an axial flow.* J. Fluids Struct., vol. 25, pages 1136 – 1157, 2009. (Cited on pages 7, 8, 81 and 92.)

[Michelin 2013] S. Michelin and O. Doaré. *Energy harvesting efficiency of piezoelectric flags in axial flows.* J. Fluid Mech., vol. 714, pages 489–504, 2013. (Cited on pages 4, 9, 12, 20, 21, 23, 42, 46, 49, 52, 67, 89 and 106.)

[Muskhelishvili 2008] Nikolai Ivanovich Muskhelishvili and Jens Rainer Maria Radok. Singular integral equations: boundary problems of function theory and their application to mathematical physics. Courier Corporation, 2008. (Cited on page 118.)

[Ng 2005] T.H. Ng and W.H. Liao. *Sensitivity analysis and energy harvesting for a self-powered piezoelectric sensor.* J. Intell. Mater. Syst. Struct., vol. 16, no. 10, pages 785–797, 2005. (Cited on page 50.)

[Nuhait 2010] Abdullah O Nuhait and Dean T Mook. *Aeroelastic behavior of flat plates moving near the ground.* Journal of Aircraft, vol. 47, no. 2, pages 464–474, 2010. (Cited on page 5.)

[Peng 2009] Z. Peng and Q. Zhu. *Energy harvesting through flow–induced oscillations of a foil.* Phys. Fluids., vol. 21, page 12362, 2009. (Cited on page 1.)

[Perez 2015] M Perez, S Boisseau, P Gasnier, J Willemin and JL Reboud. *An electret-based aeroelastic flutter energy harvester.* Smart Materials and Structures, vol. 24, no. 3, page 035004, 2015. (Cited on page 57.)

[Piñeirua 2015] Miguel Piñeirua, Olivier Doaré and Sébastien Michelin. *Influence and optimization of the electrodes position in a piezoelectric energy harvesting flag.* arXiv preprint arXiv:1501.04303, 2015. (Cited on pages 42, 57 and 80.)

[Pobering 2004] S. Pobering and N. Schwesinger. *A Novel Hydropower Harvesting Device.* In MEMS, NANO and Smart Systems, 2004. ICMENS 2004. Proc. 2004 Int. Conf. on, pages 480–485, Aug 2004. (Cited on page 12.)

[Ramadan 2014] Khaled S Ramadan, D Sameoto and S Evoy. *A review of piezoelectric polymers as functional materials for electromechanical transducers.* Smart Materials and Structures, vol. 23, no. 3, page 033001, 2014. (Cited on page 9.)

[Ristroph 2008] Leif Ristroph and Jun Zhang. *Anomalous hydrodynamic drafting of interacting flapping flags.* Physical review letters, vol. 101, no. 19, page 194502, 2008. (Cited on pages 8, 81, 82 and 101.)

[Roundy 2005] Shad Roundy, Eli S Leland, Jessy Baker, Eric Carleton, Elizabeth Reilly, Elaine Lai, Brian Otis, Jan M Rabaey, Paul K Wright and V Sundararajan. *Improving power output for vibration-based energy scavengers.* Pervasive Comput, IEEE, vol. 4, no. 1, pages 28–36, 2005. (Cited on page 50.)

[Ryu 2015] Jaeha Ryu, Sung Goon Park, Boyoung Kim and Hyung Jin Sung. *Flapping dynamics of an inverted flag in a uniform flow.* Journal of Fluids and Structures, vol. 57, pages 159–169, 2015. (Cited on page 107.)

[Saffman 1992] Philip G Saffman. Vortex dynamics. Cambridge university press, 1992. (Cited on pages 86, 87 and 118.)

[Sawada 2006] Tomohiro Sawada and Toshiaki Hisada. *Fluid-structure interaction analysis of a two-dimensional flag-in-wind problem by the ALE finite element method.* JSME International Journal Series A Solid Mechanics and Material Engineering, vol. 49, no. 2, pages 170–179, 2006. (Cited on page 4.)

[Schouveiler 2009] L. Schouveiler and C. Eloy. *Coupled flutter of parallel plates.* Phys. Fluids., vol. 21, no. 081703, 2009. (Cited on page 8.)

[Shelley 2011] M. J. Shelley and J. Zhang. *Flapping and bending bodies interacting with fluid flows.* Annu. Rev. Fluid. Mech., vol. 43, pages 449–465, 2011. (Cited on page 3.)

[Shenck 2001] Nathan S. Shenck and Joseph A. Paradiso. *Energy Scavenging with Shoe-Mounted Piezoelectrics.* IEEE Micro, vol. 21, no. 3, pages 30–42, 2001. (Cited on page 12.)

[Shepherd 1990] Dennis G Shepherd. *Historical development of the windmill.* 1990. (Cited on page 1.)

[Singh 2012a] K. Singh, S. Michelin and E. de Langre. *Energy harvesting from axial fluid-elastic instabilities of a cylinder.* J. Fluids Struct., vol. 30, pages 159–172, 2012. (Cited on page 8.)

[Singh 2012b] Kiran Singh, Sébastien Michelin and Emmanuel De Langre. *The effect of non-uniform damping on flutter in axial flow and energy-harvesting strategies.* In Proceedings of the Royal Society of London A: Mathematical, Physical and Engineering Sciences, volume 468, pages 3620–3635. The Royal Society, 2012. (Cited on pages 4 and 15.)

[Sodano 2004] Henry A Sodano, Daniel J Inman and Gyuhae Park. *A review of power harvesting from vibration using piezoelectric materials.* Shock Vibration Dig., vol. 36, no. 3, pages 197–206, 2004. (Cited on page 11.)

[Song 2014] RJ Song, XB Shan, FB Tian and T Xie. *Energy harvesting simulation of two piezoelectric flags in tandem arrangement in the uniform flow.* In Electronic Packaging Technology (ICEPT), 2014 15th International Conference on, pages 1–4. IEEE, 2014. (Cited on pages 82 and 102.)

[Taneda 1968] Sadatoshi Taneda. *Waving motions of flags.* Journal of the Physical Society of Japan, vol. 24, no. 2, pages 392–401, 1968. (Cited on page 3.)

[Tang 2007] L. Tang and M. P. Paidoussis. *On the instability and the post-critical behavior of two-dimensional cantilevered flexible plates in axial flow.* J. Sound Vib., vol. 305, pages 97 – 115, 2007. (Cited on page 4.)

[Tang 2008] L. Tang, M. P. Paidoussis and J. Jiang. *Cantilevered flexible plates in axial flow: energy transfer and the concept of flutter-mill.* J. Sound Vib., vol. 326, pages 263 – 276, 2008. (Cited on page 8.)

[Tang 2015] Chao Tang, Nan-Sheng Liu and Xi-Yun Lu. *Dynamics of an inverted flexible plate in a uniform flow.* Physics of Fluids (1994-present), vol. 27, no. 7, page 073601, 2015. (Cited on page 107.)

[Taylor 1952] G. Taylor. *Analysis of the Swimming of Long and Narrow Animals.* Proc. R. Soc. Lond. A: Math. Phys. Sci., vol. 214, no. 1117, pages 158–183, 1952. (Cited on page 15.)

[Taylor 2001] G. W. Taylor, J. R. Burns, S. M. Kammann, W. B. Powers and T. R. Welsh. *The energy harvesting eel: a small subsurface ocean/river power generator.* IEEE J. Oceanic Eng., vol. 26, no. 4, pages 539–547, 2001. (Cited on page 12.)

[Thomas 2009] O. Thomas, J. F. Deu and J. Ducarne. *Vibrations of an elastic structure with shunted piezoelectric patches: efficient finite element formulation and electromechanical coupling coefficients.* Int. J. Numer. Methods. Eng., vol. 80, pages 235–268, 2009. (Cited on pages 11 and 17.)

[Thomas 2011] Olivier Thomas. *Dynamique linéaire et non linéaire de structures élastiques et piézoélectriques.* Habilitation à diriger des recherches en sciences pour l'ingénieur, Ecole Normale Supérieure de Cachan, November 2011. in French. (Cited on pages 10 and 11.)

[Tian 2012] Fangbao Tian, Xiyun Lu and Haoxiang Luo. *Onset of instability of a flag in uniform flow.* Theoretical and Applied Mechanics Letters, vol. 2, no. 2, page 022005, 2012. (Cited on page 5.)

[Timoshenko 1953] Stephen Timoshenko. History of strength of materials: with a brief account of the history of theory of elasticity and theory of structures. Courier Corporation, 1953. (Cited on pages 30 and 112.)

[Umeda 1996] Mikio Umeda, Kentaro Nakamura and Sadayuki Ueha. *Analysis of the transformation of mechanical impact energy to electric energy using piezoelectric vibrator.* Jpn. J. of Appl. Phys., vol. 35, no. 5S, page 3267, 1996. (Cited on page 11.)

[Vijaya 2012] MS Vijaya. Piezoelectric materials and devices: Applications in engineering and medical sciences. CRC Press, 2012. (Cited on page 10.)

[Virot 2013] Emmanuel Virot, Xavier Amandolese and Pascal Hémon. *Fluttering flags: An experimental study of fluid forces.* J. Fluids Struct., vol. 43, pages 385–401, 2013. (Cited on pages 4, 16 and 26.)

[Virot 2015] Emmanuel Virot. *Flottement de drapeau: dynamique et couplage.* PhD thesis, Ecole Polytechnique, 2015. (Cited on pages 8 and 57.)

[Wang 2010] Si-ying Wang, Chuan-bao Sun and Xie-zhen Yin. *Experiment of the Flapping Coupling Modes between Two Parallel Flags in a Aniform Flow.* Journal of Experimental Mechanics, vol. 4, page 007, 2010. in Chinese. (Cited on page 7.)

[Watanabe 2002a] Y. Watanabe, K. Isogai, S. Suzuki and M. Sugihara. *An experimental study of paper flutter.* J. Fluids Struct., vol. 16, no. 4, pages 543–560, 2002. (Cited on page 4.)

[Watanabe 2002b] Y. Watanabe, S. Suzuki, M. Sugihara and Y. Sueoka. *An experimental study of paper flutter.* J. Fluids Struct., vol. 16, no. 4, pages 529–542, 2002. (Cited on page 4.)

[WEB1] Vortex Hydro Energy WEB1. *Vortex Hydro Energy.* (Cited on pages 1 and 2.)

[WEB2] Morgan Electro Ceramics WEB2. *Guide to Piezoelectric & Dielectric Ceramic.* (Cited on pages 9 and 10.)

[Weideman 2000] J Andre Weideman and Satish C Reddy. *A MATLAB differentiation matrix suite.* ACM Transactions on Mathematical Software (TOMS), vol. 26, no. 4, pages 465–519, 2000. (Cited on page 120.)

[Weihs 1973] D Weihs. *Hydromechanics of fish schooling.* 1973. (Cited on pages 6 and 7.)

[Williams 1996] C.B Williams and R. B. Yates. *Analysis of a micro-electric generator for microsystems.* Sens. Actuat A: Physical, vol. 52, no. 1, pages 8–11, 1996. (Cited on page 11.)

[Williamson 2004] C. H. K. Williamson and R. Govardhan. *Vortex–Induced Vibrations.* Annu. Rev. Fluid. Mech., vol. 36, no. 1, pages 413–455, 2004. (Cited on page 49.)

[Wu 1961] Tao-tsu Wu. *Swimming of a waving plate.* Journal of Fluid Mechanics, vol. 10, no. 03, pages 321–344, 1961. (Cited on page 3.)

[Yamaguchi 2000a] Nobuyuki Yamaguchi, Tooru Sekiguchi, Kazuhiko Yokota and Yoshinobu Tsujimoto. *Flutter limits and behavior of a flexible thin sheet in high-speed flowâĂŤII: experimental results and predicted behaviors for low mass ratios.* Journal of fluids engineering, vol. 122, no. 1, pages 74–83, 2000. (Cited on page 26.)

[Yamaguchi 2000b] Nobuyuki Yamaguchi, Kazuhiko Yokota and Yoshinobu Tsujimoto. *Flutter limits and behaviors of a flexible thin sheet in high-speed flowâĂŤI: analytical method for prediction of the sheet behavior.* Journal of fluids engineering, vol. 122, no. 1, pages 65–73, 2000. (Cited on page 26.)

[Yang 2005] J. Yang. An introduction to the theory of piezoelectricity. Springer, 2005. (Cited on page 12.)

[Zhang 2000] J. Zhang, S. Childress, A. Libchaber and M. Shelley. *Flexible filaments in a flowing soap film as a model for one-dimensional flags in a two dimensional wind.* Nature, vol. 408, pages 835–839, 2000. (Cited on pages 3, 6, 81 and 87.)

[Zhu 2002] Luoding Zhu and Charles S Peskin. *Simulation of a flapping flexible filament in a flowing soap film by the immersed boundary method.* Journal of Computational Physics, vol. 179, no. 2, pages 452–468, 2002. (Cited on page 4.)

[Zhu 2003] Luoding Zhu and Charles S Peskin. *Interaction of two flapping filaments in a flowing soap film.* Physics of Fluids (1994-present), vol. 15, no. 7, pages 1954–1960, 2003. (Cited on pages 7 and 81.)

[Zhu 2009] Luoding Zhu. *Interaction of two tandem deformable bodies in a viscous incompressible flow.* Journal of Fluid Mechanics, vol. 635, pages 455–475, 2009. (Cited on page 81.)

[Zhu 2012] Qiang Zhu. *Energy harvesting by a purely passive flapping foil from shear flows.* Journal of Fluids and Structures, vol. 34, pages 157–169, 2012. (Cited on page 1.)

Nomenclature

α	Coupling coefficient
β	Ratio between the resistance's dissipation rate and the flow time scale
β_{ext}	Ratio of dissipation rate in the harvesting resistor and the flow time scale
$\boldsymbol{\tau}$	Flag's tangential vector
χ	Mechanical/Piezoelectric conversion factor
$\Delta\phi$	Phase difference of two flags placed in the same flow
η	Harvesting efficiency
γ	Strength of the vortex sheet
$\mathbf{F}_{\text{fluid}}$	Fluid's pressure on the flag, both dimensional and dimensionless form
$\mathbf{F}_{\text{react}}$	Reactive force
$\mathbf{F}_{\text{resis}}$	Resistive force
$\mathbf{n}$	Flag's normal vector
$\mathbf{x}$	Flag's displacement, both dimensional and dimensionless form
$\mathcal{A}$	Flag's amplitude, both dimensional and dimensionless forms
$\mathcal{C}$	Intrinsic capacitance of one piezoelectric pair
$\mathcal{E}_C$	Energy stored in intrinsic capacitance
$\mathcal{E}_I$	Energy stored in inductance
$\mathcal{E}_k$	Flag's kinetic energy
$\mathcal{E}_p$	Flag's potential energy
$\mathcal{G}$	Electrical conductance of a resistor
$\mathcal{I}$	Electric current
$\mathcal{L}$	Inductance of an inductor
$\mathcal{M}$	Flag's bending torque, both dimensional and dimensionless form
$\mathcal{P}$	Harvested power, both dimensional and dimensionless forms
$\mathcal{R}$	Resistance of a harvesting resistor in local circuit

$\mathcal{R}_d$ Internal resistance of DAQ

$\mathcal{R}_L$ Internal resistance of inductor

$\mathcal{T}$ Rate of energy transfer from the structure to the circuit

$\mathcal{W}_f$ Rate of work of fluid force

μ Flag's mass per unit length

ν Poisson's coefficient

ω Frequency in radian

ω_0 Dimensionless natural frequency of a LC circuit

$\mathcal{R}_{\text{ext}}$ Harvesting resistor in electric network

ρ_f^s Fluid mass per unit surface

ρ_f Fluid density

θ Flag's orientation

B Flag's bending rigidity

C Contour of the vortex sheet

c Linear density of capacitance

C_d Drag coefficient

C_f Contour of the vortex sheet attached to the flag

C_w Contour of the vortex sheet representing the shed wake

D Distance separating two flags

d Dimensionless form of the distance separating two flags

E Young's modulus

f Frequency in Hertz

F_{elec} Electrical energy flux

F_{mech} Mechanical energy flux

$F_{\text{p1}}, F_{\text{p2}}$ Contribution of piezoelectric effects to mechanical energy flux

g Linear density of conductance

H Flag's width

H^*	Aspect ratio
h_0	Thickness of a flag's middle layer
h_p	Thickness of piezoelectric layer
I	Electric current in the electric network
L	Flag's length
l	Linear density of inductance
l_p	Length of one piezoelectric pair
m	Mass of the MFC flag
M^*	Mass ratio fluid/solid
m_a	Added mass coefficient
Q	Electric charge displacement in one piezoelectric pair
q_I	Electric charge displacement in inductance
T	Flag's tension, both dimensional and dimensionless form
U^*	Reduced velocity
U_c^*	Critical velocity for instability
U_∞	Incoming flow velocity
U_τ	Tangential component of relative velocity
U_n	Normal component of relative velocity
V	Voltage applied on one piezoelectric pair
Z	Electrical impedance
z	Linear density of impedance

Récupération d'énergie par drapeaux piézoélectriques

Résumé: L'instabilité de flottement de structures flexibles (ex : drapeaux) en écoulement axial constitue un exemple classique d'instabilité par interaction fluide-structure. Cette instabilité entraîne un flottement spontané et auto-entretenu de grande amplitude du drapeau. En ce sens, ce phénomène présente un intérêt pour la récupération d'énergie d'un écoulement, s'il est possible de convertir l'énergie associée au mouvement solide en électricité. Les drapeaux piézoélectriques représentent une piste pour exploiter ce phénomène : ces drapeaux sont recouverts de matériaux piézoélectriques, capables de convertir la déformation de la structure en transfert de charge et en énergie électrique. Dans cette thèse, nous proposons d'étudier ce concept de récupération d'énergie par des moyens expérimentaux et numériques, et en particulier l'impact du circuit récupérateur sur la dynamique du système fluide-solide-électrique. Nos résultats montrent que le drapeau piézoélectrique constitue un concept prometteur pour la récupération d'énergie. Dans un premier temps, on illustre une amélioration de l'efficacité par le phénomène de l'accrochage de fréquence. Dans un second temps, nous étudions la performance de récupération d'énergie de deux drapeaux placés dans un même écoulement et interagissent au travers de l'écoulement (interactions hydrodynamiques) et par leur connexion à un même circuit aval (interactions électrodynamiques).
Mot clef : Instabilité de flottement, récupération d'énergie, drapeaux piézoélectriques, accrochage de fréquence, couplage hydrodynamique

Energy harvesting by piezoelectric flags

Abstract: The flutter instability of flexible plates, or flags, in an axial flow is a canonical fluid-structure instability that results in the flags' large-amplitude spontaneous and self-sustained flapping. This phenomenon consequently appears as an interesting mechanism for flow energy harvesting, if the mechanical energy associated with this solid motion can be converted into electrical form. One route to exploit this mechanism is the concept of so-called piezoelectric flags: these flexible plates covered by piezoelectric materials which convert mechanical energy into electrical energy through the materials' mechanical deformation. In this thesis, we propose to study both experimentally and numerically this concept of energy harvesting. Our results illustrate promising perspective of harvesting energy with piezoelectric flags. We first show that by using circuits possessing resonant properties, the energy harvesting becomes more efficient through a frequency lock-in phenomenon. Second, we studied the energy-harvesting performance of two flags placed in the same fluid flow and are coupled through the flow (hydrodynamic coupling) and through the output circuit (electrodynamic coupling).
Keywords: Flutter instability, energy harvesting, piezoelectric flags, frequency lock-in, hydrodynamic coupling